Contents

Part One Control Models for AC Motors

List of Contributors

Haitham Abu-Rub
Department of Electrical & Computer Engineering, Texas A&M University at Qatar, Qatar

Tarek Ahmed-Ali
GREYC Lab, University of Caen Basse-Normandie, France

Vincent Van Assche
GREYC Lab, University of Caen Basse-Normandie, France

Giovanni Azzone
Dipartimento di Ingegneria "Enzo Ferrari", Università di Modena e Reggio Emilia, Italy

Gildas Besançon
Control System Department, GIPSA Lab, Grenoble Institute of Techology and Institut Universitaire de France, France

Marc Bodson
Electrical and Computer Engineering, University of Utah, USA

Robert Boisliveau
Ecole Centrale de Nantes, LUNAM, France

Ajit K. Chattopadhyay
Electrical Engineering Department, Bengal Engineering & Science University, India

Fatima-Zahra Chaoui
GREYC Lab, University of Caen Basse-Normandie, France

Maria Letizia Corradini
Scuola di Scienze e Tecnologie, Università di Camerino, Italy

Jesús De León
FIME, Universidad Autonoma de Nuevo Leon, Mexico

Marc Diguet
Alstom Transport, France

Philippe Dorléans
GREYC Lab, University of Caen Basse-Normandie, France

out without the innumerable and exciting exchanges we had along the past 10 years. I am particularly grateful to Abderrahim and Abdelmounim who kindly accepted to retype in Latex some chapters initially written in Word by the authors. Last, but not least, I would like to thank Peter Mitchell, Liz Wingett, and Richard Davies, all three from John Wiley & Sons, Ltd, UK, who provided numerous advice and material help during the editing stage of the book.

Fouad Giri
University Distinguished Professor
University of Caen Basse-Normandie
France

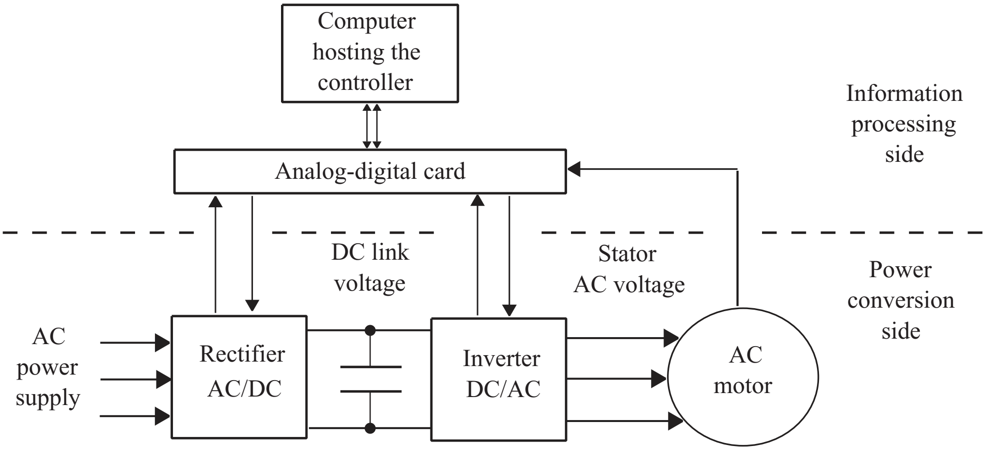

Figure 1.1 AC motor control architecture

Synchronous motors also exist in two versions, namely, permanent-magnet and wound rotor. Unlike induction motors, there are no induced rotor currents in synchronous motors in steady state, because the rotor rotates at the same speed as the rotating magnetic field. A motor torque is developed due to the interaction between the stator rotating field and a rotor field generated either by permanent magnets or by an injected rotor current.

For both induction and synchronous motors, variable speed operation is possible if the stator supply frequency is made variable. Until the development of modern power electronics, there was no simple and effective way to vary the frequency of the motors' supply voltages. Nowadays, reliable high-speed switching power converters are available that serve as actuators in AC motor control. Specifically, an AC motor is supplied with power through an association of two power converters, a rectifier and an inverter (Figure 1.1). The former, also called AC/DC converter, converts the AC power provided by the grid into DC power. Control of the rectifier is not always implemented, but is useful to regulate the DC voltage, or to enable regeneration of power to the grid. The inverter, also referred to as DC/AC converter, transforms the DC voltage into an AC voltage with a specified frequency. The result is achieved by chopping the DC voltage at a high rate, typically using a pulse-width modulation (PWM) technique. In this respect, it is worth emphasizing the considerable progress made in computer technology, which has resulted in fast multiprocessor computers and high-performance analog-digital interfaces. This progress has made possible the real-time implementation of sophisticated methods to control the power converters associated with AC machines.

DC motors require schemes similar to Figure 1.1, but with lower bandwidth requirements and fewer channels. However, ACs are produced in conductors through mechanical commutation, rather than electrical commutation. The commutators of DC motors are complex and vulnerable. As a result, AC motors offer a higher power/mass ratio, relatively low cost, and simple maintenance. AC motors exist with a variety of characteristics and in a large range of sizes, from a few watts to many thousands of kilowatts. For these reasons, AC drive systems have already replaced DC drives in several industrial fields and this widespread proliferation is expected to continue. Nowadays, AC drives are used in almost all industrial applications, such as the following:

1. **Transport:** vehicle traction, marine propulsion
2. Milling in cement, steel, paper, and others industries
3. Pumping/compressing in oil and gas industry
4. Cranes and industrial vehicles
5. **Domestic machines:** lifts, washing machines, and others.

1.2 Control Issues

1.2.1 State-Feedback Speed Control

The prime objective in AC motor control is to make the rotor turn at a desired speed despite load variations. If the desired speed is constant, one talks of speed regulation, while tracking problems correspond to time-varying speeds. The desired speed, also called the speed reference signal, is often unknown a priori, making the control issue more difficult. Indeed, the achievement of a desired rotor speed profile necessitates a sufficient motor torque to overcome the load torque, but also to provide the required accelerations of the rotor during transient periods.

In AC induction motors, the generation of a given torque necessitates a sufficient level of rotor magnetization, that is, a sufficiently high flux magnitude in the rotor. Flux control is thus not independent from the problem of speed control and both are acted upon through the inverter control signals. These signals are binary signals commanding on and off conduction modes. The electromechanical nature of the motor entails nonlinearities associated with products of fluxes with currents and fluxes with speed. Furthermore, the three-phase nature of the motor means that the overall model is nonlinear, of high dimension, as well as controlled through binary signals. A common practice consists in reducing the model dimension by resorting to Park's transformation, which projects the three-phase variables (generally referred to as *abc*) on a two-phase rotating coordinate frame (generally referred to as *dq*) (see, e.g., Blaschke 1972; Leonard 2001). The binary nature of the inverter signals is generally coped with by averaging the signals over the PWM period and letting the control design be based on the corresponding averaged two-coordinate model (see, e.g., Sira-Ramirez and Silva-Ortigoza 2006). Model nonlinearity is handled using modern nonlinear control design techniques, including state- and output-feedback linearization, Lyapunov control, sliding-mode (SM) control, passivity-based control (Ortega *et al.* 1998; Isidori 1999; Sastry 1999; Vidyasagar 2002; Khalil 2003).

The basic ideas described so far lead to the control strategy depicted in Figure 1.2.

1.2.2 Adaptive Output-Feedback Speed Control

The basic state-feedback control strategy of Figure 1.2 assumes that all controlled system parameters are known. However, some system parameters are generally not known a priori, and may even be varying in normal operating conditions. In particular, the stator and the rotor resistances are sensitive to the magnitude of the currents, and thus undergo wide variations in the presence of speed reference and load torque changes. The rotor-load set inertia and rotor friction coefficient may also vary (e.g., in transportation applications). To maintain the control

Table 2.1 Rating plate of the used induction motor

Nominal power	P_n	2.2	kW
Nominal voltage	U_{sn}	380/420	V
Nominal current	I_{sn}	4.9	A
Frequency	f	50	Hz
Nominal speed	ω_{mn}	1430	rad/min
$\cos\psi$		0.81	

denoted ω_{mo}. As a consequence, the stator currents and the electromagnetic torque T_{em} vanish at $t = 0$ and the mechanical equation (2.52) simplifies to, for $t > 0$,

$$J\frac{d\omega_m}{dt} = -F\omega_m - T_d. \tag{2.78}$$

Clearly, equation (2.78) is linear in the quantities $(\frac{T_d}{J})$ and $(\frac{F}{J})$. Then, the least squares estimator can be resorted to get estimates of these quantities using a sufficiently large sample of measurements (t, ω_{mo}) (e.g., Ioannou and Fidan 2006). Presently, a quite simpler alternative necessitating only four speed measures is presented, getting benefit of the fact that speed measurements are weakly noisy. The key point is that the solution of the first order equation (2.78) is easily found. Specifically, one has

$$\omega_m(t) = \left(\omega_{mo} + \frac{T_d}{F}\right) e^{\frac{-t}{\tau_m}} - \frac{T_d}{F}, \tag{2.79}$$

using the fact that $\omega_m(0) = \omega_{mo}$, where $\tau_m = \frac{F}{J}$ is the mechanical constant time. The expression (2.79) shows that the rotor speed is exponentially decaying and vanishes at a finite stop time, say t_s. Figure 2.6 shows the decaying speed curve obtained when the motor of Table 2.1 is submitted to the deceleration test. From such a curve, let us get two arbitrary time-speed couples (t_1, ω_{m1}) and (t_2, ω_{m2}) with $t_2 = 2t_1$. Writing equation (2.79) for $t = t_1$ and $t = t_2$, one gets the following equations:

$$\omega_{m1} = \left(\omega_{mo} + \frac{T_d}{F}\right) e^{\frac{-t_1}{\tau_m}} - \frac{T_d}{F}, \tag{2.80}$$

$$\omega_{m2} = \left(\omega_{mo} + \frac{T_d}{F}\right) e^{\frac{-2t_1}{\tau_m}} - \frac{T_d}{F}. \tag{2.81}$$

Subtracting side-to-side equation (2.80) from equation (2.81), gives

$$\omega_{m2} - \omega_{m1} = \left(\omega_{mo} + \frac{T_d}{F}\right) e^{\frac{-t_1}{\tau_m}} \left(e^{\frac{-t_1}{\tau_m}} - 1\right). \tag{2.82}$$

Also, one immediately gets from (2.80)

$$\omega_{m1} - \omega_{mo} = \left(\omega_{mo} + \frac{T_d}{F}\right) \left(e^{\frac{-t_1}{\tau_m}} - 1\right). \tag{2.83}$$

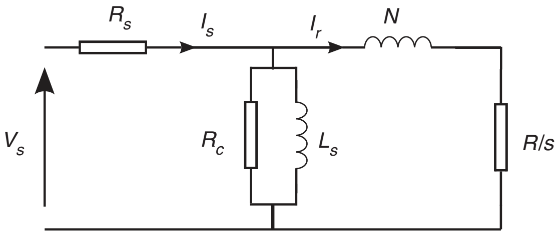

Figure 2.7 Per phase equivalent circuit, viewed from the stator, of a three-phase induction motors. V_s is the stator phase voltage; R_s is stator resistance and R is the rotor winding resistance brought to the stator side; N is the equivalent inductance of both stator and rotor leakage brought to the rotor side. L_s is the magnetizing and stator inductance; R_c is the equivalent resistance for core loss; and s is the slip.

The equivalent circuit parameters for an induction motor can be determined using specific tests on the motor. The tests are quite similar to those performed on transformers.

Stator Winding Resistance Measurement

The resistance of the stator winding is measured at DC, and the measurement is preferably performed after the motor temperature has reached its nominal value. This experimental test gives, for the induction motor characterized by Table 2.1, the following value:

$$R_s = 2.5\ \Omega, \tag{2.88}$$

Loadless Test

This experiment consists of applying a balanced three-phase voltage, at the rated frequency, to the stator terminals, while the rotor is carrying no mechanical load. Currents, voltages, and powers are measured at the motor input. As the slip of the loadless induction motor is very low, the value of the equivalent resistance in the rotor branch of the equivalent circuit is very high. The no-load rotor current is then negligible and the rotor branch of the equivalent circuit can also be negligible. The approximate equivalent circuit, in the loadless test, simplifies as it is shown in Figure 2.8.

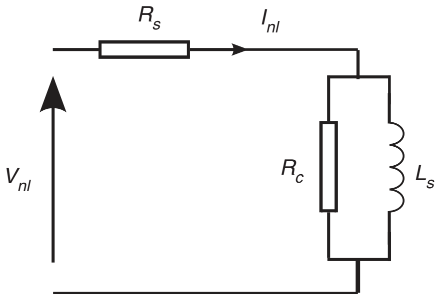

Figure 2.8 Induction machine equivalent circuit in loadless test

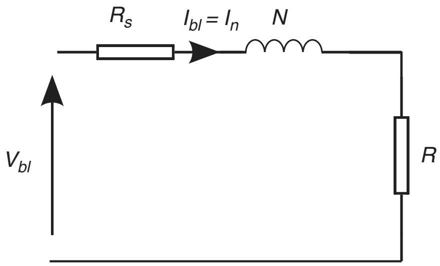

Figure 2.9 Induction machine equivalent circuit in blocked rotor test

smaller, compared to the magnetizing branch, so that the corresponding equivalent circuit boils down to the simpler configuration of Figure 2.9.

The measurements to be performed in this test are the following:

- The three-phase active power P_{bl}.
- The three-phase reactive power Q_{bl}.
- The line voltage V_{bl}.
- The line current I_{bl}.

R and N can be calculated from the following equations:

$$R = \frac{P_{bl}}{3I_{bl}^2} - R_s, \qquad N = \frac{\sqrt{\left(\frac{V_{bl}}{I_{bl}}\right)^2 - (R+R_s)^2}}{\omega_s}. \tag{2.95}$$

As $N = \sigma L_r(\frac{L_s}{M_{sr}})^2$ and $R = R_r(\frac{L_s}{M_{sr}})^2$, the knowledge of R and N allows to calculate the rotor time constant and the parameter σ, using the expressions

$$T_r = \frac{L_s + N}{R}, \qquad \sigma = \frac{N}{N+L_s}. \tag{2.96}$$

The measurements made, in the blocked rotor test, on the induction machine of Table 2.1, are described in Table 2.6.

Table 2.6 Measurements made in blocked rotor test on the induction motor

V_{bl}	I_{bl}	P_{bl}	Q_{bl}
63.5 V	4.9 A	504 W	785 VAr

Table 2.7 Electrical parameter estimates of the induction motor

R_s	R_r	L_s	L_r	M_{sr}	T_r	σ
2.5 Ω	2.5 Ω	441.6 mH	441.6 mH	441.6 mH	100.6 ms	0.33

Then, using Table 2.6 and using the approximation that $L_r = M_{sr}$, one gets from equations (2.95) and (2.96) the electrical parameter estimates described in Table 2.7.

2.5 Conclusions

In this chapter, the problem of modeling induction motors has been concisely addressed. First, the triphase model is established applying electromagnetic and mechanical laws. This model is certainly the most physical as all variables it involves can be made accessible to measurements. However, it is hardly applicable in control design due to its high complexity. Then, simpler two-phase variants of that model are obtained by using the Park transformation. The simpler (two-phase) models are still nonlinear but will prove to be tractable in control design.

The modeling approach presented in this chapter is deliberately kept simple in the sense that the magnetic circuit has been supposed to be linear. As a matter of fact, in real-life machines, the magnetic circuit characteristic is nonlinear and linear approximations are only accurate if the machine operation does not entail wide-range rotor flux variation. Typically, the rotor flux must remain all the time close to its nominal value. The point is that a constant-flux operation cannot be optimal in the presence of varying load, when large speed variations are needed. In these situations, it is necessary to make the machine work with changing flux values to ensure high-efficiency operation. Models that account for the nonlinear nature of the machine magnetic characteristic have been presented in Levi (1995), Novotnak *et al.* (1999), Ouadi *et al.* (2011), and El Fadili *et al.* (2012b). An example of such models will be presented in Chapter 10 of this book.

References

Blaschke F (1972) The principle of field orientation applied to the new trans-vector closed-loop control system for rotating field machine. *Siemens Review*, **93**, 217–220.

De Leon J, Alvarez-Leal JG, Castro-Linares R, and Alvarez-Gallegos J (2001) Control of a flexible joint robot manipulator via a nonlinear control-observer scheme. *International Journal of Control*, **74**, 290–302.

El Fadili A, Giri F, Magri A, *et al.* (2012a) Adaptive nonlinear control of induction motors through AC/DC/AC converters. *Asian Journal of Control*, **14**, 1–14.

El Fadili A, Giri F, Magri A, *et al.* (2012b) Towards a global control strategy for induction motor. Speed regulation, flux optimization and power factor correction. *International Journal of Electrical Power and Energy Systems*, **43**, 230–244.

Ioannou PA and Fidan B (2006) *Adaptive Control Tutorial*. SIAM - Society for Industrial & Applied Mathematics.

Leonard W (2001) *Control of Electrical Drives*. Springer, New York.

Levi E (1995) A unified approach to main flux saturation modeling in D-Q axis models of induction machines. *IEEE Transactions on Energy Conversion*, **10**, 455–460.

Lubineau D, Dion JM, Dugard L, and Roye D (2000) Design of an advanced nonlinear controller for induction motor and experimental validation on an industrial benchmark. *EPJ Applied Physics*, **9**, 165–175.

Montanan M, Peresada S, and Tilli A (2006) A speed-sensorless indirect field-oriented control for induction motors based on high gain speed estimation. *Automatica*, **42**, 1637–1650.

Novotnak RT, Chiasson J, and Bodson M (1999) High performance motion control of an induction motor with magnetic saturation, *IEEE Transactions on Control Systems Technology*, **7**, 315–327.

Ouadi H, Giri F, and Dugard L (2011) Accounting for magnetic saturation in induction machines modeling. *International Journal of Modeling, Identification and Control*. **14**, 27–36.

Traore D, Plestan F, Glumineau A, and De Leon J (2008) Sensorless induction motor: high order sliding mode controller and adaptive interconnected observer. *IEEE Transactions on Industrial Electronics*, **55**, 3818–3827.

Vas P (1990) *Vector Control of AC Machines*. Clarendon Press, Oxford.

The stator and the rotor voltages equations (3.14) and (3.15) constitute, together with the mechanical equation (3.19), the model of the WRSM in the fixed three-coordinate frame linked to the three stator windings. From expressions (3.10b–c), of the self-inductance $[L_{ss}]$ and the mutual $[M_{sf}]$, it is seen that the stator and the rotor flux depends on both the time and the rotor position. This makes this model difficult to be exploited in control design. Indeed, the inductance matrix contains 13 nonzero terms, including 12 depending on the rotor position θ. This entails burdensome real-time implementations especially in transient regimes. To overcome these difficulties, the the Park transformation is resorted to obtain a lower-size position-independent model. Analytically described by equation (3.6), this transformation allows the passage from the (stator-related frame) three-phase models (3.14), (3.15), (3.10b–c) to the corresponding rotating dq-frame two-phase model. In the dq-frame, all inductances turn out to be constant and all signals are steady-state sinusoidal and referred to dc-quantities along d-axis or q-axis.

3.4.1 Oriented dq-Frame Model of Salient Pole WRSM

As explained in Chapter 2, it is beneficial to let the dq-frame be rotating at the rotor speed and be oriented along the the rotor flux d-axis so that the rotor flux q-component can be set to zero, reducing the model size (Blaschke 1972).

Then, operating the transformation (3.6), on the (three-phase) current $[i_{sabc}]$, the voltage $[v_{sabc}]$, and the flux $[\phi_{sabc}]$, one obtains the two-phase system ($[i_{sdq}]$, $[v_{sdq}]$, and $[\phi_{sdq}]$). Following closely a similar procedure in Chapter 2, one gets the equations that govern the dq quantities. The obtained equations are listed in order.

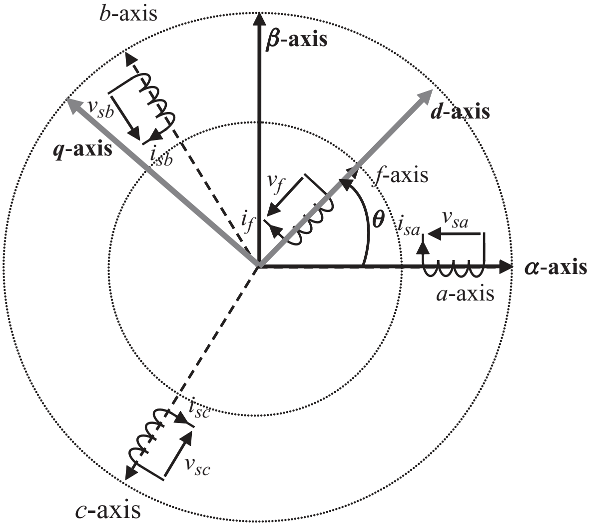

Figure 3.4 abc- and dq-coordinate frame in wound-rotor synchronous machines

created by the magnets. The distribution of the excitation field in the air gap and the MMFs are assumed to be sinusoidal (by assumption A3). Consequently, the expressions of the mutual flux of the inductor phases assume the following expressions:

$$\phi_{ra} = \phi_r \cos(p\theta), \tag{3.26a}$$

$$\phi_{rb} = \phi_r \cos(p\theta - 2\pi/3), \tag{3.26b}$$

$$\phi_{rc} = \phi_r \cos(p\theta + 2\pi/3), \tag{3.26c}$$

where ϕ_r is the amplitude of the flux produced by the permanent magnets, assumed to be constant as the variation with temperature is insignificant. It turns out that the flux through each of the stator windings is the sum of the flux induced by the rotor magnets and the flux produced by the currents carried by the stator phases. Specifically, one has

$$[\phi_{sabc}] = [L_{ss}][i_{sabc}] + [\phi_{rabc}]. \tag{3.27}$$

Furthermore, the fact that the rotor flux (PMSMs) is generated by permanent magnets, equation (3.9a) is still valid provided that the quantity $[M_{sf}]i_f$ (flux produced by the inductor in the WRSM case) is replaced by its PMSM equivalent, that is $[\phi_{rabc}]$. Now, using the flux expression (3.26a), the stator voltage expression (3.25) becomes

$$[v_{sabc}] = [R_s][i_{sabc}] + \frac{d}{dt}\{[L_{ss}][i_{sabc}]\} + \omega\frac{d}{d\theta}[\phi_{rabc}], \tag{3.28}$$

where we have used the rule $\frac{d}{dt}(\bullet) = \frac{d\theta}{dt}\frac{d}{d\theta}(\bullet) = \omega\frac{d}{d\theta}(\bullet)$.

The WRSM mechanical equation (3.19) remains valid for PMSMs again, provided the WRSM quantity $[M_{sf}]i_f$ is replaced by its PMSM equivalent $[\phi_{rabc}]$. Doing so, one gets

$$T_{em} = \frac{1}{2}[i_{sabc}]^T\left\{\frac{d[L_{ss}]}{d\theta}\right\}[i_{sabc}] + [i_{sabc}]^T\left\{\frac{d[\phi_{rabc}]}{d\theta}\right\}. \tag{3.29}$$

For convenience, the usual motion equation is rewritten

$$T_{em} = T_L + F\omega + J\frac{d\omega}{dt}. \tag{3.30}$$

3.5.2 *PMSM Model in the Rotating dq-Frame*

Electric Equations

The PMSM model in the rotating dq-frame, linked to the rotor (Figure 3.4), is derived from the abc-model, described by equation (3.28), by using the Concordia-Park transformation (3.6).

A brief overview on existing results about estimation issues in induction motors is proposed in next subsection.

4.2.2 *Short Literature Review*

Complex instrumentation placed on an induction motor would only cancel the major strength of this device—simplicity. It is the reason why one can hardly, if ever, see flux transducers in induction-motor-driven variable speed industry applications. On the other hand, flux information is crucial for the control of the drive, so flux estimation is an inescapable part of any variable-speed control design. Moreover, speed sensors might also be undesirable, leaving the stator current as the only output information that can be used for state estimation. Notice then that "sensorless" in the context of induction motor usually means "speed-sensorless."

When the mechanical speed is available through measurement, the measured values can be injected into the differential equation (4.1) making the model linear time varying, which therefore allow for a possible *Kalman-like* observer (see Section 4.3). However, under measured speed conditions, it is possible to build effective reduced-order observers for flux only, which, as opposed to a Kalman solution, may employ a constant gain in the correction term (Verghese and Sanders 1988). Passivity can also be exploited in order to build flux observers when the speed is measured (Martin and Rouchon 2000).

When the rotor speed is not available through measurements, the observation problem becomes significantly complex. Not only the model is now nonlinear and requires some dedicated observer design, but studies such as Canudas de Wit *et al*. (2000) and Ibarra Rojas *et al*. (2004) show that under zero synchronous speed and constant mechanical speed the systems becomes unobservable (in fact, in this case there is no information from the rotor side contained in the stator currents). The locus of the unobservability points is a straight line in the speed-torque plane—called the *unobservability line* of the motor—that runs through the origin of the plane and lies in the quadrants that correspond to a generator operating mode of the motor. Notice that, under closed-loop operation with load torques falling in the range safely handled by the motor (acting as a brake), such observability losses usually happen at rather low mechanical speeds. Based on this idea, some authors claim speed-sensorless estimation results with respect to low mechanical speed situations, which is actually a rather long stretch from the precise unobservability conditions; in reality, at *any* constant speed, the synchronous speed is the one responsible for the presence of information exchange between rotor and stator.

Any effort to accurately observe the state of the induction motor is futile if the parameters of the system are not known with sufficient precision. Unfortunately, this is likely to be the case during operation; in particular, the parameters that are the most susceptible to be uncertain are the resistances, as they (significantly) change with the temperature. Therefore, a realistic induction motor observation problem would actually be a joint state and parameter estimation problem. It is worth noticing at this point that it is impossible to identify all five fundamental electrical parameters from the input-output data, even when using speed measurements. In reality, it is only possible to estimate variables that are in bijection with $\frac{L_r}{R_r}$, R_s, L_s, and σ (Besançon *et al*. 2001). Some potential sources of errors in simultaneous state and parameter estimation for induction motors with equations expressed in a stator-fixed reference

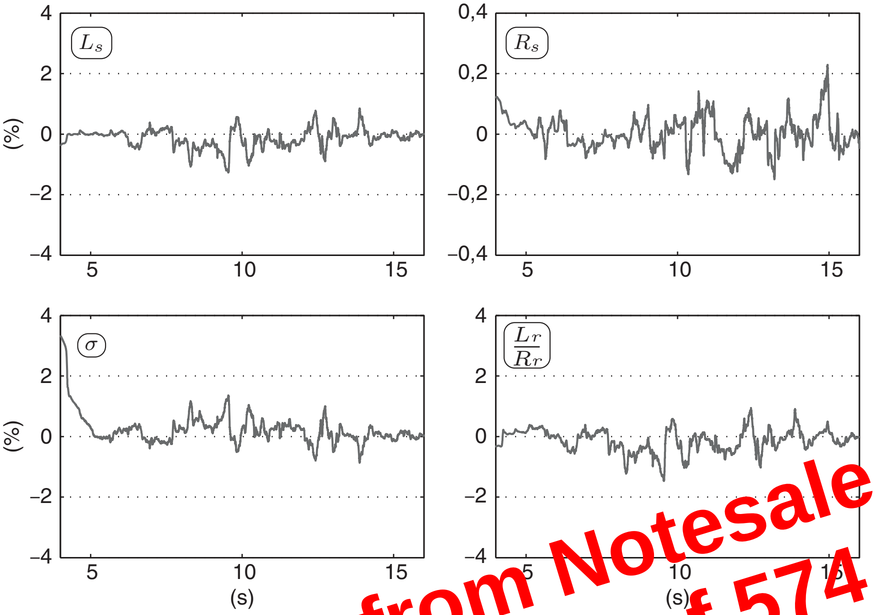

Figure 4.13 Relative estimation errors for the parameters under operation close to the inobservability line

of the relative estimation errors for the parameters in Figure 4.13. It is obvious that the unobservability condition is not rigorously fulfilled, as there are slight stator flux variations, mainly due to noise and errors propagating through the loop. It is nevertheless an operation close to the unobservability line and the results show that a sufficient excitation level can ensure observer stability even under conditions in which, theoretically, the system is on the verge of unobservability. It is worth remembering at this point that in the case of the exponential forgetting factor observer, the least singular value of S represents an indicator of the quantity of meaningful information that is present in the signals fed to the observer. This indicator can be monitored in real time in order to detect potentially critical situations for the observer.

4.5 Conclusions

In this chapter, various estimation problems related to the classical model of induction motors have been reviewed, at the light of (nonlinear) observer approaches for possible solutions. They include the basic problem of flux reconstruction, from stator currents and rotor speed measurements, as well as the analysis of the widely studied situation of estimation *without any speed sensor* (so-called sensorless configuration in the literature). The latter has also been extended to the case of possible unknown parameters, and various simulation results have been provided accordingly.

Although the formal analysis has been mostly provided on the basis of a continuous-time representation, some possible extensions to discrete-time have also been highlighted. Finally,

5

State Observers for Active Disturbance Rejection in Induction Motor Control

Hebertt Sira Ramírez[1], Felipe González Montañez[2], John Cortés Romero[3], and Alberto Luviano-Juárez[4]
[1]Department of Electrical Engineering, CINVESTAV-IPN, México
[2]Departamento de Energía, Universidad Autónoma Metropolitana, México
[3]Department of Electrical and Electronic Engineering, Universidad Nacional de Colombia, Colombia
[4]UPIITA-IPN, México

5.1 Introduction

Asymptotic estimation of perturbation inputs, with the aim of exactly, or approximately, canceling their influence on the system at the controller stage, has been treated in the existing literature under several headings: *disturbance accommodation control*, *active disturbance rejection control* (ADRC), and *intelligent Proportional–Integral–Derivative* (PID) *control*, also called, *model-free control*. In all these approaches, disturbances, whether state-dependent or not, are treated as a lumped single disturbance input that may be estimated online and then appropriately canceled by the controller. Roots of this line of work may be found in Shipanov (1939). Disturbance accommodation control is represented by the work of C.D. Johnson. Originally, the approach was cast in the context of linear systems (see Johnson 1971) and included a known linear model for the exogenous disturbances. The method, however, has been actively evolving, including extensions to discrete-time systems and to the decoupling of nonlinear systems (see Johnson (2008) for a survey). The ADRC method is represented by the works of the late Prof. Jingqing Han. The emphasis of this work lies on *nonlinear* observer-based disturbance estimation, for the canceling, and efficient time derivative calculations,

AC Electric Motors Control: Advanced Design Techniques and Applications, First Edition. Edited by Fouad Giri.

for the feedback (see, Han 2009). The original work of Han has been suitably extended and applied to various interesting technological fields by Z. Gao and his colleagues (see Gao 2001; Sun and Gao 2005; Gao 2006). The third methodology: model-free control, was developed by Fliess and Join (2008). This technique proposes controller design on the basis of one-dimensional, or at most two-dimensional, local phenomenological models (called *local ultra-models*) of the nonlinear plant. These models are online adapted to the actual plant via fast algebraic estimation and identification techniques characterized by frequent resettings. The theoretical support of this methodology stems from the differential algebraic viewpoint in linear and nonlinear systems (see Fliess *et al.* 2008). In recent years, the authors of this chapter have been involved in developing illustrative laboratory applications of the ADRC method for nonlinear systems using only linear feedback and linear observers, known as generalized proportional integral (GPI) observers, for simultaneous estimation of states and of nonlinear disturbances. The disturbances are viewed as an aggregation of exogenous and endogenous disturbances into a single time signal with no additional structure. The method thus proposes *global ultra-models* of the perturbed plant that require no online resettings. The approach is systematically used in the context of an input-output system description, regardless of the complexities of the nonlinear system. The method is circumscribed to either differentially flat systems, or to minimum phase systems (see Luviano-Juárez *et al.* 2010; Sira-Ramírez *et al.* 2009; Sira-Ramírez *et al.* 2012a; Sira-Ramírez *et al.* 2012b; Sira-Ramírez *et al.* 2012c).

GPI observers, a dual counterpart of GPI controllers (see Fliess *et al.* 1991), were introduced in Sira-Ramírez and Feliu-Battle (2011) in the context of sliding-mode observers for flexible robotics systems. The nonsliding version appears in Luviano-Juárez *et al.* (2010), as applied to chaotic systems synchronization. The linear GPI observer naturally incorporates a self-updating polynomial model of the overall disturbance effects as well as iterated output error integral injections aimed at attenuating the effects, on the estimation error dynamics, of lumped exogenous and state-dependent perturbation input signals present in the input-output model of the plant. GPI observers are capable of accurate online estimations of: (a) the output-related phase variables of the underlying pure integration input-output system obtained after disturbance cancelation, (b) the, nonlinear state-dependent, additive perturbation input signal itself, and (c) the estimation of a certain number of the perturbation input time derivatives (this allows a natural extension to the control of nonlinear input-delayed systems; Sira-Ramírez *et al.* 2010a).

This chapter is devoted to the GPI observer-based ADRC approach for trajectory tracking in induction motors subject to, both, external disturbance inputs and endogenous nonlinearities treated also as unknown disturbances. Two traditional control design techniques are cast into this context. Namely, the two stage (inner loop–outer loop) controller design and the direct armature voltage field-oriented controller. The fundamental advantage of this proposal lies in the single-handed cancelation of the effects of time-varying torques, and of unmodeled frictions and nonlinearities containing possibly uncertain parameters. For detailed background on induction motor control, we refer the readers to the excellent books by Trzynadlowski (1994), Leonhard (2001), Ortega *et al.* (1998), Chiasson (2005), and Marino *et al.* (2010). The chapter is organized as follows: Section 5.2 deals with the problem of controlling an induction motors using two observer-based ADRC loops, one for the current tracking task and a second one for the angular velocity regulation. Section 5.3 presents the armature voltage field-oriented controller for the decoupled regulation of the angular velocity and the flux magnitude. Both schemes present experimental results and comparisons with existing control strategies. Finally, For the theorem below, let the set of parameters, $\{\kappa_1^\psi, \kappa_0^\psi\}$, $\{\kappa_1^\omega, \kappa_0^\omega\}$, be such that the polynomials in the complex variable s, given by

$$p_{\psi,c}(s) = s^2 + \kappa_1^\psi s + \kappa_0^\psi, \quad p_{\omega,c}(s) = s^2 + \kappa_1^\omega s + \kappa_0^\omega, \tag{5.21}$$

are Hurwitz polynomials. Similarly, let the set of parameters, for some given integers n and m[1], $\{\gamma_{m+1}^\psi, \gamma_m^\psi, \ldots, \gamma_0^\psi\}$, $\{\pi_{n+1}^\omega, \pi_n^\omega, \ldots, \pi_0^\omega\}$, be such that the polynomials in the complex variable s, given by

$$\begin{aligned} p_{\psi,o}(s) &= s^{m+2} + \gamma_{m+1}^\psi s^{m+1} + \gamma_m^\psi s^m + \cdots + \gamma_0^\psi, \\ p_{\omega,o}(s) &= s^{n+2} + \pi_{n+1}^\omega s^{n+1} + \pi_n^\omega s^n + \cdots + \pi_0^\omega, \end{aligned} \tag{5.22}$$

are also Hurwitz polynomials, with roots located sufficiently far into the left half of the complex plane. Furthermore, let $\xi_\psi^{(m)}(t)$ and $\xi_\omega^{(n)}(t)$, be functions of time uniformly absolutely bounded by finite constants.

Theorem 5.3.1 *The armature voltage field-oriented controller,*

$$\begin{aligned} v_s &= v_{s\alpha} + j v_{s\beta} = \left(\frac{\hat{\phi}_r}{\hat{\psi}_r^{\,2}} \right) v, \quad v = v_a + j v_b, \\ v_a &= -\frac{L_r L_s \sigma}{2 R_r M_{sr}} \left[\widehat{\xi}_\psi + \kappa_1^\psi \widehat{\left(\frac{d\psi_r^2}{dt} \right)} + \kappa_0^\psi \left(\hat{\psi}_r^{\,2} - (\psi_r^*)^2 \right) \right], \\ v_b &= -\frac{J L_r L_s \sigma}{p M_{sr}} \left[\widehat{\xi}_\omega - \ddot{\omega}^*(t) + \kappa_1^\omega (\widehat{\dot{\omega}}_m - \dot{\omega}^*(t)) + \kappa_0^\omega \left(\omega_m - \omega^*(t) \right) \right], \end{aligned} \tag{5.23}$$

with $\widehat{\xi}_\psi$ *and* $\widehat{\left(\frac{d\psi_r^2}{dt}\right)}$ *given, respectively, by the variables* ϑ_1^ψ *and* ζ_2^ψ *generated by the following linear high-gain GPI observer:*

$$\begin{aligned} \dot{\zeta}_1^\psi &= \zeta_2^\psi + \gamma_{m+1}^\psi (\hat{\psi}_r^{\,2} - \zeta_1^\psi), \\ \dot{\zeta}_2^\psi &= \vartheta_1^\psi + \left(\frac{2 R_r M_{sr}}{L_r L_s \sigma} \right) v_a + \gamma_m^\psi (\hat{\psi}_r^{\,2} - \zeta_1^\psi), \\ \dot{\vartheta}_1^\psi &= \vartheta_2^\psi + \gamma_{m-1}^\psi (\hat{\psi}_r^{\,2} - \zeta_1^\psi), \\ \dot{\vartheta}_2^\psi &= \vartheta_3^\psi + \gamma_{m-2}^\psi (\hat{\psi}_r^{\,2} - \zeta_1^\psi), \\ &\vdots \\ \dot{\vartheta}_{m-1}^\psi &= \vartheta_m^\psi + \gamma_1^\psi (\hat{\psi}_r^{\,2} - \zeta_1^\psi), \\ \dot{\vartheta}_m^\psi &= \gamma_0^\psi (\hat{\psi}_r^{\,2} - \zeta_1^\psi), \end{aligned} \tag{5.24}$$

---

[1] The integers n and m are, in principle, sufficiently large, indicating the number of iterated output estimation error integral injections needed to attenuate the effect of unmodeled plant nonlinearities in the GPI observation error dynamics. In practice, however, they are small and chosen within the range of 3–5. We recall here a quote by J. von Neumann: "With four parameters I can fit an elephant, and with five I can make him wiggle his trunk!"

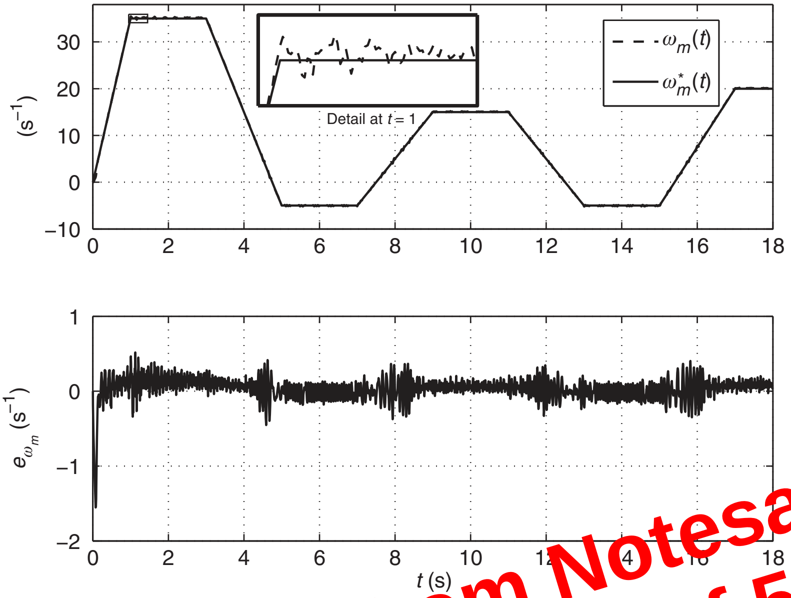

Figure 5.10 Angular velocity reference trajectory tracking and tracking error

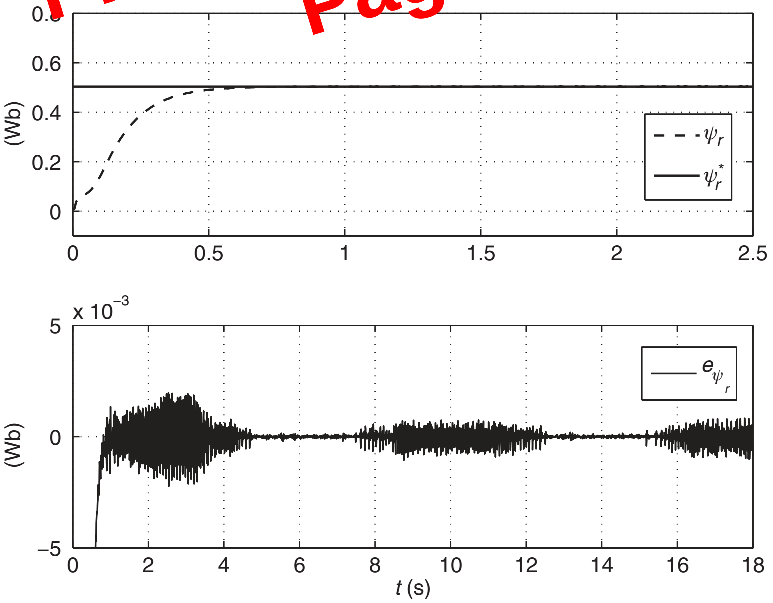

Figure 5.11 Flux magnitude regulation and its stabilization error

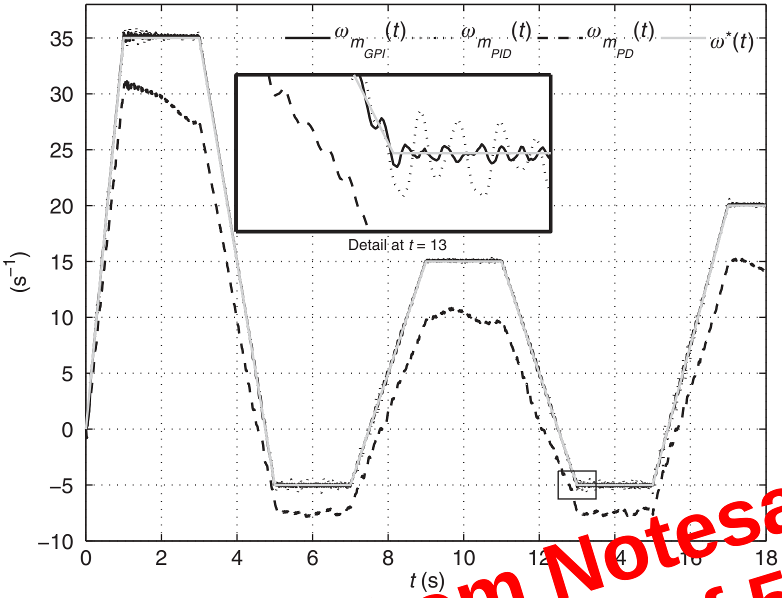

Figure 5.15 Performance comparison with PD and PID control schemes

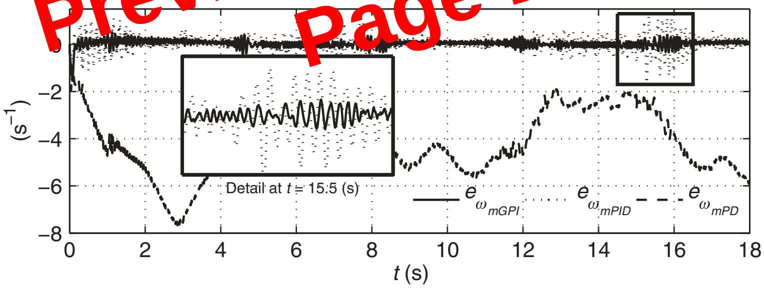

Figure 5.16 Performance comparison with PD and PID control schemes

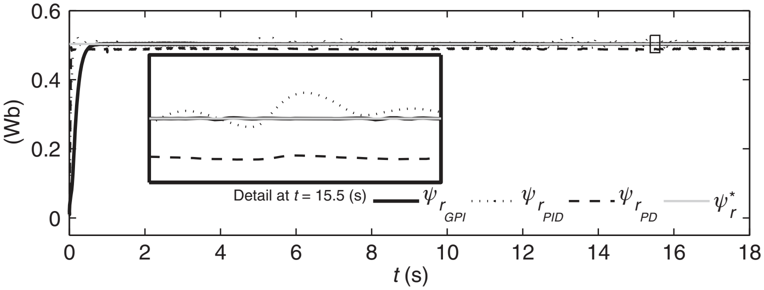

Figure 5.17 Performance comparison with PD and PID control schemes

Gliklikh YE (2006) Necessary and sufficient conditions for global -in-time existence of solutions of ordinary, stochastic and parabolic differential equations. *Abstract and Applied Analysis*, **2006**, 1–17.

Han J (2009) From pid to active disturbance rejection control. *IEEE Transactions on Industrial Electronics*, **56**, 900–906.

Hinkkanen M (2004) Flux estimators for speed sensorless induction motor drives. *PhD Thesis. Helsinki University of Technology* Institute of Intelligent Power Electronics Publications, Publication 9.

Johnson CD (1971) Accommodation of external disturbances in linear regulator and servomechanism problems. *IEEE Transactions on Automatic Control*, **AC-16**, 635–644.

Johnson CD (2008) Real-time disturbance-observers; origin and evolution of the idea. Part 1: the early years. *40th Southeastern Symposium on System Theory.* New Orleans, LA 88–91.

Karagiannis D, Astolfi A, Ortega R, and Hilairet M (2009) A nonlinear tracking controller for voltage–fed induction motors with uncertain load torque. *IEEE Transactions on Control Systems Technology*, **17**(3), 608–619.

Kim D, Ha I, and Ko M (1990) Control of induction motors via feedback linearization with input-output decoupling. *International Journal of Control*, **51**(4), 863–883.

Leonhard W (2001) *Control of Electrical Drives* Power Systems, edn. Springer, Berlin.

Luviano-Juárez A, Cortés-Romero J, and Sira-Ramírez H (2010) Synchronization of chaotic oscilators by means of proportional integral observers. *International Journal of Bifurcation and Chaos*, **20**(5), 1509–1517.

Maggiore M, and Passino K (2005) Output feedback tracking: a separation principle approach. *Automatic Control, IEEE Transactions,* **50**(1), 111–117.

Marino R, Tomei P, and Verrelli C (2010) *Induction Motor Control Design Advances in Industrial Control.* Springer-Verlag, London.

Martin P and Rouchon P (2000) Two simple flux observers for induction motors. *International Journal of Adaptive Control and Signal Processing*, **14**, 171–175. doi: 10.1002/(SICI)1099-1115(200003/05)14:2/3<171::AID-ACS583>3.0.CO;2-0.

Ortega R, Loría-Perez J, Nicklasson P, and Sira-Ramírez H (1998) *Passivity Based Control of Euler-Lagrange Systems Mechanical, Electrical and Electromechanical Applications Communications and Control Engineering*. Springer-Verlag, London.

Shipanov AG (1939) Theory and methods of designing automatic regulators. *Automatika in Telemekhanika*, **4**, 49–66.

Sira-Ramírez H, Luviano-Juárez A, and Cortés-Romero J (2012) Flatness-based linear output feedback control for disturbance rejection and tracking tasks on a Chua's Circuit. *International J. of Control*, **85** (accepted for publication, to appear).

Sira-Ramírez H, Núñez C, and Visairo N (2009) Robust sigma-delta generalised proportional integral observer based control of a 'buck' converter with uncertain loads. *International Journal of Control*, **83**(8), 1631–1640.

Sira-Ramírez H, Velasco-Villa M, and Rodríguez-Angeles A (2010) Trajectory tracking control of an input delayed monocycle. *American Control Conference 2009*, Baltimore USA.

Sira-Ramírez H, López-Uribe C, and Velasco-Villa M (2012a) Linear observer-based active disturbance rejection control of the omnidirectional mobile robot. *Asian Journal of Control*, (accepted for publication, to appear).

Sira-Ramírez H, Feliu-Batlle V (2011) Robust Σ - Δ modulation based sliding mode observers for linear systems subject to time polynomial inputs. *International Journal of Systems Science*, **42**(4), 621–631.

Sira-Ramírez H, Luviano-Juárez A, and Cortés-Romero J (2012b) Robust input-output sliding mode control of the buck converter. *Control Engineering Practice* (accepted for publication, to appear).

Sira-Ramírez H, Luviano-Juárez A, and Cortés-Romero J (2012c) Flatness-based linear output feedback control for disturbance rejection and tracking tasks on a Chua's Circuit. *International J. of Control*, **85**(5), 594–602.

Sira-Ramírez H, Ramírez-Neria M, and Rodríguez-Angeles A (2010b) On the linear control of nonlinear mechanical systems. *49th IEEE Conference on Decision and Control*, Atlanta, 1999–2004.

Sun B, and Gao Z (2005) A DSP-based active disturbance rejection control design for a 1-kW H-bridge DC–DC power converter. *IEEE Transactions on Industrial Electronics*, **52**(5), 1271–1277.

Tian G and Gao Z (2009) From Poncelet's invariance principle to active disturbance rejection. *American Control Conference, 2009. ACC '09.*, pp. 2451–2457, St. Louis, MO.

Trzynadlowski A (1994) *The Field Orientation Principle in Control of Induction Motors*. Kluwer Academic Publishers, Norwell, MA.

Verghese G and Sanders S (1988) Observers for flux estimation in induction machines. *IEEE Transactions on Industrial Electronics*, **35**(1), 85–94.

Table 6.1 AC machine parameters

Parameter	Definition
L_s	Stator self-inductance
L_r	Rotor self-inductance
L_m	Mutual inductance between stator and rotor windings
R_r	Rotor resistance
R_s	Stator resistance
τ_r	Rotor time constant

This model will also be noted in a shorter form,

$$\begin{cases} \dot{x} = f(x, v) + h(u_L), \\ y = Cx(t_k). \end{cases} \tag{6.49}$$

To be able to design a high-gain observer as in Corollary 6.3.2, we follow the method proposed by Dib *et al.* (2011) for the continuous-time case. The following change of variable is used:

$$z = \begin{pmatrix} z_1 \\ z_2 \\ z_3 \end{pmatrix} = g(x), \tag{6.50}$$

where z_1, z_2, and z_3 belong to $\mathbb{R}^2$, with

$$z_1 = g_1(x) = i, \tag{6.51}$$

$$z_2 = g_2(x) = kF(\omega_m)\Phi, \tag{6.52}$$

$$\begin{aligned} z_3 = g_3(x) = p\omega_m J_2 \left(-\frac{kL_m}{\tau_r} i + kF(\omega_m)\Phi \right) \\ + kp \left(\frac{kL_m}{JL_r} \Phi J_2 i + \frac{T_L}{J} \right) J_2 \Phi. \end{aligned} \tag{6.53}$$

We assume that the Jacobian of $g(x)$

$$\frac{\partial g}{\partial x} = \begin{pmatrix} I_2 & 0_2 & 0_2 \\ 0_2 & \dfrac{\partial g_2}{\partial \Phi} & \dfrac{\partial g_2}{\partial x_3} \\ \dfrac{\partial g_3}{\partial i} & \dfrac{\partial g_3}{\partial \Phi} & \dfrac{\partial g_3}{\partial x_3} \end{pmatrix} \tag{6.54}$$

is regular almost everywhere, which is true provided that $\Phi \neq 0$ and

$$\arctan\left(\frac{\Phi_\beta}{\Phi_\alpha} \right) - \arctan\left(p\tau_r\omega_m \right)$$

Table 7.1 Parameters specification of SPMSM and MRAS observer

SPMSM parameters	value	MRAS observer parameters	value
P_n	1.6 kW	α_1	80 000
ω_n	3000 rpm	α_2	80 000
U_n	540 V	λ_1	100
I_n	5.8 A	λ_2	100
R_s	2.06 Ω	K	700
L_s	9.15 mH	m	100
P	3		
ϕ_m	0.29 Wb		
J	0.0249 kgm^2		
f_v	0.0075 $\text{kgm}^2\text{s}^{-1}$		
T_l	5.1 Nm		

SPMSM, surface permanent-magnet synchronous motor; MRAS, model reference adaptive system.

motor speed (Figure 7.3 (dashed line)) where the synchronous motor operates at high and very low speeds.

Rotor Position Observation Results

For rotor position observation, the experimental results are displayed in Figure 7.4. The observed position (Figure 7.4 (solid line)) is obtained at high and very low frequencies according to Section 7.3.4 and tracks well the measured position (Figure 7.4 (dashed line)).

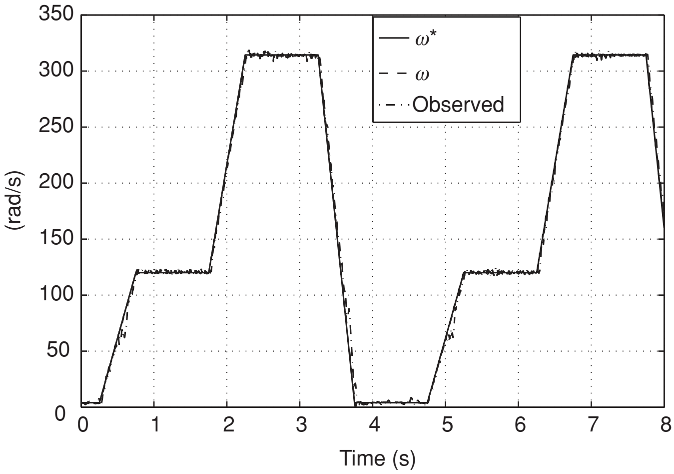

Figure 7.3 Rotor speed

angle, $\tan^{-1}(\hat{\lambda}_a, \hat{\lambda}_b)$, which are obtained from the flux observer (8.23), are different from the ones obtained when $\alpha_r = \alpha_{r0}$ and $\omega_0 = \omega$. However, for convenience, we continue to denote them by λ_d and ρ, which are now given by

$$\dot{\lambda}_d = -\alpha_{r0}\lambda_d + \alpha_{r0}Mi_d, \tag{8.24}$$

$$\dot{\rho} = p\omega_0 + \frac{\alpha_{r0}Mi_q}{\lambda_d}. \tag{8.25}$$

The stator current and voltage transformed to this estimated frame of reference are given by equation (8.17), with the newly calculated ρ. To calculate the developed torque in this estimated frame of reference we start again from equation (8.7)

$$T_d = \frac{pM}{L_r}(i_b\lambda_a - i_a\lambda_b). \tag{8.26}$$

Defining rotor flux errors in the stator frame of reference

$$e_a = \lambda_a - \hat{\lambda}_a, \quad e_b = \lambda_b - \hat{\lambda}_b, \quad \left[e_a, e_b\right]^T = F(-\rho)\left[e_d, e_q\right]^T, \tag{8.27}$$

and transforming the variables for the torque to the estimated frame of reference

$$\begin{bmatrix} i_a \\ i_b \end{bmatrix} = F(-\rho)\begin{bmatrix} i_d \\ i_q \end{bmatrix}, \quad \begin{bmatrix} \lambda_a \\ \lambda_b \end{bmatrix} = F(-\rho)\begin{bmatrix} \lambda_d \\ \lambda_q \end{bmatrix}, \tag{8.28}$$

and since $\lambda_q = 0$, we obtain

$$\begin{bmatrix} \lambda_a \\ \lambda_b \end{bmatrix} = F(-\rho)\left\{\begin{bmatrix} \lambda_d \\ 0 \end{bmatrix} + \begin{bmatrix} e_d \\ e_q \end{bmatrix}\right\}, \tag{8.29}$$

giving the torque equation using variables in the estimated frame of reference

$$T_d = \frac{pM}{L_r}\left[i_q\lambda_d + (i_q e_d - i_d e_q)\right]. \tag{8.30}$$

The stator currents i_d and i_q satisfy the equations

$$\dot{i}_d = p\,\omega_0 i_q + \alpha_r\beta\lambda_d - (\alpha_s\eta + \alpha_r\beta M)i_d + \alpha_{r0}Mi_q^2/\lambda_d + \gamma u_d + \alpha_r\beta e_d + p\,\beta\omega e_q, \tag{8.31}$$

$$\dot{i}_q = -p\,\omega_0 i_d - p\,\omega\beta\lambda_d - (\alpha_s\eta + \alpha_r\beta M)i_q - \alpha_{r0}Mi_d i_q/\lambda_d + \gamma u_q - p\,\beta\omega e_d + \alpha_r\beta e_q, \tag{8.32}$$

while the rotor flux errors e_d and e_q satisfy the equations

$$\dot{e}_d = -\alpha_r e_d + (p\,\omega_0 - p\,\omega + \alpha_{r0}Mi_q/\lambda_d)e_q + (\alpha_r - \alpha_{r0})(Mi_d - \lambda_d), \tag{8.33}$$

$$\dot{e}_q = -(p\,\omega_0 - p\,\omega + \alpha_{r0}Mi_q/\lambda_d)e_d - \alpha_r e_q + (\alpha_r - \alpha_{r0})Mi_q + p(\omega - \omega_0)\lambda_d. \tag{8.34}$$

where

$$f_1(\lambda_d, i_d, i_q, u_q, \omega_0) = p\,\omega_0 i_d + (\alpha_s \eta + \alpha_{r0}\beta M) i_q + \alpha_{r0} M i_d i_q/\lambda_d - \gamma u_q$$

is available online, and δ_3 and δ_4 are uncertain terms given by

$$\begin{aligned}\delta_3 &= -(\alpha_r - \alpha_{r0})\beta M i_q - p\,\beta\,\omega e_d + \alpha_r \beta e_q,\\ \delta_4 &= \mu(i_q e_d - i_d e_q) - T_L/J.\end{aligned}$$

We view i_q as the measured output and use it, together with the models (8.64) and (8.65), to build an observer to estimate ω. The high-gain observer of Section 8.3 can be designed if the uncertain terms appear only on the right-hand side of (8.65). The presence of δ_3 in (8.64) violates this condition. The change of variables

$$\begin{aligned}\Omega &= \omega - \frac{\delta_3}{p\,\beta\,\lambda_d}\\ &= \left(\frac{\lambda_d + e_d}{\lambda_d}\right)\omega + \frac{1}{p\,\beta\,\lambda_d}[(\alpha_r - \alpha_{r0})\beta M i_q - \alpha_r \beta e_q] \qquad (8.66)\end{aligned}$$

brings equations (8.64) and (8.65) into the form

$$\dot{i}_q = -p\,\beta\,\lambda_d \Omega - f_1(\lambda_d, i_d, i_q, u_q, \omega_0), \qquad (8.67)$$

$$\dot{\Omega} = \mu i_q \lambda_d + \delta_5, \qquad (8.68)$$

which is suitable for high-gain observer design, where

$$\begin{aligned}\delta_5 &= \delta_4 - \frac{d}{dt}\left(\frac{\delta_3}{p\,\beta\lambda_d}\right)\\ &\overset{\text{def}}{=} f_2(\lambda_d, i_d, i_q, \omega, u_q, e_d, e_q, T_L, \omega_0),\end{aligned}$$

and f_2 is a continuous function of its arguments. The change of variables (8.66) is invertible, provided $\lambda_d + e_d \neq 0$. We use the high-gain observer

$$\dot{\hat{i}}_q = -p\,\beta\lambda_d\hat{\Omega} - f_1(\lambda_d, i_d, i_q, u_q, \omega_0) + \left(\frac{\alpha_1}{\varepsilon}\right)(i_q - \hat{i}_q), \qquad (8.69)$$

$$\dot{\hat{\Omega}} = \mu i_q \lambda_d - \left(\frac{\alpha_2}{\varepsilon^2 p\,\beta\lambda_d}\right)(i_q - \hat{i}_q), \qquad (8.70)$$

where ε is a small positive parameter and α_1 and α_2 are positive constants that assign the roots of $s^2 + \alpha_1 s + \alpha_2 = 0$ at desired locations in the left-half plane. The scaled estimation errors

$$\xi_1 = \frac{i_q - \hat{i}_q}{\varepsilon}, \qquad \xi_2 = \Omega - \hat{\Omega}$$

to regulate λ_d to λ^*. Then, we design the PI current controller

$$\dot{\phi}_d = i_d - i_D \overset{\text{def}}{=} \tilde{i}_d, \qquad u_d = -K_d(\tau_d \tilde{i}_d + \phi_d), \tag{8.76}$$

for equation (8.74) to regulate i_d to i_D. With tight feedback loops, we can ensure the regulation of λ_d to λ^* for a wide range of variation of the variables (i_q, e_d, e_q) and the parameter α_r. The design should ensure that λ_d starts at a positive value and approaches λ^* monotonically so that λ_d is always positive. The initial condition of λ_d is determined by the initial condition of the observer (8.23), which is at our disposal.

Alternatively, we can approach the design of u_d as a nonlinear control problem for which a number of techniques are available to robustly regulate λ_d to λ^*. As an example, we describe a continuously implemented sliding-mode controller. Taking the sliding surface as

$$s_1 = M i_d - \lambda^*, \tag{8.77}$$

we can rewrite equations (8.73) and (8.74) as

$$\dot{\lambda}_d = -\alpha_{r0}\lambda_d + \alpha_{r0}\lambda^* + \alpha_{r0}s_1, \tag{8.78}$$

$$\begin{aligned} \dot{s}_1 = M[p\,\omega_0 i_q + \alpha_r\beta\lambda_d - (\alpha_s\eta + \alpha_{r0}\beta M)i_d + \alpha_{r0}M i_q^2/\lambda_d + \gamma u_d \\ + \alpha_r\beta e_d + p\,\beta\omega e_q] - \dot{\lambda}^*. \end{aligned} \tag{8.79}$$

Taking

$$u_d = \frac{1}{\gamma}[-p\,\omega_0 i_q - \alpha_{r0}\beta\lambda_d + (\alpha_s\eta + \alpha_{r0}\beta M)i_d - \alpha_{r0}M i_q^2/\lambda_d + \dot{\lambda}^*/M + v_d],$$

reduces the $\dot{s}_1$-equation to

$$\dot{s}_1 = M[v_d + \alpha_r\beta e_d + p\,\beta\omega e_q - (\alpha_r - \alpha_{ro})\beta M i_d].$$

The choice

$$v_d = -k_1 \text{sat}(s_1/\mu_1),$$

with

$$k_1 \geq k_0 + |\alpha_r\beta e_d + p\,\beta\omega e_q - (\alpha_r - \alpha_{ro})\beta M i_d|,$$

for some positive constants k_1 and k_0 and a small positive constant μ_1, ensures that

$$s_1\dot{s}_1 \leq -k_0 M|s_1|, \qquad \text{for } |s_1| \geq \mu_1,$$

which shows that, within finite time, s_1 and $|\lambda_d - \lambda^*|$ will be of the order $O(\mu_1)$. By choosing λ^* and the initial condition $\lambda_d(0)$, it can be ensured that λ_d will be always positive.

where δ_6 is an uncertain term whose components are proportional to e_d, e_q, or $(\alpha_r - \alpha_{r0})$. Once again, for any bounded i_q the flux errors e_d and e_q will be bounded and, after some finite time, their ultimate bounds will be proportional to $\sqrt{|\alpha_r - \alpha_{r0}|}$. Thus, the design of u_q is a robust control problem for the equations (8.88), (8.89), and (8.90). Using the high-gain observer of Section 8.4.2 to estimate ω and $\dot{\omega}$, and relying on the performance recovery property of high-gain observers, we can proceed to design a state feedback control in terms of x_1, x_2, and x_3. A continuously implemented sliding-mode controller can be designed similar to the current-control scheme and with similar results. The details can be found in Khalil *et al.* (1996).

8.7 Speed Control without Mechanical Sensor

The goal is to design a feedback controller to regulate the speed ω to the speed reference ω^*. This time, however, we do not have measurements of θ and we use the high-gain observer of Section 8.4.3 to estimate the speed. The flux observer (8.23) is implemented with $\omega_0 = \omega^*$ and we assume that flux λ_d has been regulated to a constant value λ^*. We rewrite equation (8.32) as

$$\dot{i}_q = -(\alpha_s\eta + \alpha_r\beta M)i_q - \alpha_{r0} i_q + \gamma u_q + d_2, \tag{8.93}$$

where

$$d_2 = -p\,\beta\omega\lambda^* - p\omega\lambda^*/M - -p\,\beta\omega e_d + \alpha_r\beta e_q$$

acts as a disturbance input. For any current command i_Q, we can design a state feedback controller for u_q, with sufficiently large gains, to regulate i_q to i_Q. Once again, the traditional approach (Leonhard 1996) uses the PI current controller

$$\dot{\phi}_q = i_q - i_Q \overset{\text{def}}{=} \tilde{i}_q, \qquad u_q = -K_q(\tau_q\tilde{i}_q + \phi_q). \tag{8.94}$$

This allows us to view i_Q as the control input. Thus, the motor dynamics can be described by the third order model

$$\dot{e}_d = -\alpha_r e_d + (p\omega^* - p\omega + \alpha_{r0}Mi_Q/\lambda^*)e_q, \tag{8.95}$$

$$\dot{e}_q = -(p\omega^* - p\omega + \alpha_{r0}Mi_Q/\lambda^*)e_d - \alpha_r e_q + (\alpha_r - \alpha_{r0})Mi_Q + p(\omega - \omega^*)\lambda^*, \tag{8.96}$$

$$\dot{\omega} = \mu[i_Q(\lambda^* + e_d) - e_q\lambda^*/M] - T_L/J, \tag{8.97}$$

$$\Omega = \left(\frac{\lambda^* + e_d}{\lambda^*}\right)\omega - \frac{\alpha_r e_q}{p\lambda^*} + a i_Q, \tag{8.98}$$

where Ω is viewed as the measured output and $a = (\eta - \hat{\eta})/(p\,\beta\lambda^*)$. In Khalil *et al.* (2009) it is shown how to apply the singular perturbation theory (Kokotović *et al.* 1999), to justify the model (8.95), (8.96), (8.97), and (8.98) when the gain K_q is sufficiently large.

The model (8.95), (8.96), (8.97), and (8.98) enables us to design the current i_Q as a feedback function of Ω to regulate ω to ω^*, and perform rigorous analysis of the nonlinear closed-loop errors in both rotor and stator resistance. Simulation and experiments on a 2HP squirrel-cage induction motor showed closeness between the results of a full and reduced model, made possible by the use of high-gain feedback. These were compared for 10% increase in R_s and R_r. The inability to maintain stability at steady state when $\omega_c \bar{i}_Q < 0$ as discussed earlier was demonstrated.

8.9 Conclusions

This chapter summarized the research conducted at Michigan State University to use high-gain observers and robust nonlinear techniques for the control of electric drives. The work has focused on field-oriented control of induction motors, but the same tools can be applied to other machines and different control strategies. One outcome of the experimental testing of the proposed control strategies is the confirmation that high-gain observers can be successfully implemented in electric drives with a sampling frequency in the range 10–20 kHz and with the typical measurement noise that results from using optical encoders.

References

Aloliwi B, Khalil HK, and Strangas EG (1997) Robust speed control of induction motors. *Proceedings of American Control Conference*, Albuquerque, NM WP16:4.

Aloliwi B, Khalil HK, and Strangas EG (2000) Robust speed control of induction motors: application to a benchmark example. *International Journal Adaptive Control and Signal Processing*, **14**, 157–170.

Atassi AN and Khalil HK (1999) A separation principle for the stabilization of a class of nonlinear systems. *IEEE Transactions on Automatic Control*, **44**, 1672–1687.

Davison EJ (1976) The robust control of a servomechanism problem for linear time-invariant multivariable systems. *IEEE Trans. Automat. Contr.*, **AC-21**(1), 25–34.

Khalil HK (2002) *Nonlinear Systems* 3rd edn. Prentice Hall, Upper Saddle River, NJ.

Khalil HK and Strangas EG (1996) Robust speed control of induction motors using position and current measurement. *IEEE Transactions on Automatic Control*, **41**, 1216–1220.

Khalil HK, Strangas EG, and Jurkovic S (2009) Speed observer and reduced nonlinear model for sensorless control of induction motors. *IEEE Transactions on Control Systems Technology*, **17**, pp. 327–339.

Ferrah A, Bradley KJ, and Asher GM (1992) Sensorless speed detection of inverter fed induction motors using slot harmonics and fast fourier transform. *Power Electronics Specialists Conference*, 279–286.

Kokotović PV, Khalil HK, and O'Reilly J (1999) *Singular Perturbations Methods in Control: Analysis and Design*. SIAM.

Leonhard W (1996) *Control of Electrical Drives* 2nd edn. Springer.

Novotony DW, Lipo TA, and Jahns TM (2010) *Introduction to Electric Machines and Drives*. University of Wisconsin.

Krishnan R (2001) *Electric Motor Drives*. Prentice Hall, Upper Saddle River, NJ.

Strangas EG, Khalil HK, Aloliwi B, *et al.* (1999). Robust tracking controllers for induction motors without rotor position sensor: analysis and experimental results. *IEEE Transactions on Energy Conversion*, **14**, 1448–1458.

9

Adaptive Output Feedback Control of Induction Motors

Riccardo Marino, Patrizio Tomei, and Cristiano Maria Verrelli
Dipartimento di Ingegneria Elettronica, Universitá di Roma "Tor Vergata", Italy

9.1 Introduction

Induction motors have definite advantages with respect to more expensive and less reliable electric motors such as direct-current ones: no commutator, no brushes, no rotor windings in squirrel-cage motors, capability of producing higher torques with lower weights, smaller size, and lower rotating masses. The availability of low-cost powerful digital signal processors and significant advances on power electronics allow for the design of complex induction motor (IM) controllers with the aim of achieving high performance on speed tracking and power efficiency. Flux sensors are typically not available so that an output feedback control problem is to be addressed, in which only the rotor speed and the stator currents are available from measurements. On the other hand, speed sensors may fail or be eliminated on purpose to increase reliability and noise immunity as well as to reduce cost and maintenance: in this case, the estimation and tracking control problem is called "sensorless" since only stator currents are assumed to be measured and available for feedback. Several difficulties naturally arise: motor dynamics are nonlinear and multivariable; measured outputs (stator currents for the sensorless case and stator currents/rotor speed for the output feedback case) do not coincide with the controlled outputs (rotor speed and flux modulus) that are required to track smooth bounded reference signals; three critical parameters, namely rotor and stator resistances (which vary during operations due to motor heating) and load torque (which depends on applications), are typically uncertain and are to be estimated online.

The sensorless estimation and tracking control problem with no use of nonrobust open-loop integration of flux dynamics (or equivalently rotor flux measurements) has been recently

---

AC Electric Motors Control: Advanced Design Techniques and Applications, First Edition. Edited by Fouad Giri.

addressed. Even though significant contributions can be found in Khalil *et al.* (2009), Lin *et al.* (2000), Marino *et al.* (2005, 2008), Montanari *et al.* (2006, 2007), (see also Zaky 2012; Traoré *et al.* 2012), the problem of designing an estimation and tracking control algorithm and of proving its closed-loop stability for sensorless IMs with uncertainties in load torque and stator and rotor resistances still remains open to the best of our knowledge. This constitutes an important problem in real applications since, as experimentally demonstrated in Montanari *et al.* (2006) (see also Mitronikas *et al.* 2001; Karanayil *et al.* 2007; Jadot *et al.* 2009; Hinkkanen *et al.* 2010), errors in estimating the stator resistance may lead to steady-state rotor speed and flux modulus tracking errors and even to instability, especially at low speeds.

Even when the rotor speed measurement is available for feedback (output feedback case) the corresponding theoretical estimation and tracking control problem can be still considered open: the available results in Behal *et al.* (2003), Fattah and Loparo (2001), Feemster *et al.* (2000), Jadot *et al.* (2009), Karagiannis *et al.* (2009), Marino *et al.* (1999), Peresada and Tonielli (2000), Peresada *et al.* (1999), and Vedagarbha *et al.* (1997) do not solve, via a priori verifiable persistency of excitation conditions, the critical case of output tracking in the presence of uncertain load torque, rotor and stator resistances. In particular: (1) only the case of known stator resistance is solved in Marino *et al.* (1999), in the presence, however, of not a priori verifiable persistency of excitation conditions; (2) only a qualitative sensitivity analysis of the persistency of excitation conditions is provided by Jadot *et al.* (2009) for the speed regulation (and not tracking) problem.

The aim of this chapter is to show that, under specific observability and identifiability conditions, solutions to the above sensorless and output feedback estimation and tracking control problems exist. They are constituted by dynamic nonlinear adaptive control algorithms that incorporate closed-loop observers for the unmeasured motor variables and closed-loop identifiers for the uncertain parameters (load torque and motor resistances). In particular, owing to the use of a sufficiently slow adaptation for the stator resistance estimate (see Montanari and Tilli (2006) and Jadot *et al.* (2009) for a similar approach to parameter estimation in IMs (Ha and Lee 2000) and for the identification of stator resistance from the generated torque at steady state, the closed-loop error system is guaranteed to be locally exponentially stable under: (1) persistency of excitation conditions, which may be interpreted in terms of rotor speed and flux observability and rotor resistance identifiability, and involve the rotor speed and flux modulus reference signals only; (2) conditions for the identifiability in first approximation of the stator resistance at steady state. Exponential rotor speed and flux modulus tracking is thus, in both cases, achieved along with exponential estimation of the unmeasured state variables and uncertain parameters.

Theoretical and simulative comparisons between the two presented controllers (sensorless control and output feedback one) are finally carried out in terms of persistency of excitation requirements and closed-loop performances: a time-varying rotor flux reference signal is no longer needed in the output feedback case (leading to the possibility of minimizing the power losses at steady state), while, as expected, transient performance are largely improved when the rotor speed signal is available for feedback.

9.2 Problem Statement

Assuming linear magnetic circuits, the dynamics of a balanced nonsaturated IM with one pole pair in a fixed reference frame attached to the stator are given by the well-known fifth order model (see, for instance, Krause 1986; Leonhard 2001; Marino *et al.* 2010)

$$\begin{aligned}
\frac{\mathrm{d}\omega_m}{\mathrm{d}t} &= \mu(\phi_{ra} i_{sb} - \phi_{rb} i_{sa}) - \frac{T_L}{J},\\
\frac{\mathrm{d}\phi_{ra}}{\mathrm{d}t} &= -\alpha\phi_{ra} - \omega_m\phi_{rb} + \alpha L_m i_{sa},\\
\frac{\mathrm{d}\phi_{rb}}{\mathrm{d}t} &= -\alpha\phi_{rb} + \omega_m\phi_{ra} + \alpha L_m i_{sb},\\
\frac{\mathrm{d}i_{sa}}{\mathrm{d}t} &= -\left(\frac{R_s}{\sigma} + \beta\alpha L_m\right) i_{sa} + \frac{1}{\sigma}v_{sa} + \beta\alpha\phi_{ra} + \beta\omega_m\phi_{rb},\\
\frac{\mathrm{d}i_{sb}}{\mathrm{d}t} &= -\left(\frac{R_s}{\sigma} + \beta\alpha L_m\right) i_{sb} + \frac{1}{\sigma}v_{sb} + \beta\alpha\phi_{rb} - \beta\omega_m\phi_{ra},
\end{aligned} \tag{9.1}$$

in which ω_m is the rotor speed, ϕ_{ra} and ϕ_{rb} are the rotor fluxes, i_{sa} and i_{sb} are the stator currents, ω_m, ϕ_{ra}, ϕ_{rb}, i_{sa}, and i_{sb} constitute the state variables, v_{sa}, and v_{sb} are the stator voltages (which constitute the control inputs) in a fixed reference attached to the stator; the outputs to be controlled are the rotor speed ω_m and the rotor flux modulus $\sqrt{\phi_{ra}^2 + \phi_{rb}^2}$. The model parameters are: load torque $T_L = T_{Ln} + \theta$, where $\theta \in [-\theta_m, \theta_m]$ denotes the constant uncertain variation from the constant nominal value T_{Ln} (T_L is typically uncertain since it depends on applications); (known) motor moment of inertia J; rotor and stator windings resistances R_r and R_s and (known) inductances L_r and L_s; and (known) mutual inductance L_m. To simplify notations we use the reparametrization: $\alpha = \frac{1}{T_r} = \frac{R_r}{L_r}$, $\beta = \frac{L_m}{\sigma L_r}$, $\mu = \frac{L_m}{J L_r}$, $\sigma = L_s(1 - \frac{L_m^2}{L_s Lr})$. Besides the load torque T_L, the parameters α and R_s are also assumed to be uncertain taking into account resistance variations during operations due to motor heating. If we introduce, as in Marino *et al.* (1999), an angle $\varepsilon_0(t)$, whose dynamics $\frac{d\varepsilon_0(t)}{dt} = \omega_0(t)$ will be later defined ($\varepsilon_0(0)$ is an arbitrary initial condition), we can equivalently consider the vectors $[\phi_{rd}, \phi_{rq}]^T$, $[i_{sd}, i_{sq}]^T$, and $[v_{sd}, v_{sq}]^T$, which are obtained by multiplying the corresponding (a, b) vectors $[\phi_{ra}, \phi_{rb}]^T$, $[i_{sa}, i_{sb}]^T$, and $[v_{sa}, v_{sb}]^T$ by the matrix $\mathcal{R}(\varepsilon_0) = \begin{bmatrix} \cos\varepsilon_0 & \sin\varepsilon_0 \\ -\sin\varepsilon_0 & \cos\varepsilon_0 \end{bmatrix}$. Such vectors contain the direct and quadrature components of rotor flux, stator current, and stator voltage vectors, respectively, with respect to a time-varying (d, q) reference frame rotating at speed $\omega_0(t)$ and identified by the angle $\varepsilon_0(t)$ in the fixed (a, b) reference frame. Using the state coordinates ($\omega_m, \phi_{rd}, \phi_{rq}, i_{sd}$ and i_{sq}) and the control variables (v_{sd} and v_{sq}) the motor dynamics (9.1) become (see, for instance, Krause 1986)

$$\begin{aligned}
\frac{\mathrm{d}\omega_m}{\mathrm{d}t} &= \mu(\phi_{rd} i_{sq} - \phi_{rq} i_{sd}) - \frac{T_L}{J},\\
\frac{\mathrm{d}\phi_{rd}}{\mathrm{d}t} &= -\alpha\phi_{rd} + (\omega_0 - \omega_m)\phi_{rq} + \alpha L_m i_{sd},\\
\frac{\mathrm{d}\phi_{rq}}{\mathrm{d}t} &= -\alpha\phi_{rq} - (\omega_0 - \omega_m)\phi_{rd} + \alpha L_m i_{sq},\\
\frac{\mathrm{d}i_{sd}}{\mathrm{d}t} &= -\left(\frac{R_s}{\sigma} + \beta\alpha L_m\right) i_{sd} + \frac{1}{\sigma}v_{sd} + \omega_0 i_{sq} + \beta\alpha\phi_{rd} + \beta\omega_m\phi_{rq},\\
\frac{\mathrm{d}i_{sq}}{\mathrm{d}t} &= -\left(\frac{R_s}{\sigma} + \beta\alpha L_m\right) i_{sq} + \frac{1}{\sigma}v_{sq} - \omega_0 i_{sd} + \beta\alpha\phi_{rq} - \beta\omega_m\phi_{rd}.
\end{aligned} \tag{9.2}$$

where Proj$[\zeta, \hat{\alpha}]$ is the projection algorithm (see, Marino *et al.* 2008) defined by

$$\text{Proj}[\zeta, \hat{\alpha}] = \begin{cases} \zeta, & \text{if } \alpha_m \le \hat{\alpha} \le \alpha_M; \\ \zeta, & \text{if } \hat{\alpha} < \alpha_m \text{ and } \zeta \ge 0; \\ \zeta, & \text{if } \hat{\alpha} > \alpha_M \text{ and } \zeta \le 0; \\ \xi_{\zeta 1}\zeta, & \text{if } \hat{\alpha} < \alpha_m \text{ and } \zeta < 0; \\ \xi_{\zeta 2}\zeta, & \text{if } \hat{\alpha} > \alpha_M \text{ and } \zeta > 0; \end{cases}$$

$$\xi_{\zeta 1} = 1 - \frac{{\alpha_m}^2 - \hat{\alpha}^2}{{\alpha_m}^2 - (\alpha_m - \varepsilon_\alpha)^2},$$

$$\xi_{\zeta 2} = 1 - \frac{\hat{\alpha}^2 - {\alpha_M}^2}{(\alpha_M + \varepsilon_\alpha)^2 - {\alpha_M}^2}.$$

The load torque uncertainty saturated estimate appearing in equations (9.8) and (9.9) is defined as

$$\text{sat}(\hat{\theta}) = \begin{cases} \hat{\theta}, & \text{if } 0 \le \hat{\theta} \le \theta_m; \\ \sum_{i=0}^{3} l_i \hat{\theta}^i, & \text{if } \theta_m < \hat{\theta} < \theta_m + \varepsilon; \\ \theta_m + \varepsilon, & \text{if } \hat{\theta} \ge \theta_m + \varepsilon; \end{cases}$$

$$l_0 = \frac{\theta_m^2(\theta_m + \varepsilon)}{\varepsilon^2}, \qquad l_1 = \frac{-2\theta_m\varepsilon - 3\theta_m^2 + \varepsilon^2}{\varepsilon^2},$$

$$l_2 = \frac{\varepsilon + 3\theta_m}{\varepsilon^2}, \qquad l_3 = -\frac{1}{\varepsilon^2},$$

in which sat(x) is a class $\mathcal{C}^1$ odd function that is linear in the closed set $[-\theta_m, \theta_m]$ and satisfies $|\text{sat}(x)| \le \theta_m + \varepsilon$ for all $x \in \Re$. The overall estimation and tracking control algorithm (9.7), (9.8), and (9.9) depends on: the available i_{sa} and i_{sb} measurements; the smooth bounded reference signals (ω_m^* and ϕ^*) and their bounded first and second order time derivatives; the known motor parameters J, L_r, L_s, and L_m; the known bounds $\theta_m, \alpha_m, \alpha_M, R_{sm}$, and R_{sM}; the positive control parameters $k_\omega, k_e, k, k_i, \lambda_1 \ne \lambda_2 \ne \lambda_3, \gamma_1, \gamma_2, \varepsilon_\alpha, \varepsilon_R$, and ε.

9.3.2 *Stability Analysis*

As in Marino *et al.* (2008), introduce the angle ε_0^* that satisfies

$$\dot{\varepsilon}_0^*(t) = \omega_m^*(t) + \frac{\alpha L_m}{\mu \phi^{*2}(t)}\left[\frac{T_L}{J} + \dot{\omega}_m^*(t)\right],$$

$$\varepsilon_0^*(0) = \varepsilon_0(0),$$

depending on the uncertain parameters α and T_L; define the tracking and estimation errors: $\tilde{\omega}_m = \omega_m - \omega_m^*$, $\tilde{\phi}_{rd} = \phi_{rd} - \phi^*$, $\tilde{\phi}_{rq} = \phi_{rq}$, $e_d = i_{sd} - i_{sd}^*$, $e_q = i_{sq} - i_{sq}^*$, $\tilde{i}_{sd} = i_{sd}$

where $s_\alpha, s_\beta, s_\gamma, p \in \Re^+$ *and the matrix* $Q_p(t)$ *is the solution of the linear matrix differential equation*

$$\begin{aligned}\dot{Q}_p(t) &= -Q_p(t) + \Gamma^T(t)\Gamma(t),\\ Q_p(0) &= \mathrm{e}^{-t_p} k_p I.\end{aligned}$$

The fluxes are estimated through the estimates $\hat{z}_d$ *and* $\hat{z}_q$ *of the auxiliary variables* $z_d = i_{sd} + \beta\phi_{rd}$ *and* $z_q = i_{sq} + \beta\phi_{rq}$ *whose dynamics*

$$\begin{aligned}\dot{z}_d &= -\frac{R_s}{\sigma} i_{sd} + \frac{1}{\sigma} v_{sd} + \omega_0 z_q,\\ \dot{z}_q &= -\frac{R_s}{\sigma} i_{sq} + \frac{1}{\sigma} v_{sq} - \omega_0 z_d\end{aligned}$$

depend on neither the unmeasured rotor speed ω_m *nor the uncertain parameter* α.

The design of the estimation law for $\hat{R}_s$ is based on the following stability analysis. The closed-loop error system can be written as

$$\begin{aligned}\dot{y} &= Q_1(y, t) + Q_2(y, t)\tilde{R}_s\\ &\doteq A_y(t)y + B_y(y, t)y + A_R(t)\tilde{R}_s + B_R(y, t)\tilde{R}_s,\end{aligned}$$

where

$$\begin{aligned}\lim_{\|y\|\to 0} \sup_{t\geq 0} \frac{\|B_y(y, t)y\|}{\|y\|} &= 0,\\ \lim_{\|[y, \tilde{R}_s]\|\to 0} \sup_{t\geq 0} \frac{\|B_R(y, t)\tilde{R}_s\|}{\|[y, \tilde{R}_s]\|} &= 0.\end{aligned}$$

Since, according to Marino *et al.* (2008), the origin of the unperturbed system (i.e., when $\tilde{R}_s = 0$)

$$\dot{y} = A_y(t)y + B_y(y, t)y$$

is locally exponentially stable, the origin of the linearized unperturbed system

$$\dot{\zeta} = A_y(t)\zeta$$

is exponentially stable (see Khalil 1996) so that there exists a function V_ζ such that

$$\begin{aligned} c_1\|\zeta\|^2 \le V_\zeta(\zeta,t) &\le c_2\|\zeta\|^2, \\ \frac{\partial V(\zeta,t)}{\partial t} + \frac{\partial V(\zeta,t)}{\partial \zeta}A_y(t)\zeta &\le -c_3\|\zeta\|^2, \\ \left\|\frac{\partial V(\zeta,t)}{\partial \zeta}\right\| &\le c_4\|\zeta\|, \end{aligned}$$

in terms of certain positive reals c_i, $1 \le i \le 4$.

As in Jadot *et al.* (2009) and Montanari and Tilli (2006) and in accordance with our simulation results, we assume that there exists, for any $\tilde{R}_s$ in a sufficiently small compact set (containing the origin), a steady-state solution $h(\tilde{R}_s,t)$ to the closed-loop error system. In particular, let $\overline{B_r(0)}$ be the closed ball centered at the origin with sufficiently small radius r and assume that for all $(\tilde{R}_s,t) \in \overline{B_r(0)} \times [0,+\infty)$ the following condition holds:

$\mathcal{A}$) there exists a smooth solution $h(\tilde{R}_s,t)$ to the nonlinear partial differential equation

$$\frac{\partial h(\tilde{R}_s,t)}{\partial t} = Q_1(h(\tilde{R}_s,t),t) + Q_2(h(\tilde{R}_s,t),t)\tilde{R}_s$$

with $h = [h_{\tilde{\omega}}, h_{\tilde{\phi}_{rd}}, h_{\tilde{\phi}_{rq}}, h_{e_d},$ [illegible], $h_{\tilde{i}_{sd}}, h_{\tilde{z}_a}, h_{\tilde{z}_b}, h_{\tilde{\alpha}}]^T$ $(h(\tilde{R}_s,t)$ being bounded on $\overline{B_r(0)} \times [0,+\infty)$ along with its first order partial derivatives) and satisfying

$$h(0,t) = 0, \qquad \forall\, t \ge 0.$$

We will look for a measurable steady-state solution component from which $\tilde{R}_s$ can be in first approximation identified. To this purpose, we first recall that $\beta e_{\phi d} = z_d - \hat{z}_d = \tilde{z}_d$, and $\beta e_{\phi q} = z_q - \hat{z}_q = \tilde{z}_q$, so that

$$\begin{bmatrix} \tilde{z}_a \\ \tilde{z}_b \end{bmatrix} = \begin{bmatrix} \cos\varepsilon_0^* & -\sin\varepsilon_0^* \\ \sin\varepsilon_0^* & \cos\varepsilon_0^* \end{bmatrix} \begin{bmatrix} \tilde{z}_d \\ \tilde{z}_q \end{bmatrix},$$

and we then consider the dynamics of $\tilde{z}_a$ and $\tilde{z}_b$. They only depend, in first approximation, on the measurable $\tilde{i}_{sd}$ and on the uncertain $\tilde{R}_s$, and they can be written as

$$\begin{aligned} \dot{\tilde{z}}_a &= \tilde{\omega}_0\tilde{z}_b - \frac{1}{\gamma_1}[\hat{\alpha}\cos\varepsilon_0^* - \omega_m^*\sin\varepsilon_0^*]\tilde{i}_{sd} - \frac{\tilde{R}_s}{\sigma}[i_{sd}\cos\varepsilon_0^* - i_{sq}\sin\varepsilon_0^*] \\ &\doteq p_a(y,t) - A_{za}(y,t)\tilde{R}_s - B_{za}(y,t)p(y), \\ \dot{\tilde{z}}_b &= -\tilde{\omega}_0\tilde{z}_a - \frac{1}{\gamma_1}[\hat{\alpha}\sin\varepsilon_0^* + \omega_m^*\cos\varepsilon_0^*]\tilde{i}_{sd} - \frac{\tilde{R}_s}{\sigma}[i_{sd}\sin\varepsilon_0^* + i_{sq}\cos\varepsilon_0^*] \\ &\doteq p_b(y,t) - A_{zb}(y,t)\tilde{R}_s - B_{zb}(y,t)p(y), \end{aligned}$$

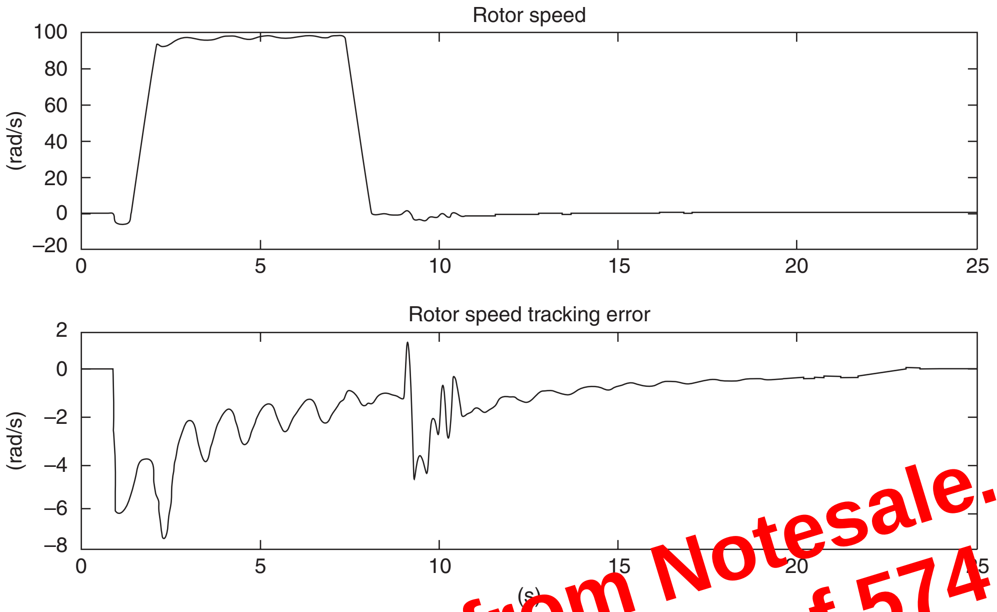

Figure 9.2 Sensorless case: rotor speed and corresponding tracking error

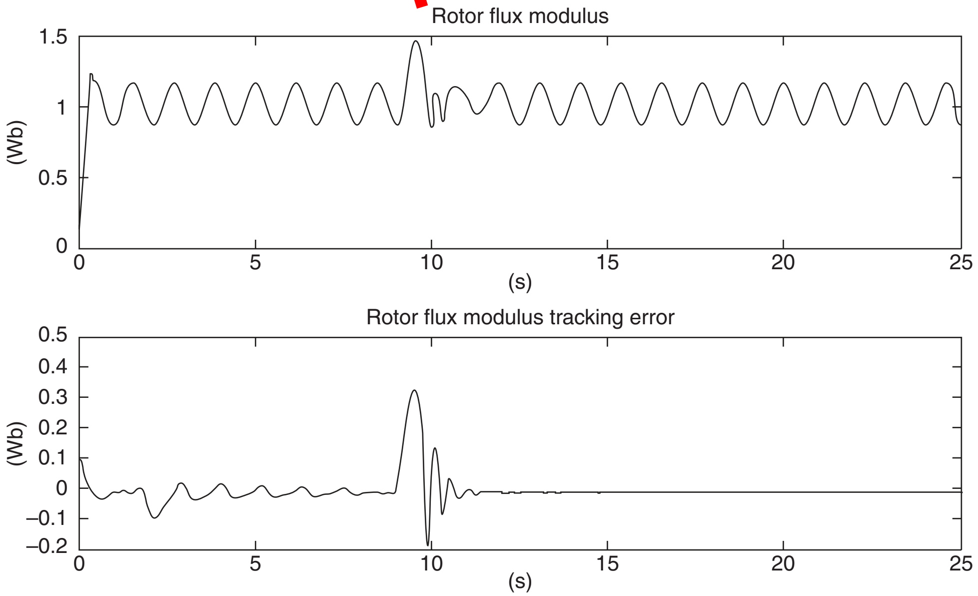

Figure 9.3 Sensorless case: rotor flux modulus and corresponding tracking error

From equations (10.3), (10.4), (10.5), and (10.9), the inductances L_s and L_r can be written as the sum of the leakage and the magnetizing inductances

$$L_s = l_s + L_m, \qquad L_r = l_r + L_m. \tag{10.10}$$

In induction motor analysis, the leakage inductances are usually grouped together either in the stator side or on the rotor side. Considering the first option, amounts to let $l_r = 0$ and $l_s = l_{seq}$. Then, equation (10.10) becomes

$$L_s = l_{seq} + L_m, \quad L_r = L_m, \quad \phi_r = \phi_\mu, \tag{10.11}$$

where l_{seq} is the equivalent inductance of both the stator and the rotor leakage brought to the stator side.

Induction Motor Model

Using the previous inductance expressions, it is shown in Ouadi *et al.* (2011) that, the induction machine dynamics are described in the α-β frame by the following model that accounts for magnetic saturation:

$$\frac{d\omega_m}{dt} = p\frac{L_m}{JL_r}(\phi_{r\alpha}i_{s\beta} - \phi_{r\beta}i_{s\alpha}) - \frac{T_L}{J} - \frac{F}{J}\omega_m, \tag{10.12}$$

$$\frac{di_{s\alpha}}{dt} = -\gamma i_{s\alpha} + \frac{L_m R_r}{\sigma L_s L_r^2}\phi_{r\alpha} + p\omega_m\frac{L_m}{\sigma L_s L_r}\phi_{r\beta} + \frac{1}{\sigma L_s}v_{s\alpha}, \tag{10.13}$$

$$\frac{di_{s\beta}}{dt} = -\gamma i_{s\beta} + \frac{L_m R_r}{\sigma L_s L_r^2}\phi_{r\beta} - p\omega_m\frac{L_m}{\sigma L_s L_r}\phi_{r\alpha} + \frac{1}{\sigma L_s}v_{s\beta}, \tag{10.14}$$

$$\frac{d\phi_{r\alpha}}{dt} = -\frac{R_r}{L_r}\phi_{r\alpha} + p\omega_m\phi_{r\beta} + \frac{R_r L_m}{L_r}i_{s\alpha}, \tag{10.15}$$

$$\frac{d\phi_{r\beta}}{dt} = -\frac{R_r}{L_r}\phi_{r\beta} - p\omega_m\phi_{r\alpha} + \frac{L_m R_r}{L_r}i_{s\beta}. \tag{10.16}$$

Replacing the stator, the rotor and the mutual inductances (L_s, L_r, and L_m) by their equivalent expressions given by equation (10.11), the above model simplifies to

$$\frac{d\omega_m}{dt} = \frac{p}{J}(\phi_{r\alpha}i_{s\beta} - \phi_{r\beta}i_{s\alpha}) - \frac{T_L}{J} - \frac{F}{J}\omega_m, \tag{10.17}$$

$$\frac{di_{s\alpha}}{dt} = -\gamma i_{s\alpha} + \frac{R_r}{l_{seq}}\kappa(\Phi_r)\phi_{r\alpha} + p\frac{1}{l_{seq}}\omega_m\phi_{r\beta} + \frac{1}{l_{seq}}v_{s\alpha}, \tag{10.18}$$

$$\frac{di_{s\beta}}{dt} = -\gamma i_{s\beta} + \frac{R_r}{l_{seq}}\kappa(\Phi_r)\phi_{r\beta} - p\frac{1}{l_{seq}}\omega_m\phi_{r\alpha} + \frac{1}{l_{seq}}v_{s\beta}, \tag{10.19}$$

$$\frac{d\phi_{r\alpha}}{dt} = -R_r\kappa(\Phi_r)\phi_{r\alpha} + p\omega_m\phi_{r\beta} + R_r i_{s\alpha}, \tag{10.20}$$

$$\frac{d\phi_{r\beta}}{dt} = -R_r\kappa(\Phi_r)\phi_{r\beta} - p\omega_m\phi_{r\alpha} + R_r i_{s\beta}, \tag{10.21}$$

designed using models that account for the magnetic circuit saturation. The approach of El Fadili *et al.* (2012) is revisited in the following text.

The first step is to find a relationship between the rotor flux norm and the stator current norm. In this respect, recall that the norms of all electrical quantities are invariant when passing from the $\alpha\beta$-coordinates to the dq-coordinates. Then, it makes sense for simplicity to conduct the present development within the oriented dq-coordinates frame. Indeed, within this reference frame, the flux q-component is null and all state variables are constant in steady state. That is, the dq-coordinate model described by equations (10.22), (10.23), (10.24), (10.25), and (10.26) is based upon. It turns out that, the machine electromagnetic torque T_{em} is simply expressed as follows:

$$T_{em} = p\phi_{rd} i_{sq} = p\Phi_r i_{sq}. \tag{10.29}$$

On the other hand, equation (10.25) simplifies to

$$\frac{\mathrm{d}\Phi_r}{\mathrm{d}t} = R_r i_{sd} - R_r \kappa(\Phi_r)\Phi_r, \tag{10.30}$$

yielding the steady-state current i_{sd},

$$i_{sd} = \kappa(\Phi_r)\Phi_r. \tag{10.31}$$

In turn, the stator current norm expression simplifies to

$$I_s = \sqrt{i_{sd}^2 + i_{sq}^2}. \tag{10.32}$$

Then, using equations (10.29), (10.30), (10.31), and (10.32), one gets the following expression of the electromagnetic torque:

$$T_{em} = p\Phi_r \sqrt{I_s^2 - (\kappa(\Phi_r)\Phi_r)^2}. \tag{10.33}$$

Figure 10.4 shows the curves representing the electromagnetic torque T_{em} versus the flux Φ_r, for various values of the stator current I_s. It is clearly seen that, to a given torque it corresponds a multitude of operation points differing by the value of the flux Φ_r and the current I_s. For instance, a torque $T_{em} = 20$ Nm can be produced, for the machine of Table 10.1, with

- a flux $\Phi_r = 0.5$ Wb and a current $I_s = 8.5$ A;
- a flux $\Phi_r = 0.37$ Wb and a current $I_s = 10$ A;
- a flux $\Phi_r = 0.21$ Wb and a current $I_s = 16$ A.

From an energetic viewpoint, the best operation point is one that involves the least current consumption. Let $T_{ei}(i = 1, \ldots, r)$ be a sufficiently large sample of relevant torque values. It is readily seen from Figure 10.4 that for any T_{ei}, there is a unique couple (Φ_{ri}, I_{si}) that involves the least possible stator current. That is, a set of couples (Φ_{ri}, I_{si}) can be obtained using with

$$\begin{aligned}\mu_2 = {} & c_1(-c_1z_1+z_3)+\ddot{\omega}_m^*+\frac{\dot{T}_L}{J}+\frac{F}{J}(\dot{\omega}_m^*-(-c_1z_1+z_3))\\ & -\frac{p}{J}((-R_r\kappa(\Phi_r)\phi_{r\alpha}+p\omega_m\phi_{r\beta}+R_ri_{s\alpha})i_{s\beta}\\ & +\phi_{r\alpha}\left(-\gamma i_{s\beta}+\frac{R_r}{l_{seq}}\kappa(\Phi_r)\phi_{r\beta}-p\frac{1}{l_{seq}}\omega_m\phi_{r\alpha}\right)\\ & -(-R_r\kappa(\Phi_r)\phi_{r\beta}-p\omega_m\phi_{r\alpha}+R_ri_{s\beta})i_{s\alpha}\\ & -\phi_{r\beta}\left(-\gamma i_{s\alpha}+\frac{R_r}{l_{seq}}\kappa(\Phi_r)\phi_{r\alpha}+p\frac{1}{l_{seq}}\omega_m\phi_{r\beta})\right). \end{aligned} \tag{10.51}$$

Similarly, it follows from equation (10.44) that z_4 undergoes the following differential equation:

$$\dot{z}_4=\dot{\nu}_1-R_r(\dot{i}_{s\alpha}\phi_{r\alpha}+i_{s\alpha}\dot{\phi}_{r\alpha}+\dot{i}_{s\beta}\phi_{r\beta}+i_{s\beta}\dot{\phi}_{r\beta}) \tag{10.52}$$

Using equations (10.17), (10.18), (10.19), (10.20), (10.21), and (10.42), it follows from equation (10.52):

$$\begin{aligned}\dot{z}_4 = {} & c_2\dot{z}_2+2\ddot{\Phi}_r^*\Phi_r^*+2R_r\dot{\kappa}(\Phi_r)\Phi_r+2R_r\kappa(\Phi_r)\dot{\Phi}_r)+2\dot{\Phi}_r^{*^2}\\ & -R_r\left(-\gamma i_{s\alpha}+\frac{R_r}{l_{seq}}\kappa(\Phi_r)\phi_{r\alpha}+p\frac{1}{l_{seq}}\omega_m\phi_{r\beta}+\frac{1}{l_{seq}}v_{s\alpha}\right)\phi_{r\alpha}\\ & +i_{s\alpha}((-R_r\kappa(\Phi_r)\phi_{r\alpha}+p\omega_m\phi_{r\beta}+R_ri_{s\alpha})\\ & +\left(-\gamma i_{s\beta}+\frac{R_r}{l_{seq}}\kappa(\Phi_r)\phi_{r\beta}-p\frac{1}{l_{seq}}\omega_m\phi_{r\alpha}+\frac{1}{l_{seq}}v_{s\beta}\right)\phi_{r\beta}\\ & +i_{s\beta}(-R_r\kappa(\Phi_r)\phi_{r\beta}-p\omega_m\phi_{r\alpha}+R_ri_{s\beta})), \end{aligned} \tag{10.53}$$

where the derivative $\dot{\kappa}(\Phi_r)$ is obtained from (10.27):

$$\dot{\kappa}(\Phi_r)=\frac{d\kappa}{d\Phi_r}\frac{\Phi_r}{dt}=\frac{d\kappa}{d\Phi_r}\left(\frac{\dot{\phi}_{r\alpha}}{\Phi_r}\phi_{r\alpha}+\frac{\dot{\phi}_{r\beta}}{\Phi_r}\phi_{r\beta}\right). \tag{10.54}$$

In turn, equation (10.53) is given the following compact form:

$$\dot{z}_4=\nu_2-\frac{R_r}{l_{seq}}(v_{s\alpha}\phi_{r\alpha}+v_{s\beta}\phi_{r\beta}), \tag{10.55}$$

with

$$\begin{aligned}\nu_2 = {} & (c_2(-c_2z_2+z_2))+2\ddot{\Phi}_r^*\Phi_r^*+2R_r\dot{\kappa}(\Phi_r)\Phi_r+2R_r\kappa(\Phi_r)\dot{\Phi}_r)+2\dot{\Phi}_r^{*^2}\\ & -R_r\left(-\gamma i_{s\alpha}+\frac{R_r}{l_{seq}}\kappa(\Phi_r)\phi_{r\alpha}+p\frac{1}{l_{seq}}\omega_m\phi_{r\beta}\right)\phi_{r\alpha}\end{aligned}$$

Specifically, one has:

$$\begin{aligned}\dot{\Phi}_r^* &= \frac{dF(I_s)}{dI_s}\frac{dI_s}{dt}\\ &= \frac{dF(I_s)}{dI_s}\left(\frac{\dot{i}_{s\alpha}i_{s\alpha}+\dot{i}_{s\beta}i_{s\beta}}{I_s}\right).\end{aligned} \tag{10.69}$$

$$\begin{aligned}\ddot{\Phi}_r^* &= \frac{d^2F(I_s)}{dI_s^2}\left(\frac{\dot{i}_{s\alpha}i_{s\alpha}+\dot{i}_{s\beta}i_{s\beta}}{I_s}\right)^2\\ &\quad+\frac{dF(I_s)}{dI_s}\left(\frac{\ddot{i}_{s\alpha}i_{s\alpha}+\dot{i}_{s\alpha}^2+\ddot{i}_{s\beta}i_{s\beta}+\dot{i}_{s\beta}^2}{I_s}\right)-\frac{\mathrm{d}F(I_s)}{\mathrm{d}I_s}\left(\frac{(\dot{i}_{s\alpha}i_{s\alpha}+\dot{i}_{s\beta}i_{s\beta})^2}{I_s^3}\right).\end{aligned} \tag{10.70}$$

Note that the derivatives $\frac{\mathrm{d}F(I_s)}{\mathrm{d}I_s}$ *and* $\frac{\mathrm{d}^2F(I_s)}{\mathrm{d}I_s^2}$ *are easily obtained due to the polynomial nature of equation (10.34).*

10.4 Simulation

This section illustrates the supremacy of the control strategy, involving the OFR optimizer, over control strategies with a CFR. The comparison is performed using a 7.5 kW induction machine whose characteristics are summarized in Table 10.1. The experimental protocol is described by Figures 10.6, 10.7, 10.8, and 10.9e. The applied load torque T_L (Figure 10.6) and rotor speed reference ω_m^* (Figure 10.7) are chosen so that the induction machine works in two very different zones of its magnetic characteristic. Recall that the nonlinear controller to be illustrated is described by: (1) the control laws (10.61); and (2) the flux reference optimizer (10.34). The following values of the controller design parameters proved to be suitable: $c_1 = 100$, $c_2 = 400$, $c_3 = 500$, and $c_4 = 1000$. The above controller will be compared with its simplified CFR version obtained keeping the flux reference constant equal to its nominal value, that is, $\Phi_r^* = 0.56$ Wb. To avoid confusion, the two controllers will be referred to OFR controller and CFR controller. The performances of both controllers are illustrated by Figures 10.7, 10.8, and 10.9. It is seen in Figure 10.7 that both controllers ensure a perfect asymptotic speed reference tracking despite the changes of load torque T_L. Figure 10.8 shows the resulting (state-dependent) OFR (for the OFR controller) and the CFR (for the simplified

Table 10.1 Numerical values of considered motor characteristics

Characteristic	Symbol	Value	Unity
Nominal power	P_N	7.5	kW
Nominal voltage	U_{sn}	380	V
Nominal flux	Φ_{rn}	0.56	Wb
Stator resistance	R_s	0.63	Ω
Rotor resistance	R_r	0.52	Ω
Inertia moment	J	0.22	Kgm^2
Friction coefficient	F	0.001	Nm s rad^{-1}
Number of pole pairs	p	2	
Leakage equivalent inductance	l_{seq}	7	mH

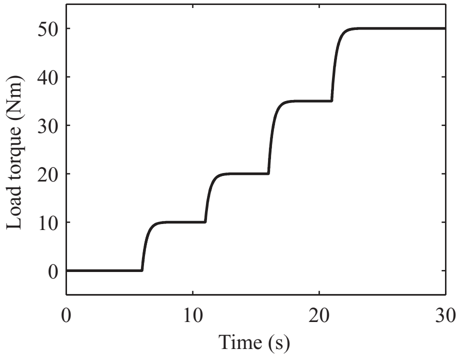

Figure 10.6 Applied load torque T_L (Nm)

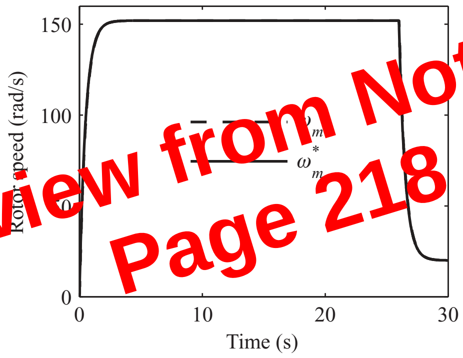

Figure 10.7 Rotor speed ω_m (rad/s) response: the identical speed responses obtained by the OFR controller and the constant flux controller

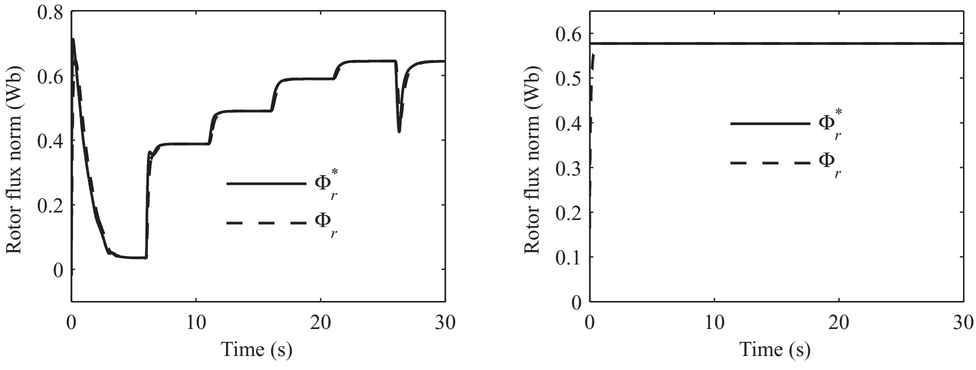

(a) OFR controller

(b) CFR controller

Figure 10.8 Flux tracking. Dashed, rotor flux reference; solid, measured flux response performance under different operation conditions. This drawback is mainly due to the IM observability property that can be lost under some operation conditions. For instance, in Ibarra-Rojas *et al.* (2004), the authors have demonstrated that the main conditions to lose the observability of IM are: the excitation voltages frequency is zero and the rotor speed is constant.

In this chapter, a comparative experimental study between nonlinear robust sensorless IM controllers, taking into account different operation conditions and under parametric uncertainties, is presented. The nonlinear controllers considered in the chapter are (a) a integral backstepping control (IBC) (Traore *et al.* 2012) and (b) a high-order sliding-mode control (HOSMC) (Traore *et al.* 2008). These control schemes are designed to improve the performance of the sensorless IM, at different operation conditions, in particular at low frequencies and in presence of unknown load torque.

Furthermore, to improve the performance of the backstepping control method, additional integral terms are introduced to improve the robustness properties of the controller in spite of uncertainties and perturbations.

Regarding the high-order sliding-mode (HOSM) speed-flux controller, a sliding manifold is designed in order to ensure finite-time convergence of sliding variable and its high-order time derivatives to zero in spite of uncertainties and disturbances.

For implementing such controllers and to reduce the number of sensors, an adaptive interconnected observer is designed for estimating of the fluxes, the speed, the load torque, and, moreover, the stator resistance.

Furthermore, experimental results comparing the performance of both control schemes are obtained on the framework of a specific sensorless IM benchmark (Benchmark 2005).

This chapter is organized as follows. Section 11.2 is devoted to the description of the IM model and the problem formulation. The robust integral backstepping is developed in Section 11.3. The HOSMC is presented in Section 11.4. To implement the proposed controller and to estimate the nonmeasured variables in Section 11.5, an adaptive interconnected observer design is introduced. Furthermore, experimental results are given and discussed related with the performance of the control schemes in Section 11.6. Finally, conclusions are drawn in Section 11.7.

11.2 Problem Formulation

In a rotating frame d- and q-axes (Chiasson 2005), the IM is described by

$$\begin{pmatrix} \dot{i}_{sd} \\ \dot{i}_{sq} \\ \dot{\phi}_{rd} \\ \dot{\phi}_{rq} \\ \dot{\omega}_m \end{pmatrix} = \begin{pmatrix} ba\phi_{rd} + bp\omega_m\phi_{rq} - \gamma i_{sd} + \omega_s i_{sq} + m_1 v_{sd} \\ ba\phi_{rq} - bp\omega_m\phi_{rd} - \gamma i_{sq} - \omega_s i_{sd} + m_1 v_{sq} \\ -a\phi_{rd} + (\omega_s - p\omega_m)\phi_{rq} + aL_m i_{sd} \\ -a\phi_{rq} - (\omega_s - p\omega_m)\phi_{rd} + aL_m i_{sq} \\ m(\phi_{rd} i_{sq} - \phi_{rq} i_{sd}) - c\omega_m - \frac{1}{J}T_l \end{pmatrix}, \tag{11.1}$$

where $i_{sd}, i_{sq}, \phi_{rd}, \phi_{rq}, v_{sd}, v_{sq}, \omega_m, T_l$, and ω_s, respectively, denote the stator currents, the rotor fluxes, the stator voltage inputs, the angular speed, the load torque, and the stator frequency. The subscripts s and r refer to the stator and rotor. The parameters $a = R_r/L_r$, $b = L_m/\sigma L_s L_r$, $c = F_v/J$, $\gamma = \frac{L_r^2 R_s + L_m^2 R_r}{\sigma L_s L_r^2}$, $\sigma = 1 - (L_m^2/L_s L_r)$, $m = pL_m/JL_r$, $m_1 = 1/\sigma L_s$, that these uncertainties are bounded. The control input u reads as (note that matrix φ_β^{Nom} is invertible on the work domain ($\phi_{rd} \neq 0$))[1]

$$\begin{pmatrix} v_{sd} \\ v_{sq} \end{pmatrix} = \varphi_\beta^{Nom^{-1}} \left\{ -\begin{pmatrix} \varphi_{\alpha_1}^{Nom} \\ \varphi_{\alpha_2}^{Nom} \end{pmatrix} + \begin{pmatrix} v_{sd} \\ v_{sq} \end{pmatrix} \right\}. \tag{11.21}$$

From equations (11.16), (11.17), (11.18), (11.19), (11.20), and (11.21), switching variables dynamics read as

$$\begin{pmatrix} \phi_{rd}^{(2)} & \omega_m^{(2)} \end{pmatrix}^T = \Psi_\alpha + \Psi_\beta \begin{pmatrix} v_{sd} & v_{sq} \end{pmatrix}^T. \tag{11.22}$$

$\varphi_{\alpha_1}^{Nom}$, $\varphi_{\alpha_1}^{Nom}$, and φ_β^{Nom} are bounded C^1-functions in the operation domain D of IM, which implies that Ψ_α and Ψ_β are uncertain bounded C^1-functions. Then, one gets

$$\begin{pmatrix} \sigma_\phi^{(3)} \\ \sigma_{\omega_m}^{(3)} \end{pmatrix} = \underbrace{\dot{\Psi}_\alpha + \dot{\Psi}_\beta \begin{pmatrix} v_{sd} \\ v_{sq} \end{pmatrix} - \begin{pmatrix} \phi_{rd^*}^{(3)} \\ \omega_m^{*\,(3)} \end{pmatrix}}_{\varphi_1} + \underbrace{\Psi_\beta}_{\varphi_2} \begin{pmatrix} \dot{v}_{sd} \\ \dot{v}_{sq} \end{pmatrix}$$

The control law synthesis is made in two steps: the design of the switching variable and the discontinuous input.

11.4.1 *Switching Vector*

From equation (29) and Theorem 3 in Traore *et al.* (2008), the switching vector reads as

- *For* $t \leq t_F$. $S_\phi = \sigma_\phi^{(2)} - \chi_\phi$, and $S_{\omega_m} = \sigma_{\omega_m}^{(2)} - \chi_{\omega_m}$ with

$$\begin{aligned} \chi_\phi &= K_\phi F^2 e^{Ft} T \sigma_\phi(0) - 2\zeta_\phi \omega_{n\phi}(\dot{\sigma}_\phi - K_\phi F e^{Ft} T \sigma_\phi(0)) - \omega_{n\phi}^2(\sigma_\phi - K_\phi e^{Ft} T \sigma_\phi(0)), \\ \chi_{\omega_m} &= K_{\omega_m} F^2 e^{Ft} T \sigma_{\omega_m}(0) - 2\zeta_{\omega_m} \omega_{n\omega_m}(\dot{\sigma}_{\omega_m} - K_{\omega_m} F e^{Ft} T \sigma_{\omega_m}(0)) \\ &\quad - \omega_{n\omega_m}^2(\sigma_{\omega_m} - K_{\omega_m} e^{Ft} T \sigma_{\omega_m}(0)). \end{aligned}$$

- *For* $t > t_F$. $S_\phi = \sigma_\phi^{(2)} + 2\zeta_\phi \omega_{n\phi} \dot{\sigma}_\phi + \omega_{n\phi}^2 \sigma_\phi$ and $S_{\omega_m} = \sigma_{\omega_m}^{(2)} + 2\zeta_{\omega_m} \omega_{n\omega_m} \dot{\sigma}_{\omega_m} + \omega_{n\omega_m}^2 \sigma_{\omega_m}$,

with

$$\begin{aligned} K_\phi &= \left[\sigma_\phi^{(2)}(0) 0 \dot{\sigma}_\phi(0) 0 \sigma_\phi(0) 0 \right] \cdot K_\phi^{-1}, \\ K_{\omega_m} &= \left[\sigma_{\omega_m}^{(2)}(0) 0 \dot{\sigma}_{\omega_m}(0) 0 \sigma_{\omega_m}(0) 0 \right] \cdot K_{\omega_m}^{-1}, \end{aligned}$$

---

[1] The interest of a such feedback is that it allows to minimize gain values of the control discontinuous function.

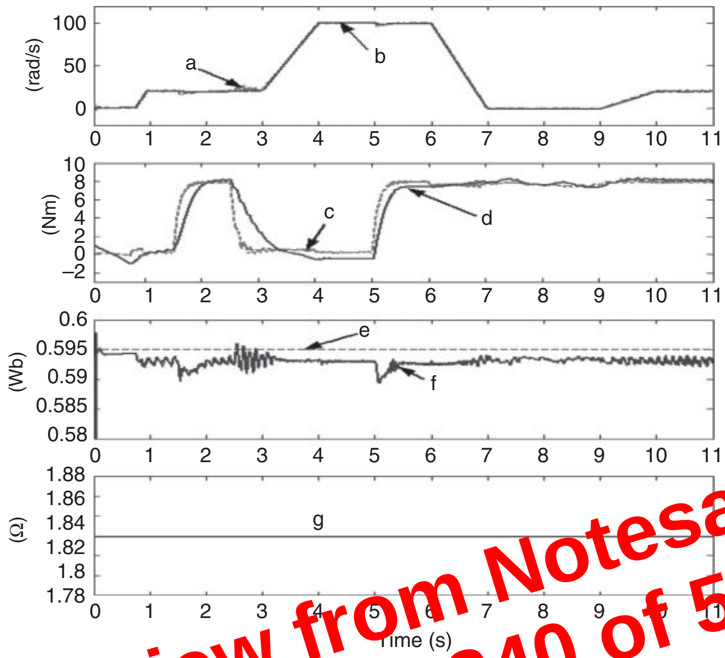

Figure 11.9 Integral backstepping control (IBC), +10% of L_s; a, c, measured speed and load torque; e, reference flux; b, d, f, g, observed speed, torque, flux (ϕ_{rd}), and stator resistance

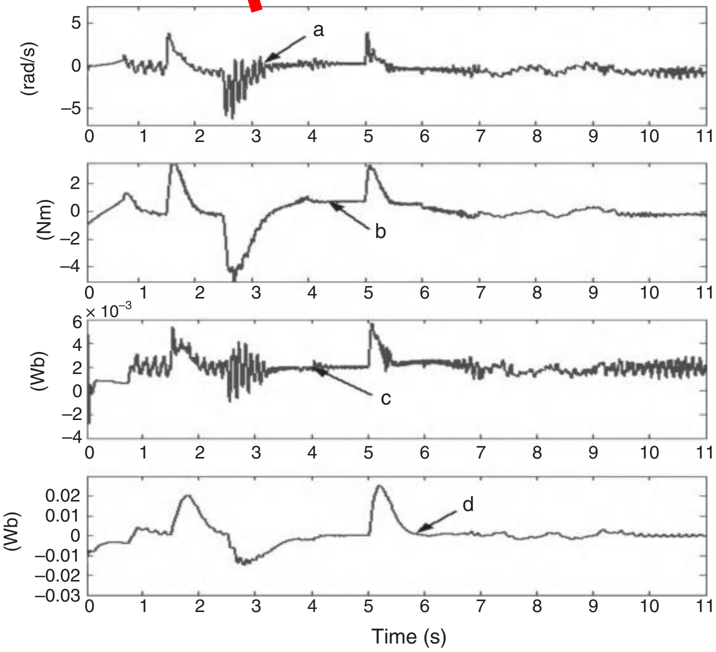

Figure 11.10 Integral backstepping control (IBC), +10% of L_s; a, b, speed and load torque estimation errors; c, d, flux tracking error (ϕ_{rd}) and flux angle error (ϕ_{rq})

rejected excepted at the time when it is applied (Figure 11.11h and j at time 1.5 s and 5 s) and when it is removed (Figure 11.11h, j at time 2.5 s). In Figure 11.11g, it can be viewed that the stator resistance estimation remains almost constant despite noise and transient dynamics of speed and load torque. This test shows the capability of the proposed controller to guarantee flux and speed tracking of slowly varying speed reference with excitation frequency close to zero (between 7 and 9 s).

Robustness Tests

+50% rotor resistance variation (R_r): The robustness of the observer-controller scheme is confirmed by the result obtained with rotor resistance variation (+50%) applied to the observer and controller parameters Figure 11.12 (evaluation of robustness with respect to inductances variations has also been successfully made). The increase of the rotor resistance value does not affect the performance of the speed trajectories tracking, when the observability conditions of are verified. It shows a static error when the motor is under unobservable condition (between 7 and 9 s) (Figure 11.12a, b). The static error transitory increases when the load torque is applied at time 1.5 s and 5 s (Figure 11.12h, j).

+10% rotor inductance variation (L_r): Robustness tests are made with variation of rotor inductance (+10%). The results of these tests are shown on Figure 11.13. The rotor inductance

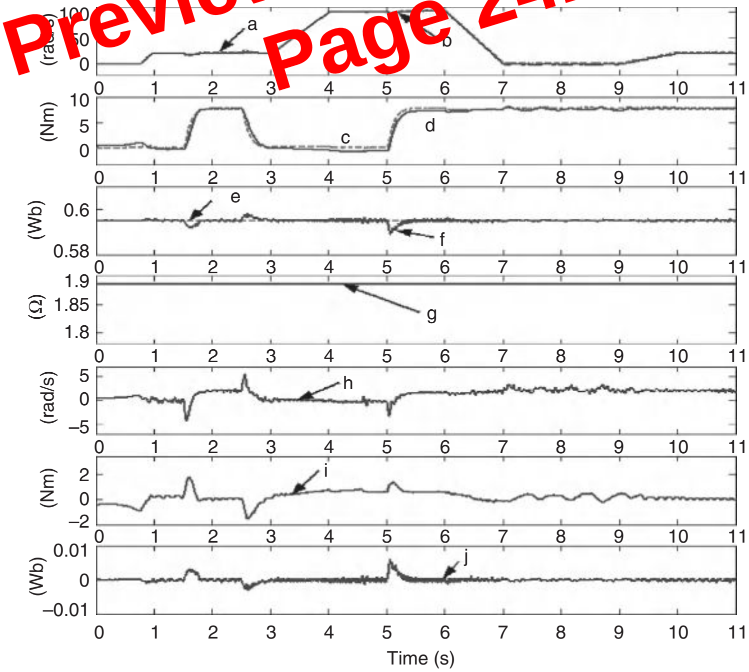

Figure 11.12 HOSM, rotor resistance variation (+50%); a, b, estimated and measured speeds; c, d, measured and estimated load torques; e, f, reference and estimated fluxes; g, estimated stator resistance; h, speed error; i, torque error; j, flux error versus time

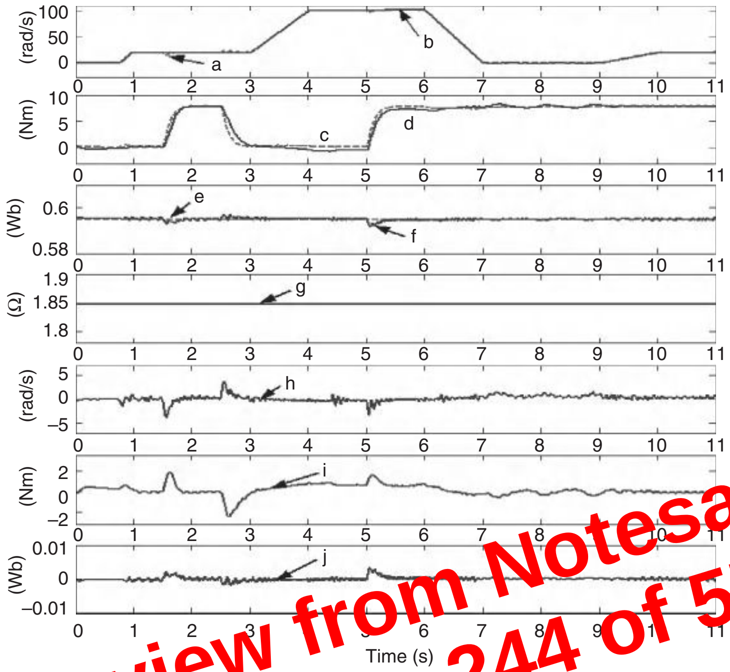

Figure 11.1[illegible] HOSM: stator inductance variation (+[illegible]0%); a, b, estimated and measured speeds; c, d, measured and estimated load torques; e, f, reference and estimated fluxes; g, estimated stator resistance; h, speed error; i, torque error; j, flux error versus time

The HOSM and the IBCs are implemented and validated experimentally on the same IM setup and use the same electromechanical model for the control design.

11.7.1 High-Order Sliding-Mode Control

It is well known that the success of the SM control applied to IM drives is due to its disturbance rejection and robustness. The HOSM control introduced in Section 11.4 is characterized by:

Advantages

1. *Convergence properties:* Finite-time convergence is achieved. The time of convergence can be fixed a priori.
2. Stability and robustness despite uncertainties.

Limitations

1. Tuning difficulty.
2. *Computational effort:* The control design requires a mayor computational effort and difficulties for the experimental implementation.
3. *Transient performance:* High-frequency signal components.

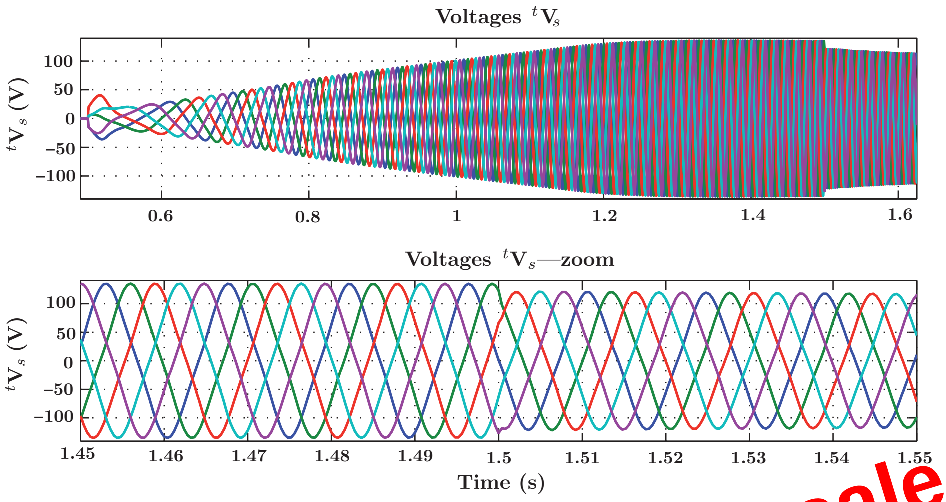

Figure 12.12 Stator voltages in the original reference frame Σ_t during the velocity rising ramp (for a color version of this figure, please see color plates.)

contributions. The generated mechanical torque τ_m and the applied load torque profile τ_e are shown in Figure 12.14. For $t \in [0, 0.5]$ and $t \in [3.5, 4]$ the torque τ_m is null because no load torque τ_e is applied and no velocity is tracked, while for $t \in [0.5, 1.5]$ and $t \in [2.5, 3.5]$ the torque τ_m evolves according to the load torque profile τ_e and to the velocity rising and falling transients (see Figure 12.9).

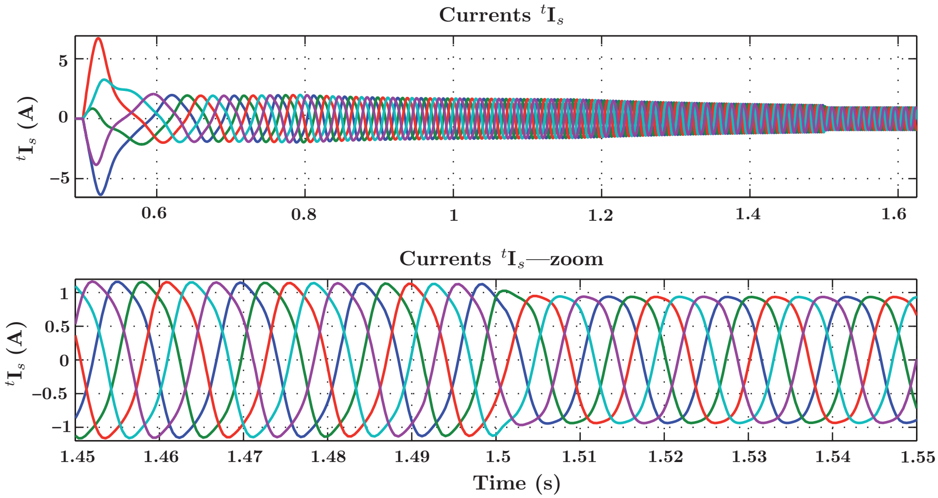

Figure 12.13 Stator currents in the original reference frame Σ_t during the velocity rising ramp (for a color version of this figure, please see color plates.)

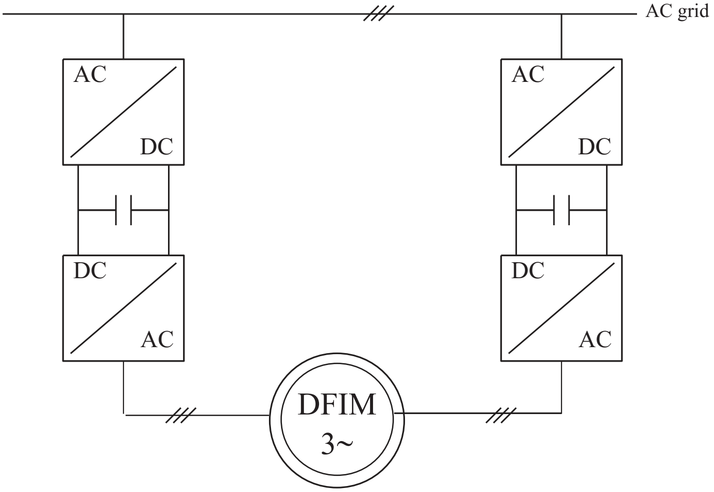

Figure 13.1 DFIM supplied by tow inverters in stator and rotor

control inputs, yielding four freedom degrees (Ourici 2012). The second configuration is one where the DFIM is controlled from the rotor (Figure 13.2). Then, a single bidirectional pulse-width modulation (PWM) power converter is implemented on the rotor, while the stator side is directly connected to the power grid (Verma *et al.* 2010). This configuration is suitable for applications involving limited rotor speed variation around the synchronous speed value. Indeed, as the power supplied from the rotor (slip power) is proportional to the slip, only a small fraction of the overall system power can be handled by means of the rotor-side power

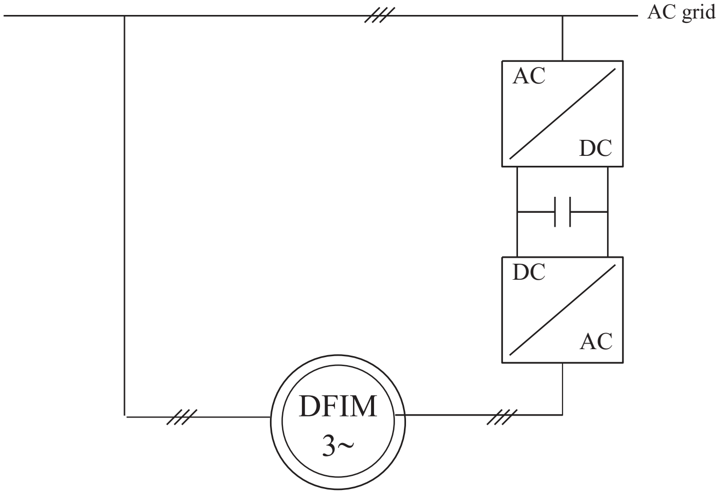

Figure 13.2 DFIM supplied by the rotor (inverter in rotor only)

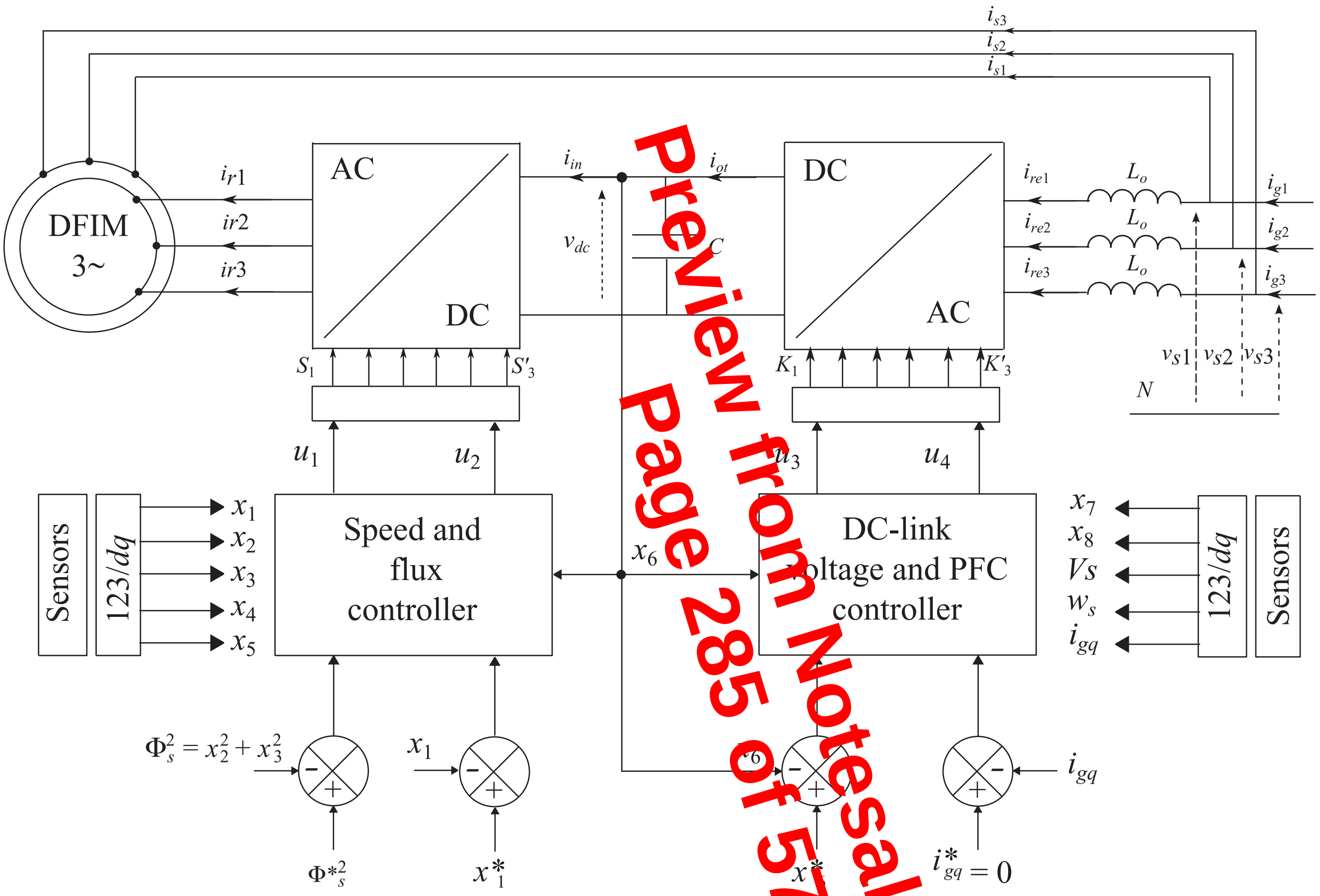

Figure 13.5 Control system including AC/DC/AC converters and a doubly-fed induction motor

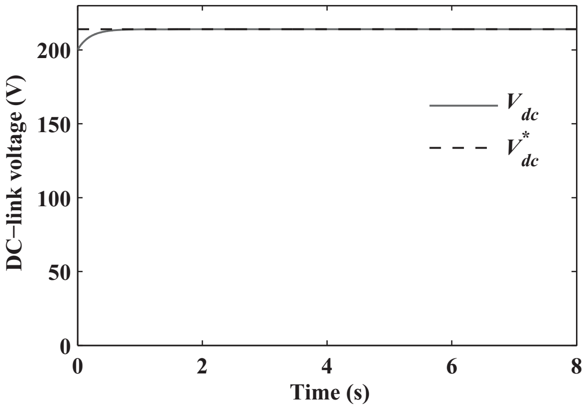

Figure 13.9 DC-link voltage v_{dc} (V)

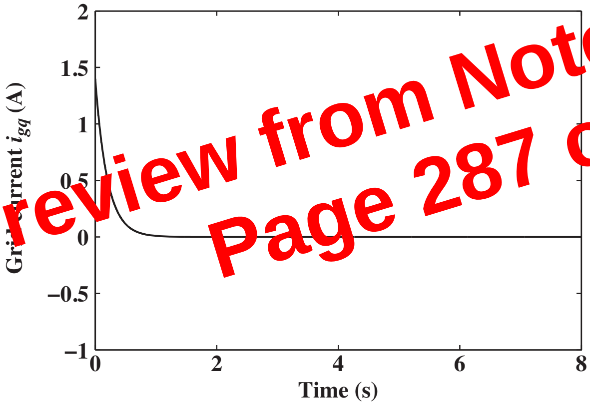

Figure 13.10 Grid current i_{gq} (A)

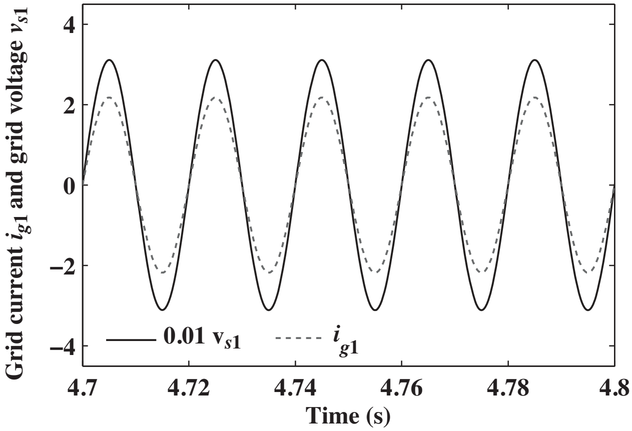

Figure 13.11 Unitary power factor checking in presence of a varying speed reference and load torque

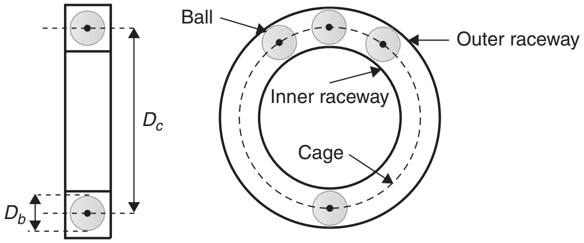

Figure 14.1 Geometry of a rolling-bearing

14.3 Model-Based FDI in IMs

14.3.1 Introduction

The model-based approach to FDI in automated processes has received considerable attention during the last two decades (Simani *et al.* 2003). The kernel of a model-based FDI algorithm is the generation of residual signals, which are indicators (symptoms) of the specific faults of interest. Ideally, each residual should selectively react to a specific fault only to allow fault isolation. Observer-based schemes were widely considered as residual generators, constructing the residual by a properly weighted output estimate error (Simani *et al.* 2003). In particular, when the system model admits significant degree of uncertainty, a particular class of nonlinear observer, the so-called *sliding-mode observers* (SMOs), appears to be an appropriate choice (Edwards *et al.* 2000; Simani *et al.* 2003; Pisano *et al.* 2008).

In this paper an observer-based FDI methodology is presented, which can detect the occurrence of broken bar fault (BBF) or eccentricity fault (EF) conditions. The method is based on a mathematical model of the motor under the considered faulty conditions, which represents the faults by means of suitably located fault injection signals. Its implementation requires the measurement of stator currents, shaft speed, and supply voltages, and the knowledge of the nominal motor electromechanical parameters. Noticeably, to overcome the uncertainty in the load torque, and to cope with, at the same time, the unknown fault injection signals, an unknown-input observation approach, robust to the presence of certain unmeasurable exogenous input terms, is taken. The framework of design relies on the so-called high-order SMO (Floquet *et al.* 2004; Fridman *et al.* 2007) and the suggested scheme is able to reconstruct at the same time both the fault injection signals and the load torque as well. The convergence property of the proposed algorithm will be supported by a Lyapunov-based stability proof.

A suitable residual is computed on the basis of the estimated fault injection signals, which can be processed by a threshold-based logic enabling a quick and computationally simple detection of the occurrence of the faulty conditions. The standard model describing the nominal (i.e., healthy) dynamics of the three-phase induction (wound-rotor or squirrel-cage) machine in the fixed (α, β) stator reference frame is expressed by the next fifth order nonlinear system (Krause and Thomas 1965; Marino *et al.* 1993):

$$\begin{cases} \dot{x}_1 = a_1\,(x_3x_4 - x_2x_5) - a_2x_1 + a_3T_L, \\ \dot{x}_2 = b_1x_4 - b_2x_2 + b_3x_1x_3 + b_4u_{s_\alpha}, \\ \dot{x}_3 = b_1x_5 - b_2x_3 - b_3x_1x_2 + b_4u_{s_\beta}, \\ \dot{x}_4 = c_1x_2 - c_2x_4 - n_px_1x_5, \\ \dot{x}_5 = c_1x_3 - c_2x_5 + n_px_1x_4, \end{cases} \tag{14.10}$$

The application of the HT to the analysis of faulty IMs has been considered, for example, in Liu *et al.* (2004) and Puche-Panadero *et al.* (2009).

Analytic Signal of the Current in a Healthy Machine

The steady-state phase current in an ideal machine, running at constant speed, is purely sinusoidal:

$$i(t) = I_m \cos(\omega t) = I_m \left(\frac{e^{j\omega t} + e^{-j\omega t}}{2} \right). \tag{14.31}$$

The FT of $i(t)$ shows two distinct components, at frequencies $f = \omega/2\pi$ and $f = -\omega/2\pi$, with an amplitude of $I_m/2$.

The AS corresponding to $i(t)$ is

$$\vec{i}(t) = i(t) + jHT(i(t)) = I_m(\cos(\omega t) + j\sin(\omega t)) = I_m e^{j\omega t}. \tag{14.32}$$

The FT of equation (14.32) will show a single spike corresponding to the positive frequency $f = \omega/2\pi$, with an amplitude double respect to the original signal spectrum component (14.31). The modulus of the AS reflects how the energy of $i(t)$ varies with time, and contains its low-frequency components. In the case of a healthy machine (14.32), it has a constant value of I_m, indicating that the energy of the phase current does not vary with time.

Analytic Signal of the Current in a Faulty Machine

In the case of periodic disturbances, like those produced by a broken bar in a motor that rotates at constant speed, the amplitude of the current in each phase is modulated with the principal frequency f_0 characteristic of the fault

$$i_b(t) = i(t)\left[1 + \beta\cos(\omega_0 t)\right], \tag{14.33}$$

where β denotes the modulation depth (modulation index) and $\omega_0 = 2\pi f_0$. By substituting (14.31) in (14.33)

$$i_b(t) = I_m \cos(\omega t)\left[1 + \beta\cos(\omega_0 t)\right]. \tag{14.34}$$

After performing the cosines multiplications, we get

$$i_b(t) = I_m \cos(\omega t) + \frac{\beta I_m}{2}\left[\cos\left((\omega - \omega_0)\, t\right) + \cos\left((\omega + \omega_0)\, t\right)\right], \tag{14.35}$$

which shows the presence of the two sideband frequencies characteristic of the fault. The HT of this current is constructed by changing the cosines functions by sine ones

$$HT(i_b(t)) = I_m \sin(\omega t) + \frac{\beta I_m}{2}\left[\sin\left((\omega - \omega_0)\, t\right) + \sin\left((\omega + \omega_0)\, t\right)\right], \tag{14.36}$$

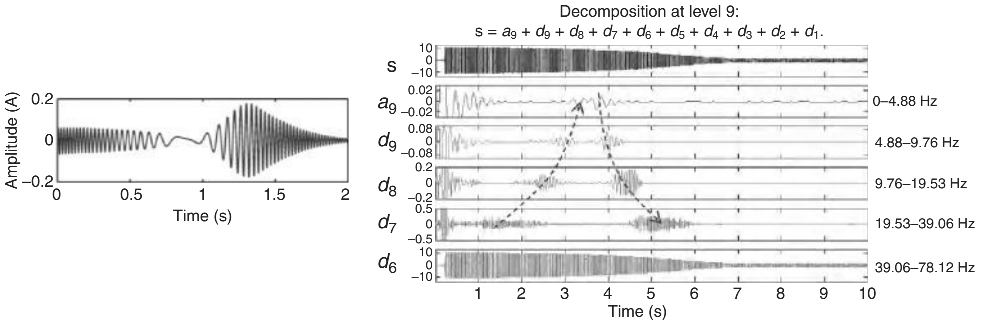

Figure 14.11 Theoretical evolution of the LSH component of the start-up current of a cage motor with one broken bar (left) and DWT of the start-up current of a machine with a broken bar (right), showing the characteristic pattern of low-frequency wavelets signals

14.6.3 Application of the DWT to the Analysis of the Start-up Current of a Motor with a Broken Bar in the Rotor

The previous test was repeated, but using a machine in which a rotor bar was artificially broken. Figure 14.10 (left) shows the DWT of the start-up current for this case. Comparison between Figures 14.10 (left) and 14.10 (right) shows that the bar breakage is clearly detected through the alteration of the approximation a_6 (or in general the approximation of the same level as that of the detail containing the fundamental component); the change in this signal, as justified in Riera-Guasp *et al*. (2008a), is caused by the left sideband component; its amplitude increases substantially when a rotor asymmetry is present and its frequency evolves during almost the whole start-up within the frequency band of a_6; the similitude between the waveform of the approximation a_6 and the theoretical evolution of the left sideband component during the start-up, deduced in Riera-Guasp *et al*. (2008b), which is shown in Figure 14.11 (left), should be highlighted. This fact makes the diagnosis based on the approximation signal very reliable, since it is very unlikely that the pattern in a_6 could be caused by a fault or perturbation different from a rotor asymmetry. An alternative way for detecting a rotor asymmetry is shown in Figure 14.11 (right); in this approach the number of DWT decomposition levels is increased up to 9 (3 more than the level of the detail signal containing the fundamental component). In this way, the evolution of the sideband along the start-up is spread across four consecutive wavelet signals ($d_7, d_8, d_9,$ and a_9), with frequency bands covering from near the main frequency to zero Hz. A clear pattern can be observed in these signals, which, according to the precedents sections, corresponds to a component with decreasing frequency in the time interval $1 < t < 3$ s and then, increasing frequency between $t = 3$ and $t = 6$. This also constitutes a reliable signature for the left sideband identification.

14.6.4 Diagnosis of a Machine with Mixed Eccentricity through the Start-up Current

Before carrying out this experimental investigation, it was necessary to prepare a motor introducing a certain degree of eccentricity in it. This was achieved by sanding down the inner and

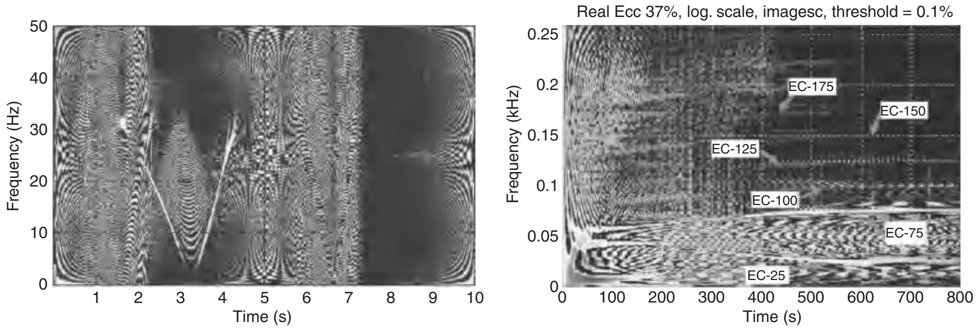

Figure 14.17 Wigner-Ville distribution of the start-up current of a machine with a broken bar (left) and of a machine with 37% eccentricity (right)

energy distribution is shown in Figure 14.17 (left); the characteristic "V" pattern associated to the LSH during start-up is clearly visible, leading to a diagnostic of faulty machine.

A more general and systematic methodology for the pretreatment of the signal before applying the WVD is proposed in Climente-Alarcon *et al.* (2011): In a first stage, the start-up current undergoes a filtering process; in this stage, a series of constant frequency components not related with the fault (fundamental component and winding harmonics) are filtered using optimized notch filters. Then, the HT is applied to the filtered signal to obtain an AS, whose spectrum does not contain negative frequencies. Finally, high- and low-pass filters are used for keeping only the range of frequencies of interest. In this way, the WVD is applied to a signal in which the more important components not related with the fault have been suppressed, and thus, the cross-terms are strongly reduced; as a result, the computed energy distribution enables appreciation of simultaneously several fault components evolving through a wide frequency band. As an example, Figure 14.17 (right) (Climente-Alarcon *et al.* 2011) shows the result of applying this methodology to the start-up current of a cage motor having a mixed eccentricity. The spectrogram shows the evolution of the couple of main eccentricity components ($f_1 \pm f_r$) designed as EC-25 clearly and EC-75 in Figure 14.17 (right). The trajectory in the $t-f$ plane of these components can be followed during the full start-up transient, reproducing the same conceptual pattern appearing in Figure 14.12 (right), but in this case in a more explicit way. Also, the evolution of other second order eccentricity-related components (designed as EC-100, EC-125, EC-50, EC-175 in Figure 14.17 (right)) can be followed, improving the reliability of the diagnostic of faulty machine.

14.9 Instantaneous Frequency Approach

14.9.1 Basis for the Application of the IF Approach to Diagnostic of Electrical Machines

As it was explained in the previous section, the diagnostic based on conventional MCSA relies on the fact that different kind of fault produces specific families of harmonics to appear (or greatly increase their amplitude) in the currents circulating in the windings of the machine.

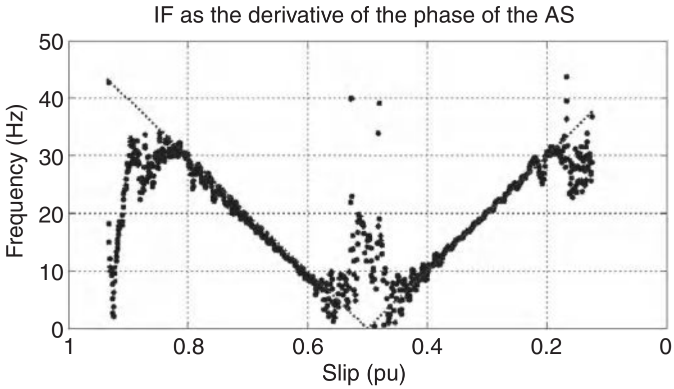

Figure 14.19 Experimental IF of the LSH extracted from the start-up stator current of a gage motor with one broken bar, computed using Hilbert transform

References

Aiello M, Cataliotti A, and Nuccio S (2005) An induction motor speed measurement method based on current harmonic analysis with the Chirp-Z transform. *IEEE Transactions on Instrumentation and Measurement*, **54** (5), 1811–1819.

Antonino-Daviu J, Riera-Guasp M, Folch J, and Palomares MP (2006) Validation of a new method for the diagnosis of rotor bar failures via wavelet transform in industrial induction machines. *IEEE Transactions on Industry Applications*, **42** (4), 990–996.

Antonino-Daviu J, Rodriguez P, Riera-Guasp M, *et al*. (2009) Transient detection of eccentricity-related components in induction motors through the hilbert-huang transform. *Energy Conversion and Management*, **50** (7), 1810–1820.

Bellini A, Filippetti F, Franceschini G, *et al*. (2001) Quantitative evaluation of induction motor broken bars by means of electrical signature analysis. *IEEE Transactions on Industry Applications*, **37** (5), 1248–1255.

Bellini A, Franceschini G, and Tassoni C (2006) Monitoring of induction machines by maximum covariance method for frequency tracking. *IEEE Transactions on Industry Applications*, **42** (1), 69–78.

Blödt M, Granjon P, Raison B, and Regnier J (2010) Mechanical fault detection in induction motor drives through stator current monitoring - theory and application examples, in *Fault Detection* (ed. W Zhang), InTech, pp. 451–487.

Burrus C, Gopinath R, and Guo H (1998) Introduction to wavelets and wavelet transforms: a primer. *Recherche*, **67**, 02.

Cabanas M and Melero M (1998) *Técnicas para el mantenimiento y diagnóstico de máquinas eléctricas rotativas*. Marcombo.

Cizek V (1970) Discrete Hilbert transform. *IEEE Transactions on Audio and Electroacoustics*, **18** (4), 340–343.

Climente-Alarcon V, Antonino-Daviu J, Riera-Guasp M, *et al.* (2011) Transient tracking of low and high-order eccentricity-related components in induction motors via TFD tools. *Mechanical Systems and Signal Processing*, **25** (2), 667–679.

Cohen L (1989) Time-frequency distributions-a review. *Proceedings of the IEEE*, **77** (7), 941–981.

Didier G, Ternisien E, Caspary O, and Razik H (2006) Fault detection of broken rotor bars in induction motor using a global fault index. *IEEE Transactions on Industry Applications*, **42** (1), 79–88.

Douglas H, Pillay P, and Ziarani AK (2005) Broken rotor bar detection in induction machines with transient operating speeds. *IEEE Transactions on Energy Conversion*, **20** (1), 135–141.

Durocher D and Feldmeier G (2004) Predictive versus preventive maintenance. *Industry Applications Magazine, IEEE*, **10** (5), 12–21.

Edwards C, Spurgeon S, and Patton R (2000) Sliding mode observers for fault detection and isolation. *Automatica*, **36** (4), 541–553.

15

Sensorless Speed Control of PMSM

Dhruv Shah[1], Gerardo Espinosa–Pérez[2], Romeo Ortega[1],
and Michaël Hilairet[3]
[1]*LSS, SUPELEC, CNRS, France*
[2]*Facultad de Ingeniería, UNAM, México*
[3]*LGEP, SUPELEC, CNRS, France*

15.1 Introduction

Sensorless control of electrical machines is a topic that imposes the challenging problem of eliminating the use of sensors for mechanical variables (position and speed) for controller design purposes (Rajashekara *et al.* 1996). Its solution is both important from the applications perspective (due to its economic impact) and quite attractive from the control theory approach (for the mathematical complexity that it exhibits). In spite of the maturity level achieved for understanding the usual strategies implemented in industrial applications as well as in the proposition of novel control schemes (Dawson *et al.* 1998; Ortega *et al.* 1998; Khorrami *et al.* 2003; Nam 2010), the sensorless control problem is currently recognized as a longstanding essentially open problem.

In this paper we are interested in the sensorless control for nonsalient permanent-magnet synchronous motors (PMSM). For solving it, three variables must be estimated out of the measurement of the electrical coordinates: (1) rotor position, (2) rotor speed, and (3) load torque—the latter assumed constant. Heuristically conceived solutions for this problem abound in the literature (see, e.g., Ichikawa *et al.* (2006) and Fabio *et al.* (2010) for recent surveys). Many results are also available for the (practically unrealistic) cases of known initial position (Tomei and Verrelli 2008; Ezzat *et al.* 2010b) or zero-load torque (Ezzat *et al.* 2010a), or the (theoretically unjustifiable) assumption of bounded trajectories (Ezzat *et al.* 2010b). An approximate stability analysis of the scheme proposed in Matsui (1996) is carried out in Nahid *et al.* (2001). In Marino *et al.* (2008) a probably stable sensorless scheme for wound-rotor

---

AC Electric Motors Control: Advanced Design Techniques and Applications, First Edition. Edited by Fouad Giri.

Remark 15.2.1 *The main advantage of the dq model is that it transforms the periodic orbits associated to the constant speed operation of the $\alpha\beta$ model of the PMSM into equilibrium points. See Section 15.5.2.*

Remark 15.2.2 *The industry standard field oriented control (Nam 2010) is designed for this model, hence the need to reconstruct θ. Indeed, it must be recalled that the input is $v_{\alpha\beta}$, while the measurable output is $i_{\alpha\beta}$, but θ is an* unmeasurable *variable.*

15.2.1 Problem Formulation

The main contribution of the paper is the solution of the following *Sensorless control problem. Consider the PMSM model* (15.2), (15.3), and (15.4) *with some desired constant speed* $\omega^* \neq 0$, *under the following conditions:*

A1 *The only variables available for measurement are $i_{\alpha\beta}$.*

A2 *The load torque τ_L is constant but* unknown.

A3 *The parameters R, L, Φ and J are known.*

Design an output-feedback controller that ensures the existence of a set of initial conditions, which guarantees that all signals are bounded and that $\omega(t)$ converges, exponentially fast, to ω^*.

Remark 15.2.3 *Even though we have restricted ourselves to the case of constant desired speed and constant load torque, it is clear that the controller, being exponentially stable hence robust, will be able to track (slowly) time-varying references and reject changes in the load torque. Interestingly, the simulations and experimental results of Section 15.9 show that the proposed controller yields a good performance even in the face of fast changes in the speed reference and the load torque. The constraint $\omega^* \neq 0$ is necessary in the present (sensorless) context, because it is easy to show (see, e.g., Zaltni et al. 2008; Ezzat et al. 2010a; Ortega et al. 2011), that the rank condition for observability is violated when the motor is at standstill. Practically, this assumption is not restrictive because, once again, the intrinsic robustness of the controller accommodates sign changes in the desired speed.*

15.3 Controller Structure and Main Result

To simplify the presentation of the main result it is convenient to explain the controller structure and define the notation. The proposed controller is a fourth order certainty equivalent version of a full-information globally asymptotically stabilizing controller, which is a static state-feedback IDA-PBC of the form $v_{\alpha\beta} = q(\rho_{\alpha\beta}, \omega, \tau_L, i_{\alpha\beta})$.

The certainty equivalent version is obtained by replacing $\rho_{\alpha\beta}$, ω, and τ_L by their estimates. The dynamics of the controller is, then, due to the I&I observer, which generates the estimates that we denote $\hat{\rho}_{\alpha\beta}$, $\hat{\omega}$, and $\hat{\tau}_L$, respectively. The controller, combined with the third order PMSM dynamics (15.7) yields a seventh order closed loop system.

15.4 Unavailability of a Linearization-Based Design

Before proceeding with the design of a controller for the nonlinear model it is natural to explore the possibility of basing the design on the PMSMs linearization. This question is particularly relevant in our case since, as explained below, the stability analysis of the proposed controller relies on the linearization of the closed loop.

To answer this question, it is convenient to work with the *dq* model (15.7), with measurable output signals the currents $i_{\alpha\beta}$. Fixing a constant desired speed ω^*, and its corresponding constant equilibrium current i^*, define the error signals

$$\delta_x(t) = \begin{bmatrix} i(t) - i^* \\ \omega(t) - \omega^* \\ \theta(t) - \theta^*(t) \end{bmatrix}, \qquad \delta_v := v - v^*,$$

where $\theta^*(t) = \theta(0) + \omega^* t$, and v^* is the constant control signal that assigns the equilibrium (i^*, ω^*). Now, as the measurable signal is $i_{\alpha\beta}$, invoking (15.8) we define the "output" error

$$\delta_y(t) := e^{\mathcal{J}\theta(t)} i(t) - e^{\mathcal{J}\theta^*(t)} i^*.$$

The linearization of (15.7) and the output map above, along the equilibrium trajectory, yields the linear time-varying system

$$\begin{aligned} \dot{\delta}_x &= A_\ell \delta_x + B\delta_v, \\ \delta_y &= C(t)\delta_x, \end{aligned}$$

where

$$A_\ell := \begin{bmatrix} -\left(\frac{R}{L} I_2 + n_p\omega^*\mathcal{J}\right) & -n_p\mathcal{J}\left(\frac{\Phi}{L} e_1 + i^*\right) & 0 \\ \frac{n_p}{J}\Phi e_1^\top \mathcal{J}^\top & 0 & 0 \\ 0 & n_p & 0 \end{bmatrix}, \quad B := \begin{bmatrix} \frac{1}{L} I_2 \\ 0 \\ 0 \end{bmatrix},$$

$$C(t) := \left[\, e^{\mathcal{J}\theta^*(t)} \quad 0 \quad e^{\mathcal{J}\theta^*(t)} \mathcal{J} i^* \,\right].$$

Although, apparently, this is an innocuous linear time-varying system for which an observer-based controller could be designed, there are several aspects that stymies this task. First of all, the *equilibrium is unknown* because, on one hand, i^* depends on the unknown load torque τ_L. On the other hand, the position $\theta^*(t)$ is also unknown, due to its dependence on $\theta(0)$—see the remark below. Consequently, the system coefficients are unknown. On top of that, the "output" δ_y is known up to the bias term $e^{\mathcal{J}\theta^*(t)} i^*$. In summary, since there exist products of unknown parameters and the unmeasurable state ω, designing an output-feedback controller implies that the solution of a nonlinearly parameterized adaptive observer problem—to the best of our knowledge—is not possible with existing techniques.

with arbitrary x_1^* and x_3^*. Consistent with engineering practice, and without loss of generality, we will fix $x_1^* = 0$ in the sequel. See the remark below.

The objective of IDA-PBC is to find a state-feedback control law $v = v(x)$ that assigns to the closed loop a desired energy function, say $H_d(x)$, which satisfies $x^* = \arg\min H_d(x)$. This is achieved by modifying the interconnection and damping matrices, endowing the closed loop with the port-Hamiltonian form

$$\dot{x} = F_d(x)\nabla H_d(x), \tag{15.14}$$

where $F_d(x) + F_d^\top(x) \leq 0$. This ensures stability of the equilibrium x^* with Lyapunov function $H_d(x)$. Under some standard detectability assumptions (e.g., Lemma 3.8, van der Schaft 2000), the equilibrium is shown to be asymptotically stable.

15.5.2 A Full-Information IDA-PBC

Proposition 15.5.1 *Consider the PMSM dq model (15.13) with a desired equilibrium point*

$$x^* = \begin{bmatrix} 0 \\ \frac{L}{n_p\Phi}\tau_L \\ J\omega^* \end{bmatrix}. \tag{15.15}$$

The full-information control

$$v^{FI} = dx_{12} + \begin{bmatrix} -\frac{L}{J\Phi}\tau_L x_3 \\ n_p\Phi\omega^* + \frac{r}{n_p\Phi}\tau_L \end{bmatrix}, \tag{15.16}$$

where $d := \frac{R-r}{L}$, with $r > 0$ a damping injection term, renders x^* globally asymptotically stable.

Proof: Define the desired closed-loop energy function as the quadratic in the errors form

$$H_d(\chi_{13}) = \frac{1}{2}\chi_{13}^\top Q \chi_{13},$$

with

$$\chi_{13} = \begin{bmatrix} \chi_{12} \\ \chi_3 \end{bmatrix} = \begin{bmatrix} x_{12} - x_{12}^* \\ x_3 - x_3^* \end{bmatrix},$$

where Q is as in (15.12).

In order to achieve the required matching between the right-hand sides of equations (15.13) and (15.14), it is considered that matrix $F_d(x)$ is partitioned in an appropriate way, with

Now, with the definition above,

$$\nabla\zeta = \frac{-1}{|\hat{\rho}_{\alpha\beta}|^2}\begin{bmatrix} a_1 \\ -a_2 \end{bmatrix}\hat{\rho}_{\alpha\beta}^{\top}\mathcal{J}.$$

Consequently, $\nabla\zeta\,\hat{\rho}_{\alpha\beta} = 0$, and the second right-hand term in (15.35) vanishes. The proof is completed noting that

$$A_{33}\begin{bmatrix} a_1 \\ -a_2 \end{bmatrix} = \begin{bmatrix} \frac{a_2}{J} - n_p a_1^2 \\ n_p a_1 a_2 \end{bmatrix},$$

replacing the function arctan by the operator $\mathcal{A}$ in equation (15.30), and noting that the derivations above remain valid after this substitution. □

Remark 15.7.2 *If the* arctan *function is used instead of the operator $\mathcal{A}$ in order to recover the estimate $\hat{\rho}_{\alpha\beta}$, some Dirac delta functions might appear in the speed estimation and the error dynamics. To explain this phenomenon consider the case of (constant) regulation of the motor speed and assume that $\hat{\rho}_{\alpha\beta}(t) \equiv \rho_{\alpha\beta}(t)$. Then, in view of (15.38), we have that $\zeta(\hat{\rho}_{\alpha\beta}(t)) \equiv \theta(t) = \omega^* t (\mathtt{mod}\ \pi)$, which is a periodic function defined on the set $(-\pi, \pi)$. In this scenario, the arctan jumps instantaneously from the value $\frac{\pi}{2}$ to the value $\frac{-\pi}{2}$ inducing a train of Dirac delta functions, $\delta_T(t)$, in the derivative of* arctan. *This term propagates, through $\dot{\zeta}(\rho_{\alpha\beta})$, into the error dynamics that now reads as*[6]

$$\dot{\chi}_{67} = \begin{bmatrix} -n_p a_1 & -\frac{1}{J} \\ n_p a_2 & 0 \end{bmatrix}\chi_{67} + \begin{bmatrix} a_1 \\ -a_2 \end{bmatrix}\delta_T.$$

As illustrated in the simulations of Section 15.9 this undesirable effect is removed by using instead the operator $\mathcal{A}$ defined in Appendix A.

Remark 15.7.3 *Proposition 15.7.1 refers to the unperturbed dynamics (15.29), for which it was assumed that $\tilde{\rho}_{\alpha\beta} = 0$. Some simple calculations show that if this term is not zero the error dynamic of χ_{67} takes the form*

$$\dot{\chi}_{67} = \begin{bmatrix} -n_p a_1 & -\frac{1}{J} \\ n_p a_2 & 0 \end{bmatrix}\chi_{67} - \frac{n_p\omega}{|\hat{\rho}_{\alpha\beta}|^2}\begin{bmatrix} a_1 \\ -a_2 \end{bmatrix}\hat{\rho}_{\alpha\beta}^{\top}\tilde{\rho}_{\alpha\beta} + \begin{bmatrix} \frac{n_p\Phi}{J} i_{\alpha\beta}^{\top}\mathcal{J}\tilde{\rho}_{\alpha\beta} \\ 0 \end{bmatrix}. \tag{15.39}$$

In the next section, the effect of the additional terms on the overall dynamics is analyzed.

---

[6] The expression above shows that, away from the isolated points where the δ–functions appear, the observer error exponentially converges to zero.

15.8 Proof of the Main Result

In this section, the stability properties of the closed-loop system, composed by the motor (15.7), the output-feedback controller (15.18), the position observers (15.23) and (15.25), and the speed-load torque observer (15.30) are studied.

The dynamics are described using the error coordinates (15.9), which yields a set of nonlinear differential equations of the form (15.10). For ease of reference, these equations are sequentially derived for χ_{13}, χ_{45}, and χ_{67}. The stability properties of the system are established by invoking Lyapunov's indirect method. Towards this end, the equations are written in the form

$$\dot{\chi} = A\chi + \Gamma(\chi), \tag{15.40}$$

where A is the system matrix of the linearized system, that is, $A := \nabla f(0)$, where $f(\chi)$ is defined in (15.9) and (15.10), and the elements of the vector $\Gamma(\chi)$ contain (second or higher order) products of the components of χ. The proof of the claim of asymptotic stability of Proposition 15.3.1, follows showing that A is a Hurwitz matrix.

15.8.1 Currents and Speed Tracking Errors

Lemma 15.8.1 *Consider the PMSM model (15.7) in closed loop with the output-feedback controller (15.18). The first three components, χ_{13}, of the error vector χ—defined in (15.9)—evolve according to the following dynamics:*

$$\dot{\chi}_{13} = A_{11}\chi_{13} + A_{12}\chi_{45} + A_{13}\chi_{67} + \Gamma_{13}(\chi), \tag{15.41}$$

where

$$\begin{aligned}
A_{11} &= F_d(x^*)Q,\\
A_{12} &= \begin{bmatrix} -\frac{L}{J\Phi}\tau_L x_3^* & -dx_2^* - \frac{n_p\Phi}{J}x_3^* - \frac{r}{n_p\Phi}\tau_L \\ dx_2^* + \frac{n_p\Phi}{J}x_3^* + \frac{r}{n_p\Phi}\tau_L & -\frac{L}{J\Phi}\tau_L x_3^* \\ 0 & 0 \end{bmatrix},\\
A_{13} &= \begin{bmatrix} -\frac{L}{\Phi}\tau_L & -\frac{L}{J\Phi}x_3^* \\ 0 & \dfrac{r}{n_p\Phi} \\ 0 & 0 \end{bmatrix},
\end{aligned} \tag{15.42}$$

where $d = \frac{R-r}{L}$, while $F_d(x)$ and Q are defined in equations (15.17) and (15.12), respectively, and $\Gamma_{13}(\chi)$ is such that $\nabla\Gamma_{13}(0) = 0$. Moreover, the matrix A_{11} is Hurwitz.

Proof: The output-feedback controller (15.18) can be written as

$$v_{\alpha\beta} = \left[\tilde{\rho}_\alpha I_2 + \tilde{\rho}_\beta \mathcal{J}\right]\hat{v} + e^{\mathcal{J}\theta}\hat{v},$$

which, in dq coordinates, that is, considering $v = e^{-\mathcal{J}\theta}v_{\alpha\beta}$, takes the form

$$v = \hat{v} + [\hat{v}_1 I_2 + \hat{v}_2 \mathcal{J}]\,\chi_{45}, \tag{15.43}$$

where we have used the errors $\chi_{45} = e^{-\mathcal{J}\theta}\tilde{\rho}_{\alpha\beta}$, and $\hat{v}_1$ and $\hat{v}_2$ are the components of $\hat{v}$.

On the other hand, some simple calculations show that

$$\hat{v} = v^{FI} + \begin{bmatrix} -\frac{L}{\Phi}\tau_L & -\frac{L}{J\Phi}x_3^* \\ 0 & \frac{r}{n_p\Phi} \end{bmatrix}\chi_{67} - \begin{bmatrix} \frac{L\chi_7}{\Phi}\left(\frac{1}{J}\chi_3 + \chi_6\right) \\ 0 \end{bmatrix},$$

with the full-information control v^{FI} given by (15.16). Using the definition of χ_3, the latter can be decomposed as

$$v^{FI} = dx_{12} + \begin{bmatrix} -\frac{L}{J\Phi}\tau_L x_3^* \\ -\frac{n_p\Phi}{J}x_3^* - \frac{r}{n_p\Phi}\tau_L \end{bmatrix} + \begin{bmatrix} \frac{L}{J\Phi}\tau_L\chi_3 \\ 0 \end{bmatrix}.$$

Finally, the second term of the control law v can be expanded as

$$[\hat{v}_1 I_2 + \hat{v}_2\mathcal{J}]\,\chi_{45} = \begin{bmatrix} -\frac{L}{J\Phi}\tau_L x_3^* & -dx_2^* - \frac{n_p\Phi}{J}x_3^* - \frac{r}{n_p\Phi}\tau_L \\ dx_2^* + \frac{n_p\Phi}{J}x_3^* + \frac{r}{n_p\Phi}\tau_L & -\frac{L}{J\Phi}\tau_L x_3^* \end{bmatrix}\chi_{45} + \Gamma_{13}(\chi),$$

for some $\Gamma_{13}(\chi)$ verifying the conditions of the lemma. Using all the expressions above to define v, and replacing in equation (15.13), yields (15.41) and (15.42), allowing to complete the first part of the proof.

To prove that the matrix A_{11} is Hurwitz we use equations (15.17) and (15.12) to evaluate

$$F_d(x^*)Q = \begin{bmatrix} -\frac{r}{L} & \frac{n_p}{J}x_3^* & 0 \\ -\frac{n_p}{J}x_3^* & -\frac{r}{L} & -\frac{n_p\Phi}{J} \\ 0 & \frac{n_p\Phi}{L} & 0 \end{bmatrix}.$$

Some simple calculations show that the characteristic polynomial is of the form $s^3 + c_1 s^2 + c_2 s + c_3$, with the coefficients $c_i > 0$ and verifying $c_1 c_2 > c_3$ that, a simple Routh–Hurwitz test proves is the necessary and sufficient condition for stability. □

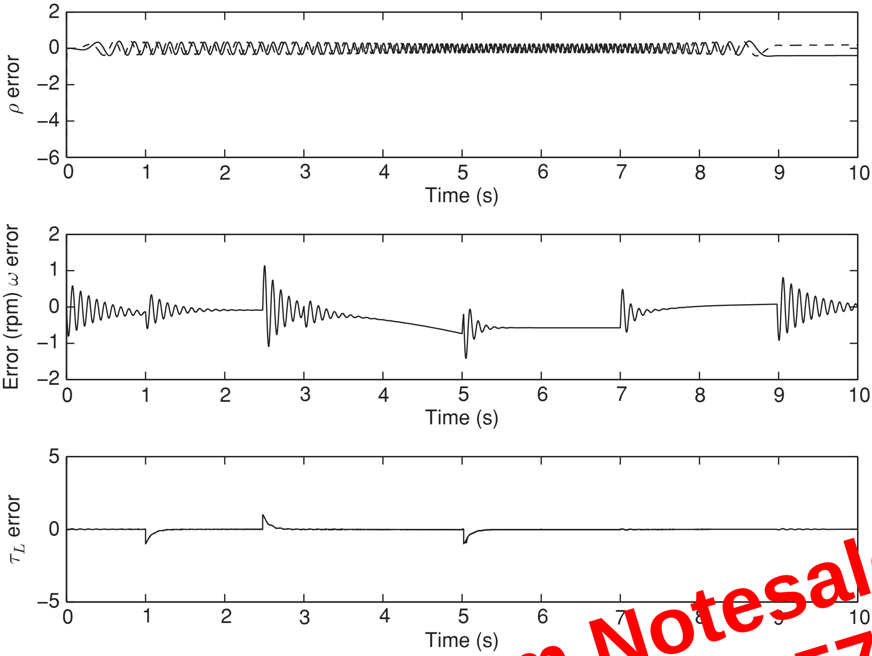

Figure 15.6 Observer and speed tracking errors with a 15% positive increase of the field flux

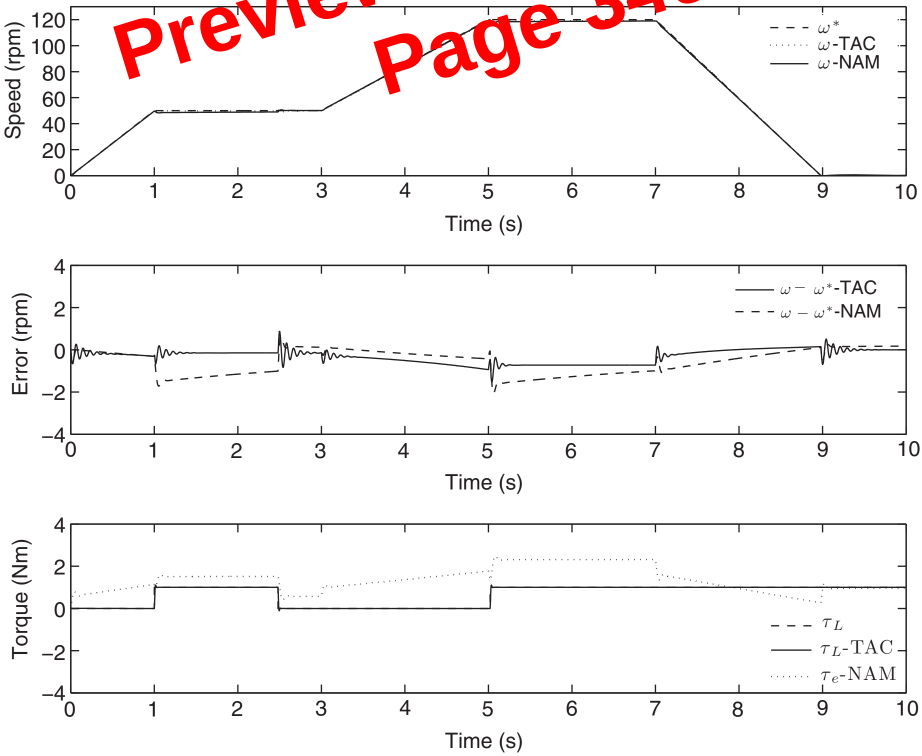

Figure 15.7 Comparative behavior of the proposed scheme (denoted TAC) with the one reported in Nam (2010) (denoted NAM)

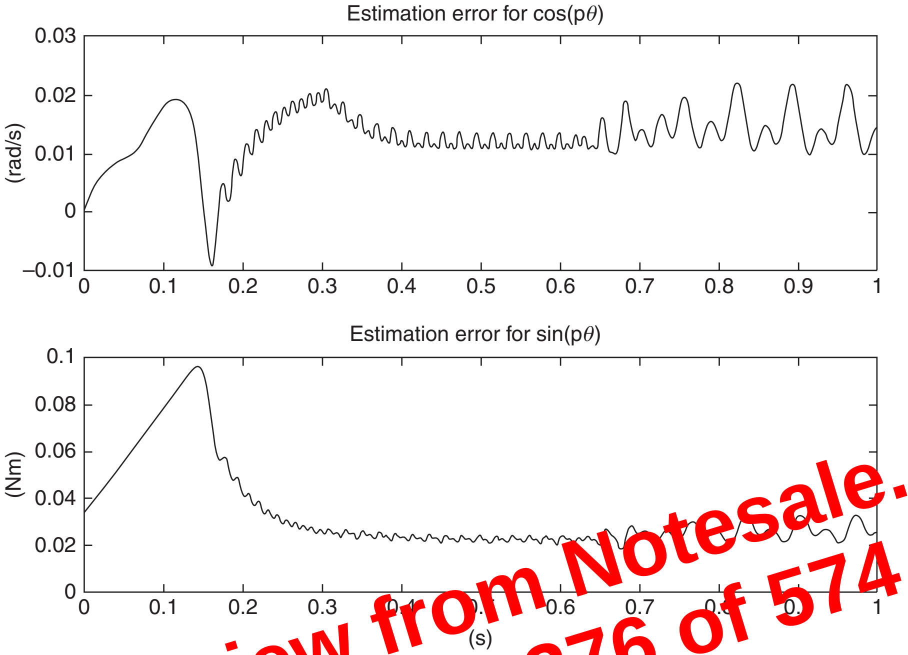

Figure 16.10 Estimation errors: $\cos(p\theta_r(t)) - \widehat{\cos(p\theta_r)}(t)$; $\sin(p\theta_r(t)) - \widehat{\sin(p\theta_r)}(t)$

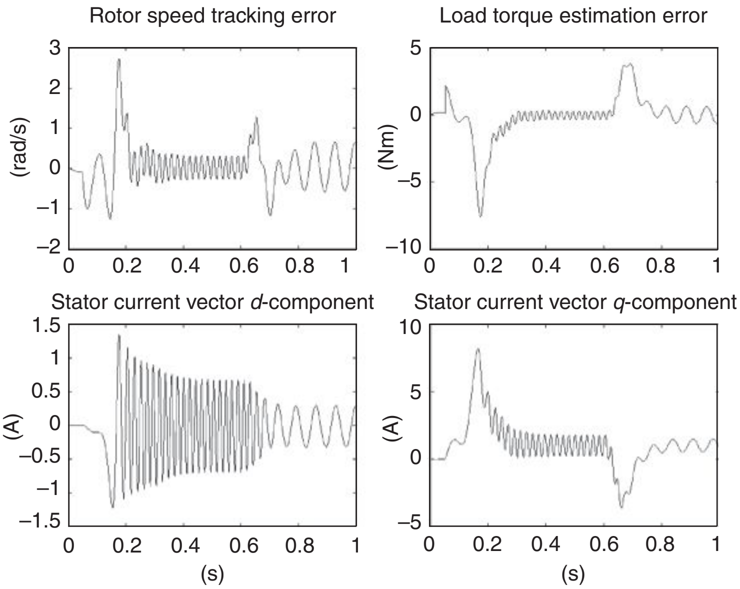

Figure 16.11 Rotor speed tracking error; load torque estimation error; stator current vector (d, q)-components

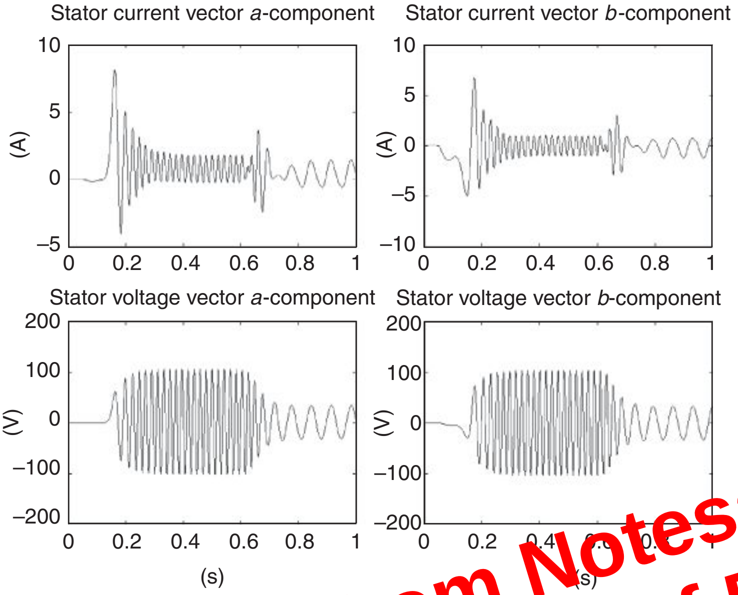

Figure 16.12 (a, b)-components of stator current and voltage vector

16.7 Experimental Setup and Results (Bifaretti *et al.* 2012)

A Tetra 56SR1.35 three-phase PMSM, manufactured by Motor Power Company, has been used in the experiments. Its main specifications are: stall torque of 1.35 Nm, rated phase-to-phase voltage of 95 V AC, maximum phase current of 11.9 A_{rms}. A current-controlled DC motor (RS 263-6005 with rated voltage 24 V DC and motor torque constant of 9 N cm A^{-1}) provides the load torque to the PMSM. The PMSM is fed by a three-phase bridge using 70 V DC bus, while the DC motor is fed by a H-bridge using 25 V DC. The DC bus voltage is generated by single-phase grid voltage whose amplitude is, at first, reduced by a variac and then rectified. The experimental tests have been performed applying a 16 kHz switching frequency for the power MOSFET (IXYS FMM50-025TF) used for both the three-phase and the H-bridges. A Texas Instruments controller board, based on DSP TMS320F28335, is employed to implement the proposed control algorithm and to generate the logic driving signals for the power switches (see Figures 16.13 and 16.14). The sensorless control algorithms (16.3) and (16.4) are executed with a sampling interval $T_s = 62.5$ μs imposed by a suitable interrupt service. At the beginning of each sampling interval, the phase currents values, provided by two Hall effect current sensors, are acquired. The experimental prototype is shown in Figure 16.14 in which the main mechanical and electronic subsystems are highlighted by dashed boxes. A 2000 pulse per revolution encoder, interfaced to a dedicated hardware unit on the DSP that counts the rising and falling edges of the two quadrature encoder signals, provides, in conjunction with the discrete-time Kalman filter proposed in Bellini *et al.* (2003) (with a 20 Hz cut-off frequency), the rotor speed measurements required to evaluate the rotor speed tracking performance. All the initial conditions of the motor (16.1) are zero (the motor is aligned and at rest); a zero

References

Awadallah M and Morcos M (2003) Application of AI tools in fault diagnosis of electrical machines and drives-an overview. *IEEE Transactions on Energy Conversion*, **18**(2), 245–251.

Awadallah M, Morcos M, Gopalakrishnan S, and Nehl T (2005) A neuro-fuzzy approach to automatic diagnosis and location of stator inter-turn faults in CSI-fed PM brushless DC motors. *IEEE Transactions on Energy Conversion*, **20**(2), 253–259.

Cusido J, Romeral L, Ortega J, *et al.* (2008) Fault detection in induction machines using power spectral density in wavelet decomposition. *IEEE Transactions on Industrial Electronics*, **55**(2), 633–643.

Huangfu Y, Liu W, and Ma R (2008) Permanent magnet synchronous motor fault detection and isolation using second order sliding mode observer. *3rd IEEE Conference on Industrial Electronics and Applications*, pp. 639–644.

Kim KH, Choi DU, Gu BG, and Jung IS (2010) Fault model and performance evaluation of an inverter fed permanent magnet synchronous motor under winding shorted turn and inverter switch open. *IET Electric Power Applications*, **4**(4), 214–225.

Liu L and Carter DA (2005) On-line identification and robust fault diagnosis for nonlinear pmsm drives. *2005 American Control Conference*, pp. 2023–2027.

Patton RJ, Frank PM, and Clark RN (ed.) (2000) *Issues of Fault Diagnosis for Dynamic Systems*. Springer-Verlag, New York.

Quiroga J, Liu L, and Carter DA (2008) Fuzzy logic based fault detection of PMSM stator winding short and long fluctuations using negative sequence analysis. *2008 American Control Conference*, pp. 4262–4267.

Rosero J, Cusido J, Garcia A, *et al.* (2006) Broken bearings and eccentricity fault detection for a permanent magnet synchronous motor. *32nd Annual Conference on IEEE Industrial Electronics, IECON 2006*, pp. 964–969.

18

On Digitization of Variable Structure Control for Permanent Magnet Synchronous Motors

Yong Feng[1,2], Xinghuo Yu[2], and Fengling Han[3]
[1] Department of Electrical Engineering, Harbin Institute of Technology, China
[2] School of Electrical and Computer Engineering, RMIT University, Australia
[3] School of Computer Science and Information Technology, RMIT University, Australia

18.1 Introduction

AC Motors have been widely used in various applications, such as factory automation, household electrical appliances, computers, CNC (Computer Numerical Control) machine tools, industrial robots, high-speed aerospace drives and high-technology tools used for outer space in the past decades (Jang *et al.* 2003; Zhang *et al.* 2006; Feng *et al.* 2011). There are two main types of AC motors depending on the principle of operation, the induction motor (IM) and the permanent magnet synchronous motor (PMSM). The rotor of IM includes a winding, while the rotor of a PMSM is a permanent magnet and has no winding. The rotor of PMSMs turns at the same speed as the rotating synchronous magnetic field of the stator which is generated by the stator currents. Unlike PMSMs, an IM always turns slightly slower than the rotating stator magnetic field generated by the stator currents. The difference is called the slip, which generates the torque of the motor (Trzynadlowski 2001).

IMs are generally used for fans, pumps, compressors, elevators, hydraulics, machinery, and actuation systems as well as industrial, aerospace, and medical applications because of their simple design, no brushes, rugged construction, load-bearing capacity, flexibility, relatively low cost, and characteristically long operating life.

AC Electric Motors Control: Advanced Design Techniques and Applications, First Edition. Edited by Fouad Giri.

This trajectory should be followed when operation is below the base speed. i_{dA} and i_{qA} are the current limits that must be placed on the d- and q-axes current controllers when operation is along this trajectory during transient operation.

19.3.2 *The Field-Weakening (Constant-Power) Trajectory*

When operation is above the base speed ω_b, field weakening has to be employed so that the stator voltage is kept within the rated limit given by equation (19.11). In Figure 19.9, the voltage limit trajectory for the base speed of 1500 rpm is indicated. As the speed increases, the i_d and i_q current limits must follow the values given by equation (19.14), along the intersections of current and voltage limit trajectories for each speed. The d- and q-axes currents are controlled in order to satisfy the machine voltage limit V_{om} given by

$$v_o = \sqrt{v_{do}^2 + v_{qo}^2} \leq V_{om}, \qquad (19.16)$$

where, $v_{do} = -\omega L_q i_q$, $v_{qo} = \omega\lambda_f + \omega L_d i_d$, and $V_{om} = V_{sm} - RI_{sm}$. The relationship between the i_d and i_q in the field weakening range is given from equation (19.12) with V_{sm} replaced by V_{om} in order to include the effect of stator resistance drop. Thus,

$$i_d = -\frac{\lambda_f}{L_d} + \frac{1}{L_d}\sqrt{\frac{v_{om}^2}{\omega^2} - (L_q\, i_q)^2}. \qquad (19.17)$$

By controlling the current vector according to equation (19.17), the terminal voltage is always kept within V_{sm} in the steady state. The intersection between the current limit and voltage limit trajectories at each speed provides the respective current limits for producing maximum torque at each operating speed. These limit values are given by

$$i_{dv} = -\frac{\lambda_f L_d}{a} + \frac{1}{a}\sqrt{\lambda_f^2 L_d^2 - ab}, \qquad (19.18)$$

$$i_{qv} = \sqrt{I_{sm}^2 - i_{dv}^2}, \qquad (19.19)$$

where $a = L_d^2 - L_q^2$, $b = I_{sm}^2 L_q^2 + \lambda_f^2 - \frac{V_{sm}^2}{\omega^2}$.

The voltage limit trajectory is also indicated in Figure 19.9 for the crossover speed (ω_c) of 2400 rpm when the load is zero (or $i_d = i_q = 0$). When the machine is operated between the base and crossover speeds, the operating mode is determined by the load. For example, when the motor runs at 2200 rpm, the corresponding voltage limit trajectory is BCO in Figure 19.9.

If the machine is heavily loaded, the $i_d - i_q$ trajectory is along BC. When lightly loaded, the trajectory is along CO which is on the MPTA trajectory.

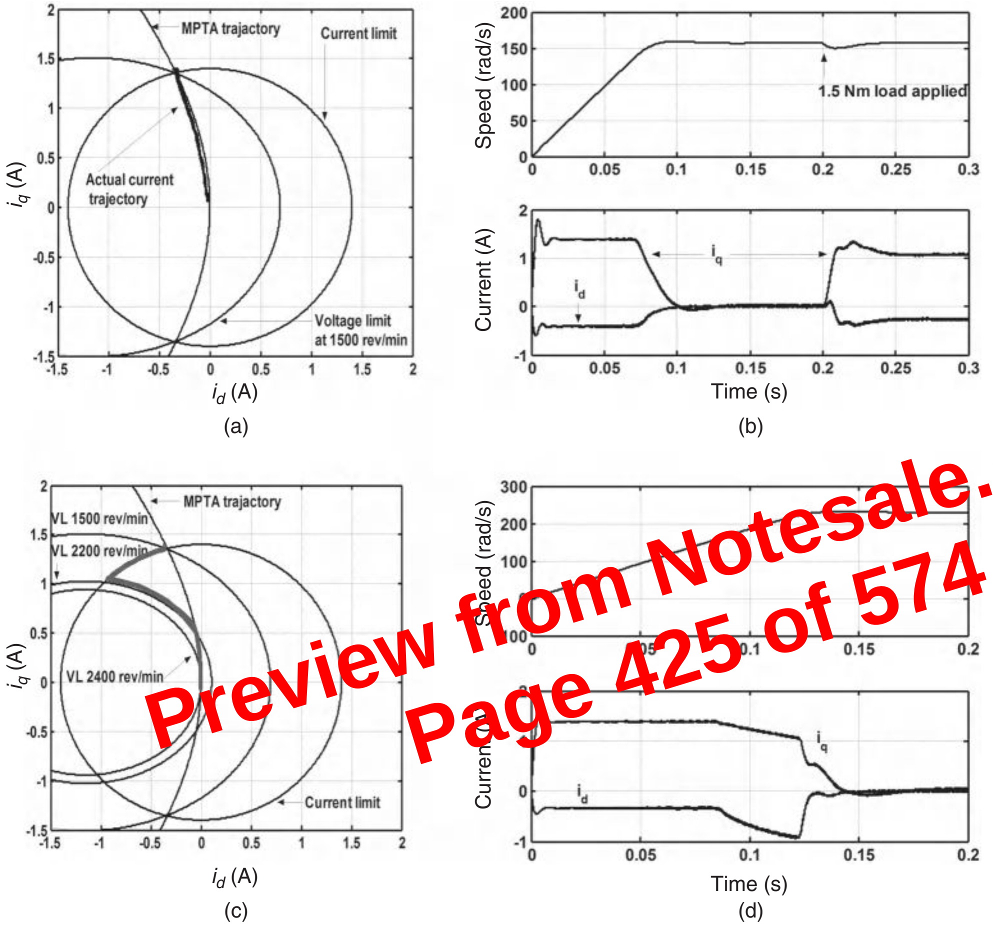

(a) (b) (c) (d)

Figure 19.13 Trajectory following of a current vector controlled IPMSM drive. (a) i_d, i_q currents along the MTPA, (b) i_d, i_q currents during acceleration and on load application, (c) MTPA and FW trajectory following, (d) i_d, i_q during MTPA and FW following (experimental results)

cases of optimum trajectory followings when an IPMSM is operated with MTPA below (base speed), and with flux–weakening at higher speeds. Precise trajectory following with smooth transition between the two trajectories, using the controls indicated in Figures 19.10, 19.11, and 19.12), is clearly demonstrated.

19.4 Sensorless Direct Torque Control of IPM Synchronous Machines

The above-mentioned control techniques are based on i_d and i_q current vector controls in the rotor dq-reference frame. The demanded torque reference from the outer speed control loop primarily defines the i_q current reference. The d-axis current is also controlled simultaneously limit trajectories are to the right of the MTPA *OA* in Figure 19.20a. Therefore, there is no requirement here to control the amplitude of the stator flux linkage λ_s to satisfy the voltage limit.

When the rotor speed increases, the voltage limit trajectories move to the left of the intersection point *A* and the stator flux will have to be reduced in order to satisfy the voltage limit requirement. For operation below the base speed, the MTPA should be selected. For the operation above the crossover speed, field-weakening control is selected since the voltage limit will no longer be satisfied if the torque and λ_s are controlled along the MTPA trajectory. However, for the operation between the base and crossover speeds, the control mode is determined by load torque. With the MTPA control, for instance, if the vertical dashed line in Figure 19.20a represents the voltage limit corresponding to the operation with the rotor speed between ω_b and ω_c, there is an intersection of this line and the maximum torque-per-ampere trajectory, and at this point the torque is T_B. If the actual torque is greater than T_B, field-weakening control is selected. Otherwise, if the actual torque is smaller than T_B, MTPA is selected even though the rotor speed is above the base speed.

19.4.3 Implementation of Trajectory Control for DTC

The block diagram of the outer speed loop for implementation of the trajectory control in DTC is show in Figure 19.21a. A lookup table is used to determine the amplitude of the stator flux linkage according to the MTPA trajectory for constant torque control. For field-weakening operation, the amplitude of the stator flux linkage is simply determined by the inverse of the speed. The control flow-chart for the control mode selection is shown in Figure 19.21b.

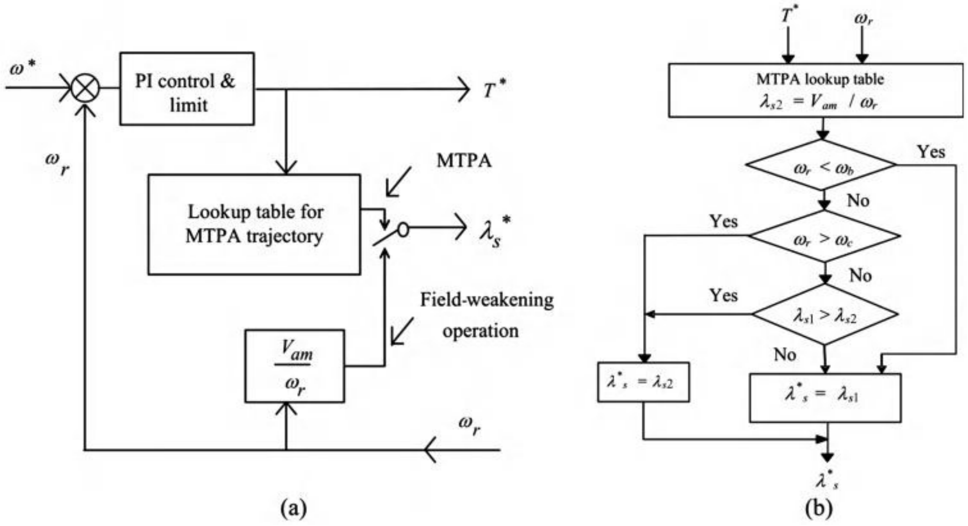

Figure 19.21 (a) Block diagram of the speed loop for trajectory control in DTC; (b) flow chart for the control mode selection

of any sensorless scheme, are then illustrated and their problems and applicability at very low speed are highlighted. The high-frequency signal injection scheme which estimates the stator flux with adequate accuracy by exploiting the saliency of such machines for operation at very low and zero speed is then described. In conclusion, it can be stated that the IPM machine drive technology now offers very attractive solutions for industrial drives covering speed from zero to a wide constant-power speed range.

References

Bianchi N and Bolognani S (1999) Performance analysis of An IPM Motor with segmented rotor for flux-weakening application. *International Conference on Electrical Machine and Drives*, 49–53.

Boldea I, Pitic CI, Lascu C, *et al.* (2006) DTFC-SVM motion sensorless control of a PM-assisted reluctance synchronous machine as starter-alternator for hybrid vehicles. *IEEE Transactions on Power Electronics*, **21**(3), 711–719.

Boldea I, Paicu MC, and Andreescu GD (2008) Active flux concept for motion sensorless unified AC drives. *IEEE Transactions on Power Electronics*, **23**, 2612–2618.

Bolognani S, Oboe R, and Zigliotto M (1999) Sensorless full-digital PMSM drive with EKF estimation of speed and rotor position. *IEEE Transactions on Industrial Electronics*, **46**, 184–191.

Caruana C, Asher GM, Bradley KJ, and Woolfson MS (2003) Flux position estimation in cage induction machines using synchronous injection and kalman filtering. *IEEE Transactions on Industry Applications*, **39**(5), 1372–1378.

Chen Z, Tomita M, Doki S, and Okuma S (2003) An extended electromotive force model for sensorless control of interior permanent-magnet synchronous motors. *IEEE Transactions on Industrial Electronics*, **50**, 288–295.

Corley M and Lorenz RD (1998) Rotor position and velocity estimation for a salient-pole permanent magnet synchronous machine at standstill and high speeds. *IEEE Transactions on Industry Applications*, **43**(4), 784–789.

Dutta R and Rahman MF (2008) Design and analysis of an interior permanent magnet (IPM) machine with very wide constant power operation range. *IEEE Trans on Energy Conversion*, **23**(1), 25–33.

Foo G and Rahman MF (2010) Sensorless sliding mode MTPA control of an IPM synchronous motor drive using a sliding mode observer and HF signal injection. *IEEE Transactions on Industrial Electronics*, **57**(4), 1270–1278.

Foo G, Sayeef S, and Rahman MF (2010) Low speed and standstill operation of a sensorless direct torque and flux controlled IPM synchronous motor drive. *IEEE Transactions on Energy Conversion*, **25**(1), 25–33.

Haque ME and Rahman MF (1994) A Sensorless initial rotor position estimation scheme for a direct torque controlled interior permanent magnet synchronous motor drive. *IEEE Transactions on Power Electronics*, **18**(6), 1376–1383.

Haraguchi H, Morimoto S, and Sanada M (2009) Suitable design of a PMSG for a small-scale wind power generator. In *Electrical Machines and Systems ICEMS 2009*, 1–6.

Honda Y, Higaki T, Morimoto S, and Takeda Y (1998) Rotor design optimisation of a multi-layer interior permanent-magnet synchronous motor. *Electric Power Applications, IEE Proceedings*, vol. **145**, 119–124.

Honda Y, Higaki T, Morimoto S, and Takeda Y (1986) Interior permanent-magnet synchronous motors for adjustable-speed drives. *IEEE Transaction on Industry Applications*, **22**, 738–747.

Jahns TM (1987) Flux-weakening regime operation of an interior permanent magnet synchronous motor drive. *IEEE Trans. on Industry Applications*, **23**, 398–407.

Jahns TM, Kaliman GB, and Neumann TW (1986) Interior permanent-magnet synchronous motors for adjustable speed drives. *IEEE Transactions on Industry Applications*, **22**, 738–747.

Jung-Ik Ha and Seung-Ki Sul (1999) Sensorless field-orientation control of an induction machine by high-frequency signal injection. *IEEE Transaction on Industry Applications*, **35**(1).

Kamiya M (2006) Development of traction drive motors for the toyota hybrid system. *Transactions of the Institute of Electrical Engineers of Japan*, **126**, 473–479.

Kim H, Harke MC, and Lorenz RD (2002) Sensorless control of interior permanent magnet drives with zero-phase lag position estimation. *Conference REC IEEE-IAS Annual Meeting*, 86–91.

Kim H, Huh KK, Lorenz RD, and Jahns TM (2004) A novel method for initial rotor position estimation for IPM synchronous motor drives. *IEEE Transactions on Industry Applications*, **40**(5), 1369–1378.

Miller TJE (1989) *Brushless Permanent-Magnet and Reluctance Machines*. University Press, Oxford.

Morimoto S, Takeda Y, Hirasa T, and Taniguchi K (1990) Expansion of operating limits for permanent magnet motor by current vector control considering inverter capacity. *IEEE Transaction on Industry Applications*, **26**, 866–871.

Morimoto S, Sanada M, and Takeda Y (1994) Wide-speed operation of interior permanent magnet synchronous motors with high-performance current regulator. *IEEE Transactions on Industry Applications*, **30**, 920–926.

Piippo A, Hinkkanen M, and Luomi J (2008) Analysis of adaptive observer for sensorless control of interior permanent magnet synchronous motors. *IEEE Transactions on Industrial Electronics*, **55**, 570–576.

Rahman MF, Zhong L, and Lim KW (1998) A Direct torque controlled interior magnet synchronous motor drive incorporating field weakening. *IEEE Transactions on Industry Applications*, **34**(6), 1246–1253.

Satoh H, Akutsu S, Miyamura T, and Shinoki H (2004) Development of traction motor for fuel cell vehicle. In *SAE World Congress*, Detroit, Michigan.

Sayeef S and Rahman MF (2009) Improved flux and torque estimators of a direct torque controlled interior pm machine with compensations of dead-time effects and forward voltage drops. *Journal of Power Electronics (JPE)*, **9**(3), 438–446.

Sebastiangordon T and Slemon GR (1987) Operating limits of inverter-driven permanent magnet motor drives. *IEEE Transactions on Industry Applications*, **IA-23**, 327–333.

Soong WL, Staton DA, and Miller TJE (1995) Design of a new axially-laminated interior permanent magnet motor. *IEEE Transaction on Industry Applications*, **31**, 358–367.

Spiteri, Cilia C, Michallef J, and Apap M (2002) Sensorless vector control of surface mount pmsm using high frequency injection. *Power Electronics Machines and Drives Conference Publication (487) IEE2002*.

Tang L, Zhong L, Rahman MF, and Hu Y (2004) A novel direct torque controlled interior permanent magnet synchronous machine drive with low ripple in flux and torque and fixed switching frequency. *IEEE Transactions on Power Electronics*, **19**(2), 346–354.

Wang A, Jia Y, and Soong WL (2011) Comparison of five topologies for an interior permanent magnet machine for a hybrid electric vehicle. *IEEE Transactions on Magnetics*, **47**(10), 3606–3609.

Xu Z and Rahman MF (2007) An adaptive sliding stator flux observer for a direct torque controlled IPM synchronous motor drive. *IEEE Transactions on Industrial Electronics*, **54**(5), 2398–2406.

Zhong L, Rahman MF, and Hu WY (1997) Analysis of direct torque control in permanent magnet synchronous motor drives. *IEEE Transactions on Power Electronics*, **12**(3), 528–536.

set of differential equations:

$$L_0 \frac{d[i_{gabc}]}{dt} = [e_{gabc}] - v_{dc}[k_{abc}] \tag{20.1a}$$

$$2C \frac{dv_{dc}}{dt} = i_s - i_r \tag{20.1b}$$

$$i_s = [k_{abc}]^T [i_{gabc}], \tag{20.1c}$$

where $[i_{gabc}] = [\, i_{ga} \; i_{gb} \; i_{gc} \,]^T$ is the three-phase input currents in the electric grid, $[e_{gabc}] = [\, e_{ga} \; e_{gb} \; e_{gc} \,]^T$ is the sinusoidal three-phase net voltages (with known constant frequency ω_g), v_{dc} denotes the voltage in capacitor 2C, i_r designates the output current converter and $k_i \;\; (i = a, \; b, \; c)$ is a binary control input determining the switch position. Specifically, one has

$$k_i = \begin{cases} 1 \;\text{ if }\; K_i \;\text{ is }\; \text{ON} \;\text{ and }\; K'_i \;\text{ is }\; \text{OFF} \\ 0 \;\text{ if }\; K_i \;\text{ is }\; \text{OFF} \;\text{ and }\; K'_i \;\text{ is }\; \text{ON} \end{cases} \qquad (i = a, \; b, \; c). \tag{20.2}$$

To simplify the three-phase representation (20.1a) for the synthesis of control laws, the Park transformation is resorted to project the triphase electrical quantities onto the two-coordinate dq-frame. Doing so, one gets the following two-phase model:

$$\frac{di_{gd}}{dt} = \frac{1}{L_0} E_{gd} + \omega_g i_{gq} - \frac{1}{L_0} u_{gd} v_{dc}, \tag{20.3a}$$

$$\frac{di_{gq}}{dt} = \frac{1}{L_0} E_{gq} - \omega_g i_{gd} - \frac{1}{L_0} u_{gq} v_{dc}, \tag{20.3b}$$

$$2C \frac{dv_{dc}}{dt} = i_s - i_r, \tag{20.3c}$$

where (E_{gd}, E_{gq}), (i_{gd}, i_{gq}), and (u_{gd}, u_{gq}) denote, respectively, the network voltage and current and input control of the rectifier in dq-coordinate. Averaging is performed (over the PWM cutting ratio) to get around the difficulty associated to the binary nature of the physical three-phase control input (k_a, k_b, k_c).

The instantaneous power absorbed by the AC/DC converter is given by the well-known expression $P_{\text{Load}} = [e_{gabc}]^T [i_{gabc}] = E_{gd} i_{gd} + E_{gq} i_{gq}$. On the other hand, the power released by the network is given by $P_{\text{Out}} = i_s v_{dc}$. Using the power conservation principle, that is, $P_{\text{Out}} \approx P_{\text{Load}}$, one gets $i_r v_{dc} = E_{gd} i_{gd} + E_{gq} i_{gq}$. Then, multiplying by v_{dc} the first equation of the system (20.3a-c), this rewrites:

$$2v_{dc} \frac{dv_{dc}}{dt} = \frac{1}{C} E_{gd} i_{gd} + \frac{1}{C} \left(E_{gq} i_{gq} - v_{dc} i_r \right), \tag{20.4a}$$

$$\frac{di_{gd}}{dt} = \frac{1}{L_0} E_{gd} + \omega_g i_{gq} - \frac{1}{L_0} u_{gd} v_{dc}, \tag{20.4b}$$

$$\frac{di_{gq}}{dt} = \frac{1}{L_0} E_{gq} - \omega_g i_{gd} - \frac{1}{L_0} u_{gq} v_{dc}. \tag{20.4c}$$

As $\alpha = (a_1 x_3 + a_2 x_4)\, x_2$ is just a virtual control input, one cannot set $\alpha = \hat{\alpha}^*$. Nevertheless, the above expression of $\hat{\alpha}^*$ is retained and a new error is introduced:

$$z_2 = \alpha - \hat{\alpha}^*. \tag{20.14}$$

Using equations (20.13)–(20.14), it follows from (20.9) that the z_1-dynamics undergo the following equation:

$$\dot{z}_1 = -k_1\, z_1 + \frac{z_2}{J} + \frac{\tilde{J}}{J}\, \left(k_1\, z_1 - \dot{x}_1^*\right) - \frac{\tilde{T}_L}{J} - \frac{\tilde{F}}{J}\, x_1, \tag{20.15}$$

where $\tilde{J} = J - \hat{J}$, $\tilde{F} = F - \hat{F}$, and $\tilde{T}_L = T_L - \hat{T}_L$.

Step 2: Now, the aim is to make the couple of errors $(z_1,\, z_2)$ vanish asymptotically. The trajectory of the error z_2 is obtained by time-derivation of the equation (20.14):

$$\dot{z}_2 = (a_1 \dot{x}_3 + a_2 \dot{x}_4)\, x_2 + (a_1 x_3 + a_2 x_4)\, \dot{x}_2 - \dot{\hat{\alpha}}^*. \tag{20.16}$$

Using equations (20.13)–(20.15) and the subsystem (20.7a–b) in (20.16) yields the following z_2-dynamics:

$$\begin{aligned}
\dot{z}_2 = {} & \alpha_1\, u_1 v_{dc} + \alpha_2\, u_2 v_{dc} + \alpha_3\, u_3 v_{dc} \\
& + \beta\,(x_{1\ldots4}) - \hat{J}\, \left(k_1^2\, z_1 + \ddot{x}_1^*\right) + k_1\, z_2 + \hat{F}\left(k_1\, z_1 - \dot{x}_1^*\right) \\
& - \tfrac{\tilde{J}}{J}\, \left(k_1\, z_2 - \hat{J}\, k_1\, \left(k_1\, z_1 - \dot{x}_1^*\right)\right) - \tfrac{\tilde{F}}{J}\, \hat{J}\, k_1\, x_1 - \tfrac{\tilde{T}_L}{J}\, (\hat{J}\, k_1 + \hat{F}) \\
& + \left(k_1\, z_1 - \dot{x}_1^*\right)\, \dot{\hat{J}} - \dot{\hat{T}}_L - \dot{\hat{F}}\, x_1 \\
& - \tfrac{\hat{F}}{J}\, \left(z_2 + \tilde{J}\, \left(k_1\, z_1 - \dot{x}_1^*\right) - \tilde{T}_L - \tilde{F}\, x_1\right) + x_2 x_4\, (a_1 c_2 - a_2 d_1)\, \tilde{R}_f
\end{aligned} \tag{20.17}$$

with

$$\begin{aligned}
\beta\ (x_{i=1\ldots4}) = {} & (a_1\, x_3 + a_2\, x_4)\,(-b_1\, x_2 - b_2\, x_1\, x_3 - b_3\, x_1\, x_4) \\
& + a_1\, x_2\, \left(-c_1\, x_3 + \hat{R}_f c_2\, x_4 + c_3\, x_1 x_2\right) \\
& + a_2\, x_2\, \left(-\hat{R}_f d_1\, x_4 + d_2\, x_3 - d_3\, x_1 x_2\right) \\
\alpha_1 = {} & b_4\, \left(a_1\, x_3 + a_2\, x_4\right) \\
\alpha_2 = {} & x_2\, \left(a_1\, c_4 - a_2\, d_4\right) \\
\alpha_3 = {} & x_2\, \left(-a_1\, c_5 + a_2\, d_5\right),
\end{aligned}$$

where $\tilde{R}_f$ denotes an estimate (yet to be determined) of R_f and $\tilde{R}_f = R_f - \hat{R}_f$. For convenience, the error equations (20.15) and (20.17) are put together:

$$\dot{z}_1 = -k_1\, z_1 + \frac{z_2}{J} + \frac{\tilde{J}}{J}\, \left(k_1\, z_1 - \dot{x}_1^*\right) - \frac{\tilde{T}_L}{J} - \frac{\tilde{F}}{J}\, x_1, \tag{20.18a}$$

$$\begin{aligned}\dot{z}_2 = \gamma &- \tfrac{F}{J}\, z_2 + x_2 x_4\ (a_1 c_2 - a_2\, d_1)\, \tilde{R}_f \\ &-\tfrac{\tilde{J}}{J}\ \left(k_1\, z_2 - (\hat{J}\, k_1 - \hat{F})\left(k_1\, z_1 - \dot{x}_1^*\right)\right) \\ &-\tfrac{\tilde{F}}{J}\ \left((\hat{J}\, k_1 - \hat{F})x_1 + z_2\right) - \tfrac{\tilde{T}_L}{J}\ \left(\hat{J}\, k_1 - \hat{F}\right),\end{aligned} \tag{20.18b}$$

with

$$\begin{aligned}\gamma = \beta\,(x_{1\ldots4}) &+ k_1\, z_2 + \alpha_1\, u_1 v_{dc} + \alpha_2\, u_2 v_{dc} + \alpha_3\, u_3 v_{dc} \\ -\hat{J}\ \left(k_1^2\, z_1 + \ddot{x}_1^*\right) &+ \hat{F}\ \left(k_1\, z_1 - \dot{x}_1^*\right) + \dot{\hat{J}}\left(k_1\, z_1 - \dot{x}_1^*\right) - \dot{\hat{T}}_L - \dot{\hat{F}}\, x_1,\end{aligned} \tag{20.19}$$

Note that the actual control inputs (u_1, u_2, u_3) have come out for the first time in the second differential equation (20.18a), through the quantity γ which acts there as a control variable. To determine a stabilizing control law for (20.18a), let us consider the following quadratic Lyapunov function candidate:

$$V_2 = \frac{1}{2}\, z_1^2 + \frac{1}{2}\, z_2^2 + \frac{1}{2J}\, \tilde{J}^2 + \frac{1}{2J}\, \tilde{F}^2 + \frac{1}{2J}\, \tilde{T}_L^2. \tag{20.20}$$

Using (20.18a), one gets from (20.20):

$$\begin{aligned}\dot{V}_2 &= z_1 \dot{z}_1 + z_2 \dot{z}_2 + \tfrac{\tilde{J}}{J}\, \dot{\tilde{J}} + \tfrac{\tilde{F}}{J}\, \dot{\tilde{F}} + \tfrac{\tilde{T}_L}{J}\, \dot{\tilde{T}}_L \\ &= -k_1\, z_1^2 + \gamma\, z_2 + \tfrac{1}{J} z_1 z_2 - \tfrac{F}{J}\, z_2^2 + (a_1 c_2 - a_2 d_1)\, x_2 x_4 z_2\, \tilde{R}_f \\ &\quad + \tfrac{\tilde{J}}{J}\left(z_1\, (k_1\, z_1 - \dot{x}_1^*) - k_1\, z_1^2 + (\hat{J} k_1 - \hat{F})(k_1\, z_1 - \dot{x}_1^*) z_2 - \dot{\hat{J}}\right) \\ &\quad + \tfrac{\tilde{F}}{J}\left(- x_1 z_1 - z_2^2 - (\hat{J}\, k_1 - \hat{F}) x_1 z_2 - \dot{\hat{F}}\right) \\ &\quad + \tfrac{\tilde{T}_L}{J}\left(- z_1 - (\hat{J}\, k_1 - \hat{F}) z_2 - \dot{\hat{T}}_L\right).\end{aligned} \tag{20.21}$$

The three last terms in the second equality (20.21) can be canceled by using the following adaptive laws:

$$\dot{\hat{J}} = z_1\, \left(k_1\, z_1 - \dot{x}_1^*\right) - k_1\, z_1^2 + (\hat{J} k_1 - \hat{F})\left(k_1\, z_1 - \dot{x}_1^*\right) z_2, \tag{20.22a}$$

$$\dot{\hat{F}} = -x_1 z_1 - z_2^2 - (\hat{J}\, k_1 - \hat{F}) x_1 z_2, \tag{20.22b}$$

$$\dot{\hat{T}}_L = -z_1 - (\hat{J}\, k_1 - \hat{F}) z_2. \tag{20.22c}$$

Substituting (20.22a–c) in (20.21), one gets

$$\dot{V}_2 = -k_1\, z_1^2 + \gamma\, z_2 + \frac{1}{J} z_1 z_2 - \frac{F}{J}\, z_2^2 + (a_1 c_2 - a_2 d_1)\, x_2 x_4 z_2\, \tilde{R}_f. \tag{20.23}$$

This suggests for the control variable γ the following choice:

$$\gamma = -k_2\, z_2, \tag{20.24}$$

This suggests for the (virtual control) ρ the following control law:

$$\rho^* = k_5\, z_5 + \beta_1(x, z) - \dot{x}_5^*. \tag{20.53}$$

with $k_5 > 0$ a design parameter. Indeed, substituting ρ^* to $\rho = \frac{1}{C} E_{gd}\, x_6$ gives $\dot{V}_5 = -k_5\, z_5^2$ which clearly is negative definite in z_5. As ρ is just a virtual control input, one can not set $\rho = \rho^*$. Nevertheless, the above expression of ρ^* is retained and a new error is introduced:

$$z_6 = \rho - \rho^*. \tag{20.54}$$

Using (20.53), it follows from (20.51) that the z_5-dynamics undergoes the following equation:

$$\dot{z}_5 = -k_5\, z_5 + z_6. \tag{20.55}$$

Step 2: Now, the aim is to make the couple of errors (z_5,z_6) vanish asymptotically. The trajectory of the error z_6 is obtained by time-derivation of (20.54), that is,

$$\dot{z}_6 = \frac{E_{gd}}{C}\, \dot{x}_6 + k_5\, \dot{z}_5 + \dot{\beta}_1(x, z) - \ddot{x}_5^*. \tag{20.56}$$

Using equations (20.55) and (20.7e–f) in (20.56) yields

$$\dot{z}_6 = \beta_2(x_i,\ z_i) - \frac{E_{gd}}{CL_0}\, u_4 v_{dc}, \tag{20.57}$$

with

$$\beta_2(x_i,\ z_i) = k_5\, \dot{z}_5 + \dot{\beta}_1(x, z) - \ddot{x}_5^* + \frac{E_{gd}^2}{CL_0} - \frac{E_{gd}}{C}\omega_g x_7. \tag{20.58}$$

To determine a stabilizing control law for (20.7e–f), let us consider the quadratic Lyapunov function candidate $V_6 = \frac{1}{2}\, z_5^2 + \frac{1}{2}\, z_6^2$. Using (20.38)–(20.55), one gets from the expression of V_6 that

$$\dot{V}_6 = -k_5\, z_5^2 + z_6 \left(z_5 + \beta_2(x, z) + \frac{E_{gd}}{CL_0}\, u_4 v_{dc} \right). \tag{20.59}$$

This suggests for the control variable u_4 the following choice:

$$u_4 = -\frac{CL_0}{E_{gd} v_{dc}} \left(k_6\, z_6 + z_5 + \beta_2(x, z)\right), \tag{20.60}$$

where $k_6 > 0$ is a new design parameter. Indeed, substituting (20.60) in (20.59) yields

$$\dot{V}_6 = -k_5\, z_5^2 - k_6\, z_6^2 < 0. \tag{20.61}$$

so that operation along the full CPSR may take place without exceeding the voltage and current limits of the machine. In other words, the machine in a vehicle should be controlled by a torque controller (with appropriate limits) while the speed is lower than the base speed, and by a field controller also with an overriding voltage limiter in addition to maximum torque or current limit as a function of the speed when the operating speed is higher than the base speed. It should be noted here that machines with such wide CPSR have to be carefully designed in order to cover this speed range.

6. In order to have adequate dynamic performance for longitudinal traction, and for pitch and yaw motion controls, the motor drive system needs to employ high-performance controllers. Decoupled field oriented (vector) control incorporating a mechanical position and velocity sensor of high resolution is routinely applied in HEVs and EVs. Sensorless control techniques, such as direct torque control (DTC), are also capable of achieving the required response requirements, with the advantage of not requiring the delicate electromechanical position and speed sensor. It should be noted here that highly dynamic control over the developed torque is also required at very low speed, in fact down to zero speed. For mechanical sensorless drives, this is still a significant challenge.

21.1.2 *The Impact of CPSR on Motor Power Rating and Acceleration Time of a Vehicle*

Under the idealized conditions that the traction motor drives the vehicle via a fixed gear ratio, the friction torque is negligible, and the vehicle reaches a certain speed ω_{rv} in T_F seconds, the following can be written:

$$J \int_0^{\omega_b} \frac{d\omega}{T_m} = T_F, \tag{21.6}$$

where J is the total equivalent rotating moment of inertia, ω_b is the base speed and T_m is the rated maximum torque which the motor develops. From equation (21.6),

$$J \left(\int_0^{\omega_b} \frac{d\omega}{P_R/\omega} + \int_{\omega_b}^{\omega_{rv}} \frac{d\omega}{P_R/\omega} \right) = T_F. \tag{21.7}$$

From equation (21.7), the motor power rating P_R is given by

$$P_R = \frac{J}{2T_F} \left(\omega_b^2 + \omega_{rv}^2 \right). \tag{21.8}$$

Using the expression, $CPSR = \dfrac{\omega_{\max}}{\omega_b}$, equation (21.8) becomes

$$P_R = \frac{J\omega_b^2}{2T_F} \left(1 + \frac{\omega_{\max}}{CPSR^2\ \omega_{rv}^2} \right) = \frac{J\omega_b^2}{2T_F} \left(1 + \frac{\omega_b^2}{\omega_{rv}^2} \right). \tag{21.9}$$

Table 21.1 Traction motor, ICE and battery data of a few recent HEV and EVs

Vehicle	Traction machines used	ECE data	Battery
Honda Insight hybrid, 2010	Brushless PMDC, 9.7 kW, @ 1500 rev/min	1.3 L petrol	100.8 V, 5.75 Ah
Ford Fusion hybrid	PMSM, 79 kW @ 6500 rev/min	2.5 L petrol	275 V, NiMH
Toyota Prius hybrid, 2011	PMSM 1, 30 kW @ 1800 rev/min	1.8 L petrol, 73 kW @ 5200 rev/min	201.6 V, NiMH
	PMSM 2, 50 kW @ 1200 rev/min		Inverter DC link voltage = 600 V
Toyota Lexus 450h hybrid, 2010	PMSM, 123 kW on front wheel; 50 kW on rear wheels	3.5 L V6 petrol	37 kW, NiMH
GM Volt hybrid, 2011	PMSM, one 55 kW MG, & one 111 kW motor	1.4 L petrol	16 kWh, 45 Ah, Li-Ion
Hyundai Sonata hybrid, 2011	PMSM, 30 kW,	2.4 L Petrol	Li-Polymer
Tesla Roadstar, 2009, EV	Induction machine, 215 kW	–	Li-Ion, 375 V, 5[illegible] kW; range: 36[illegible] km
Mistubishi iMiEV	PMSM, 47 kW	–	1[illegible] kWh Li-ion, range: 160 km
Renault Fluence EV	PMSM, [illegible] kW	–	22 kWh Li-ion, range: 185 km
BMW ActiveEV	PMSM, 125 kW	–	32 kWh, Li-ion, range: 151 km
Ford Focus BEV	PMSM, 107 kW	–	23 kWh, Li-ion, range: 122 km

traction motors superimposed on their limiting $T - \omega$ characteristics. In the following three subsections, the above three types of machines and their controls are briefly discussed.

21.2.1 Induction Machines

This machine has the advantage of being low-cost and simple construction and wide availability. A 215 kW 4-pole IM has been adopted notably in the Tesla Roadstar and by a few other automakers. Unlike PM machines, the position of the rotor flux vector (or phasor) cannot be directly measured for an IM. For fast dynamical control of IMs, as is required for modern vehicles, two control strategies have evolved, namely, the rotor flux oriented control (RFOC) and the DTC (Nash 1997; Casadei *et al.* 2008).

Indirect Rotor Flux Oriented Control

In RFOC, the desired stator flux angle is obtained by adding the slip speed, $\omega_{sl} = \omega_e - \omega_r$, to the rotor speed. By fully decoupling the d- and q-axes equations of the machine, the slip

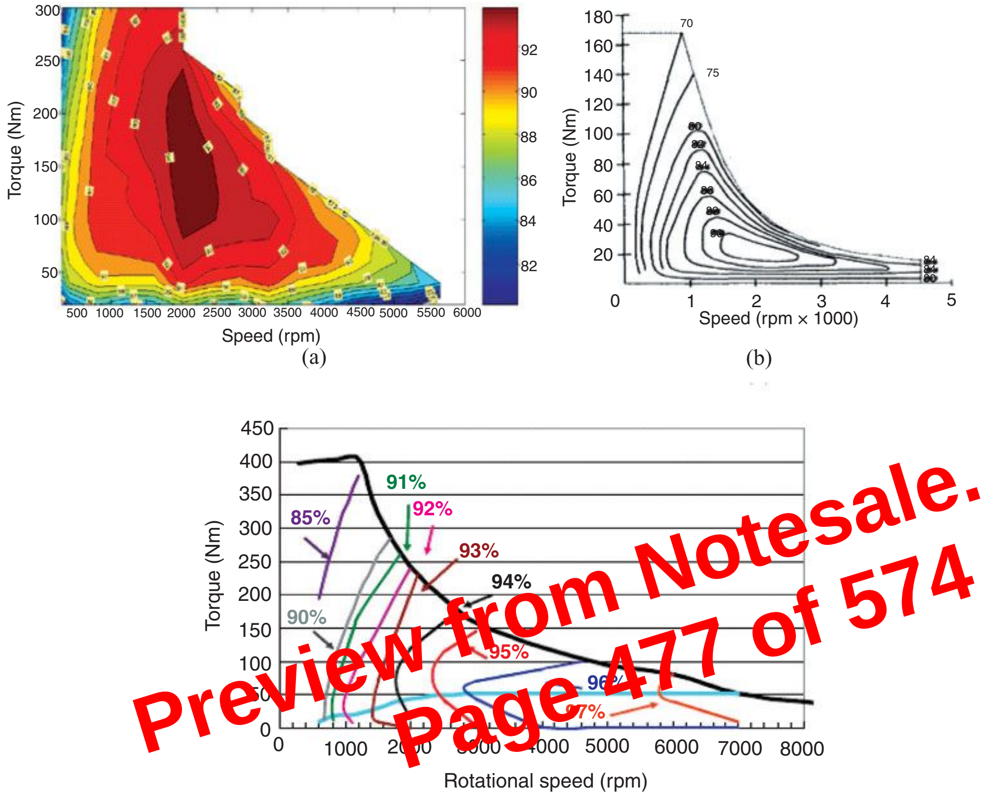

(a) (b)

(c)

Figure 21.10 Torque-speed characteristics and efficiency maps of (a) the IMPMSM in Toyota Camri Hybrid (Olszewski 2008), (b) an induction machine (Gosden *et al.* 1994), and (c) an SRM (Takano *et al.* 2010). (For a color version of this figure, please see color plates.)

speed can be made proportional to torque and the q-axis current i_{qs} in the synchronously rotating frame, subject to magnetic saturation and change of rotor resistance. The IM machine dynamics in this reference frame, the slip speed, rotor flux and torque equations are given as

$$\begin{bmatrix} v_{ds} \\ v_{qs} \\ v_{dr} \\ v_{qr} \end{bmatrix} = \begin{bmatrix} R_s + pL_s & -\omega_e L_s & pL_m & -\omega_e L_m \\ \omega_e L_s & R_s + pL_s & \omega_e L_m & pL_m \\ pL_m & -(\omega_e - \omega_r) & R_r + pL_r & -(\omega_e - \omega_r)L_r \\ (\omega_e - \omega_r)L_m & pL_m & (\omega_e - \omega_r)L_r & R_r + pL_r \end{bmatrix} \begin{bmatrix} i_{ds} \\ i_{qs} \\ i_{dr} \\ i_{qr} \end{bmatrix}, \tag{21.13}$$

$$\omega_e - \omega_r = \omega_{sl} = \frac{L_m}{\lambda_r}\frac{R_r}{L_r} i_{qs}, \tag{21.14}$$

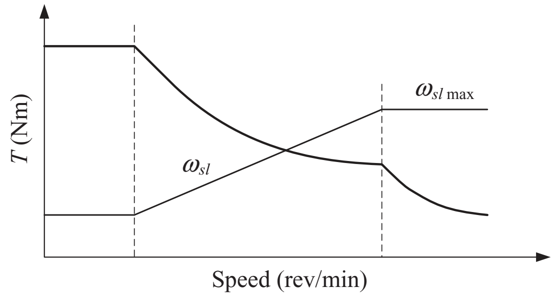

Figure 21.12 IM limiting torque-speed characteristic with slip limit and flux weakening

Direct Torque Control

In DTC, the machine torque, and stator and rotor flux linkages are estimated from the machine model using machine voltages and currents that are sensed at the machine/inverter terminals without requiring the mandatory mechanical position sensor which is indicated in the RFOC scheme of Figure 21.11 (West and Lorenz 2009). According to the errors in torque and flux, hysteresis controllers with optimum switching states for the inverter are determined which apply one of the eight voltage vectors to the motor. Space vector modulators, replacing the hysteresis controller that introduces variable switching frequency, have also been used. The DTC has been applied successfully in railway traction applications for some time (Kondou and Matsuoka 199[illegible]). The torque and flux control responses of the DTC scheme of Figure 21.13 can

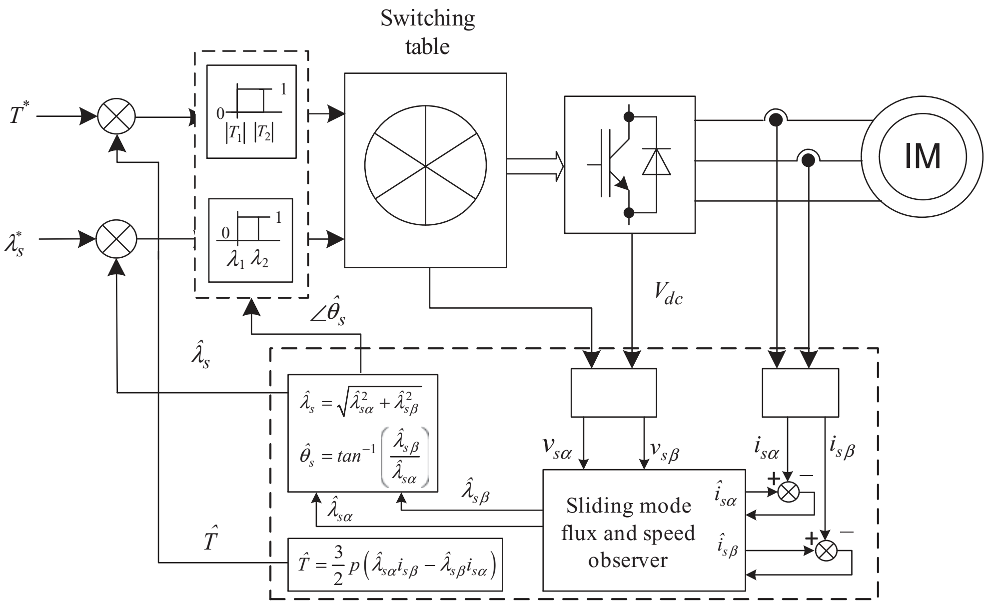

Figure 21.13 DTC scheme for an induction motor drive

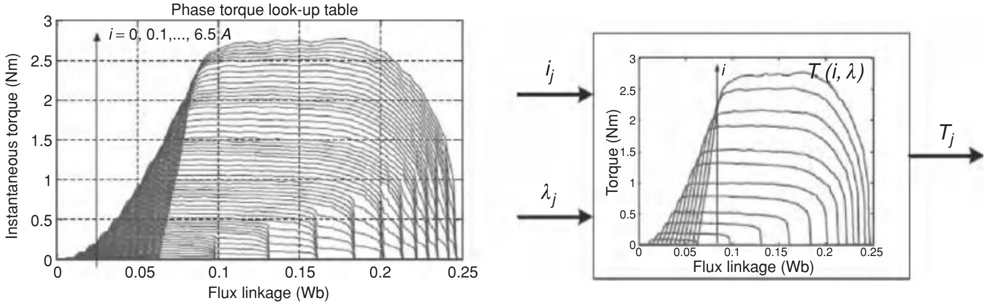

(a)

(b)

Figure 21.23 Torque versus current versus flux linkage of an SRM

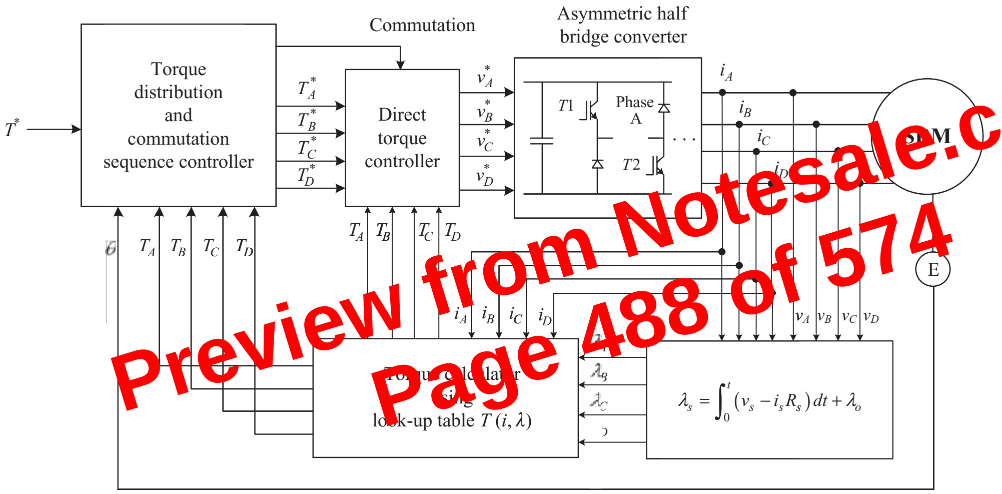

Figure 21.24 Direct torque control structure for an SRM

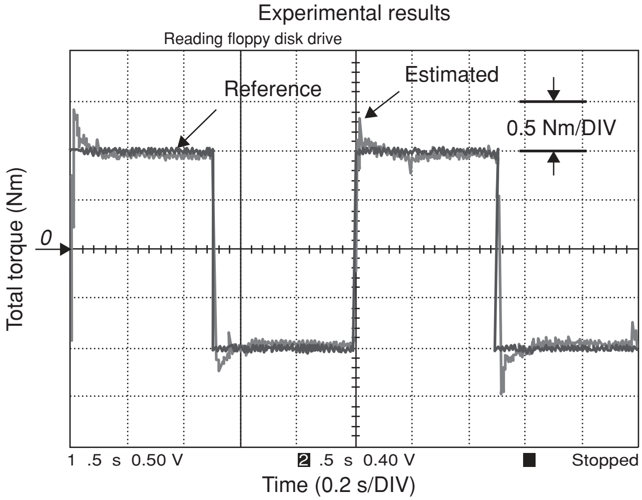

Figure 21.25 Dynamic torque response of an 8/6 SRM with direct torque control

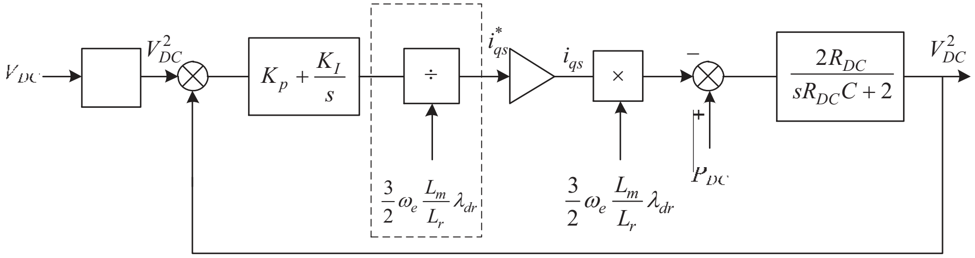

(a)

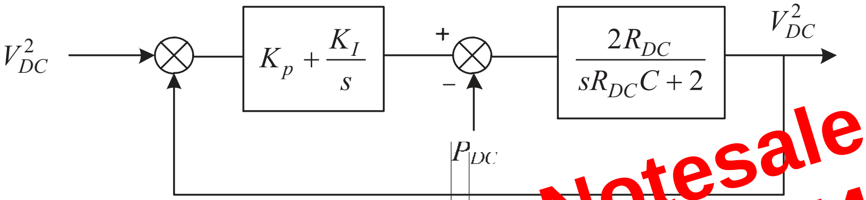

(b)

Figure 21.31 Block diagram representation DC link capacitor voltage controller

increasing the flux in the winding. When the switches are turned off, the diodes D1 and D2 charges the DC link capacitor. Figures 21.33a–c show the control structure for regenerative braking when the DC link capacitor is charged. The duty cycle of the switches is adjusted in order to control the regenerative current, and hence, the charging rate of the DC capacitor. It should be noted here that the switching interval for each winding must be appropriately advanced with increasing speed to ensure that current has time to build up to the desired value

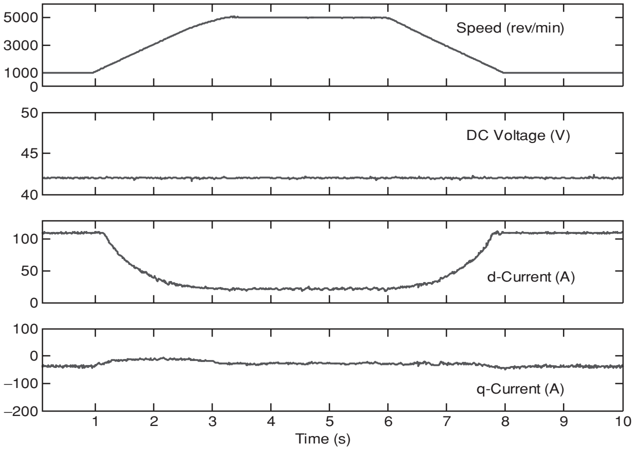

Figure 21.32 Capacitor voltage during acceleration and regenerative braking of an IM

References

Casadei D, Milanesi F, Serra G *et al.* (2008) Control of induction motors for wide speed range for electric vehicle drives. *Proceedings of the 18 ICEM*, pp. 1–6.

Dutta R and Rahman MF (2008) Design and analysis of an interior permanent magnet (IPM) machine with very wide constant power operation range. *IEEE Trans on Energy Conversion*, **23**(1), 25–33.

Dutta R, Chong L, Rahman M-F (2011) Analysis of CPSR in motoring and generating modes of an IPM motor. *International Electrical Machines and Drives Conference (IEMDC)*, Canada.

Foo G, Sayeef SM and Rahman MF (2010) Low speed and standstill operation of a sensorless direct torque and flux controlled IPM synchronous motor drive. *IEEE Transactions on Energy Conversion*, **25**(1), 25–33.

Fujii K and Fujimoto H (2007) Traction control based on slip ratio estimation without detecting vehicle speed for electric vehicle. *Proceedings of Power Conversion Conference*, Nagoya, Japan, pp. 688–693.

Gosden DF, Chalmers BJ, and Musaba L (1994) Drive system design for an electric vehicle based on alternative motor types. *Proceedings of IEE Power Electronics and Variable Speed Drives*, No. 399, pp. 710–715.

Holtz J (2006) Sensorless control of induction machines – with or without signal injection. *IEEE Transactions on Industrial Electronics*, **53**, 7–30.

Hori Y, Toyoda Y, and Tsuruoka Y (1998) Traction control of electric vehicle: basic experimental results using the test EV, UOT electric march. *IEEE Transaction on Industry Applications*, **34**(5), 1131–1998.

Jeong Y-S and Lee J-Y (2011) Parameter identification of an induction motor drive with magnetic saturation for electric vehicle. *Journal on Power Electronics*, **11**(4), 418–423.

Kondou K and Matsuoka K (1997) Permanent magnet synchonous motor control system for railway vehicle traction and its advantages, *Proceedings of the Power Conversion Conference, Nagoya, Japan*, **1**, pp. 63–68.

Karanayil B, Rahman MF, and Grantham C (2005) Stator and rotor resistance observers for induction motor drive using fuzzy logic and artificial neural networks. *IEEE Transactions on Energy Conversion*, **20**(4), 771–777.

Lovatt WH and Dunlop JB (2002) Optimization of switched reluctance motors for hybrid electric vehicles. *International Conference on Power Electronics, Machines and Drives, Bath UK*, pp. 177–182.

Miller J (2003) *Propulsion Systems for Hybrid Electric Vehicles*. Book in IET Power Engineering Series 45, Chapter 1, p. 31.

Nash JN (1997) Direct torque control, induction motor vector control without an encoder. *IEEE Transactions on Industry Applications*, **33**(2), 333–341.

Olszewski M (2008) Evaluation of the 2007 toyota camry hybrid synergy drive system. *Oak Ridge National Laboratory* Report FY 2008, US DOE, FreedomCAR and Vehicle Technologies, April 2008.

Rahman KM and Schultz SE (2002) Design of high efficiency and high torque density switched reluctance motor for vehicle propulsion. *IEEE Transaction on Industry Application* **38**(6), 1500–1507.

Rahman MF, Zhong L, and Lim KW (1998) A direct torque controlled interior magnet synchronous motor drive incorporating field weakening. *IEEE Transactions on Industry Applications*, **34**(6), 1246–1253.

Rajashekara K (1994) History of electric vehicles in general motors. *IEEE Transactions on Industry Applications*, **30**(4), 897–904.

Reddy PB, El-Refaie A, Huh K-K, *et al.* (2011) Comparison of interior and surface permanent magnet machines equipped with fractional-slot windings for hybrid vehicles. *IEEE ECCE 2011*, pp. 2252–2259.

Takano Y, Takeno M, Imakawa T, *et al.* (2010) Torque density and Efficiency Improvements of a Switched Reluctance Motor without Rare-Earth Material for Hybrid Vehicles. *Proceedings of IEEE ECCE*, pp. 2653–2659.

Telford D, Dunnigan MW, and Williams BW (2003) On-line identification of induction machine electrical parameters for vector control tuning. *IEEE Transactions on Industrial Electronics*, **50**, 253–261.

West NT and Lorenz RD (2009) Digital implementation of stator and rotor flux linkage observer for deadbeat direct torque control of induction machines. *IEEE Transactions on Industry Applications*, **45**(2), 729–736.

Sayeef S, Foo G, and Rahman MF (2010) Rotor position and speed estimation of a variable structure direct-torque-controlled IPM synchronous motor drive at very low speeds including standstill. *IEEE Transactions on Industrial Electronics*, **57**(11), 3715–3723.

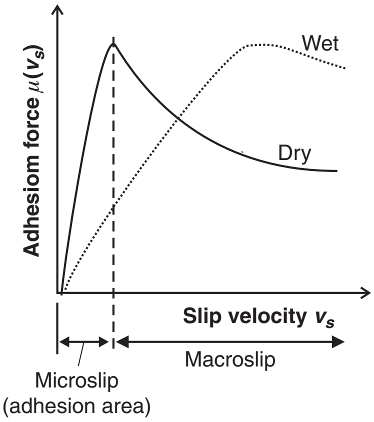

Figure 22.4 Relation between adhesion force $\mu(v_s)$ and slip velocity v_s of the coach

The two-mass model of the mechanical system is as follows:

$$J_M \frac{d\omega_m}{dt} = T_e - T_{S1} \tag{22.6}$$

$$J_L \frac{d\omega_L}{dt} = n_i T_{S2} - T_L \tag{22.7}$$

$$\frac{d\varphi_r}{dt} = \omega_m, \tag{22.8}$$

$$\frac{d\varphi_L}{dt} = \omega_L, \tag{22.9}$$

$$T_{S1} = K_2 \left(\theta_m - n_i \theta_L\right) + H_2 \left(\omega_m - n_i \omega_L\right), \tag{22.10}$$

$$T_{S2} = n_i |T_{S1}|, \tag{22.11}$$

where ω_L is the mechanical speed of the load, θ_m is the angle position of the motor rotor, θ_L is the angle position of the load, T_e is the motor electromagnetic torque, T_L is the traction load torque, T_{S1} is the transmitted torque on gear input = motor load torque, T_{S2} is the transmitted torque on gear output, K_2 is the stiffness function, H_2 is the damping coefficient (170 Ns/m), J_L is the load inertia (3000 kgm^2), and n_i is the gear ratio (1.97).

Function K_2 depends on gear wheel tooth stiffness (Muller 1979):

$$K_2 = K_S + K_D \sin(z\varphi_m), \tag{22.12}$$

where K_S is the stiffness average value (3.5×10^5 N/m), K_D is the stiffness maximum value (5.7×10^5 N/m), and z is the number of the gear driving wheel teeth (25 teeth).

In (22.7), the meshing frequency higher harmonics were omitted. It is a result of skew teeth in the modeled gear. For such gear the meshing amplitudes in healthy condition are very small.

The misalignment in the transmission system was modeled as an additional load torque component T_w:

$$J_M \frac{d\omega_m}{dt} = T_{\mathrm{em}} - T_{S1} - T_w. \tag{22.13}$$

The additional torque component T_w is sinusoidal value with frequency equal to the motor shaft rotation:

$$T_w = T_{wav}\left(1 + \sin(\varphi_m)\right), \tag{22.14}$$

where T_{wav} is the average value of the misalignment load torque component (720 Nm).

In (22.6), a viscous friction was considered:

$$J_M \frac{d\omega_m}{dt} = T_{\mathrm{em}} - T_{S1} - T_w + T_f, \tag{22.15}$$

where T_f is the viscous friction load torque component.

The torque component T_f is

$$T_f = F\omega_m, \tag{22.16}$$

where F is the viscous friction coefficient (0.8 Nm/m).

22.2.3 High-Power Electronic Converter

The HST traction system has double way supply: ac supply 25 kV 50 Hz and dc supply 1.5 kV. The train high-speed range is obtained only with the ac high-voltage traction mode. In case of using an ac train supply, one-phase transformer is utilized (Wilk 2009). The transformer output ac supply is converted into dc by full controlled transistorized rectifier, filtered in the intermediate dc link and converted to ac motor supply by a three-phase voltage inverter with insulated gate bipolar transistor (IGBT) transistors (Figure 22.5). In the simulation program, the voltage inverter was modeled with ideal switches controlled with a pulse width modulation method. Regarding the high power of the drive transistor, a switching frequency of the IGBT in the traction drive is variable within the range from 450 Hz for low speeds of the motor to square wave for highest motor speeds.

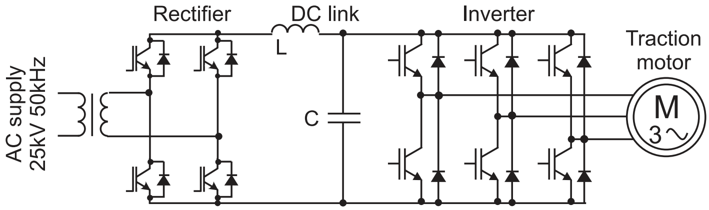

Figure 22.5 Supply system of the HST traction motor

The load torque calculation method (22.26) is very simple; however, it is not precise. This results from its sensitivity to any inaccuracy and the simplifications in the mechanical equations. Because of that it is rather not viable tool for diagnostic system.

Instead of simple estimation (22.26), the observer methods seems to be more precise. Some of the load torque observers are presented in the literature, for example, the concept of the observers for systems with unknown and inaccessible inputs or the concept of full order Luenberger-based systems (Brdys and Du 1991). Unfortunately, some of the observers have strongly limited bandwidth or are not applicable to the FOC control algorithm.

In the presented application, different methods for the load torque calculations were previously tested (Guzinski *et al.* 2009a). The best results were obtained with an observer based on the Gopinanth's method (Ohnishi *et al.* 1996) that was previously used in the traction application as part of train wheels slip detection system (Kadowaki *et al.* 2007).

The load torque observer is described as the next:

$$\frac{d}{d\tau}\begin{bmatrix} z_1 \\ z_2 \end{bmatrix} = \begin{bmatrix} 0 & -k_{1L} \\ 1 & -k_{2L} \end{bmatrix}\begin{bmatrix} z_1 \\ z_2 \end{bmatrix} + \begin{bmatrix} k_{1L}k_{2L}J_M & (k_{2L}^2 - k_{1L})J_M \end{bmatrix}\hat{\omega}_m + \begin{bmatrix} k_{1L} \\ k_{2L} \end{bmatrix}\hat{T}_{\mathrm{em}} \qquad (22.27)$$

$$\hat{T}_{S1} = z_2 - k_{2L}J_M\hat{\omega}_m, \qquad (22.28)$$

where k_{1L}, k_{2L} are observer gains, z_1, z_2 are internal observer variables, $\hat{T}_{\mathrm{em}}$ are motor torque computed by equation (22.25).

Presented load torque observer (22.27)–(22.28) does not require speed sensor because the motor speed is computed in the speed observer procedure.

22.4 Simulation Investigations

Simulation was realized using Matlab software. An example of the results obtained using speed observer operation are depicted in Figure 22.9. In Figure 22.9, the desired motor torque is used as the commanded value.

For improving simulation time a smaller inertia of the whole train was assumed. Motor speed is changed to the next values referring to train speed $30 \cdots 160 \cdots 210 \cdots 150$ km/h. The error between the measured and estimated speeds is also shown, and it is observed that this error is significantly small and it is less than 2%.

In the next simulation test, the load torque T_L is applied at the start of the drive transmission with simultaneous changes of motor speed. Also in this case, the operation of the proposed observer is correct as illustrated in Figure 22.10.

In Figure 22.10, a comparison of he real motor load torque T_{S1} with the computed one in the observer $\hat{T}_{S1}$ is presented. The results show correct performance except at initial time, in which load observer started computation.

22.5 Experimental Test Bench

In the second step of verification of the speed and load torque observers the experiments were done. The experiments were provided in the HST factory, where the HST test bench were

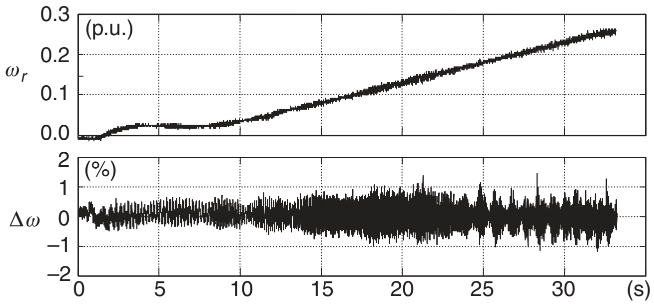

Figure 22.14 Speed observer experimental results—the train start to 50 km/h

22.6 Experimental Investigations

The examples of the experimental speed observer calculations are illustrated in Figures 22.14 and 22.15. In the test of Figure 22.14, speed observer error is low and does not exceed 1.5%. In Figure 22.15, an increase in computation error with train speed is noticed. At speed 320 km/h (the train full speed), this error reached 5%. This error is caused by a distortion in motor stator current. With an increase in motor speed, inverter switching frequency was decreased from 450 Hz until an operation without PWM for full train speed. The changes in PWM are done to fully utilize the inverter dc supply voltage in the motor high-speed range. The distortion of the motor current in the high-speed range are presented in Figure 22.16.

The proposed load torque observer is supposed to be used for fault detection in the torque transmission system. Comparable experimental investigation should be realized for correctly working torque transmission system and for faulty system for different fault types. However, because of limited access to faulty real system and because of high cost of faulty transmission system, experimental investigations were up to now limited to the existing in the HST factory

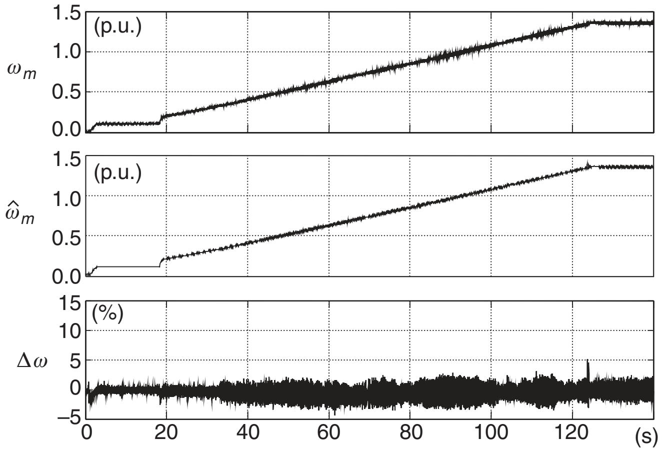

Figure 22.15 Experimental results—the train start up to 320 km/h

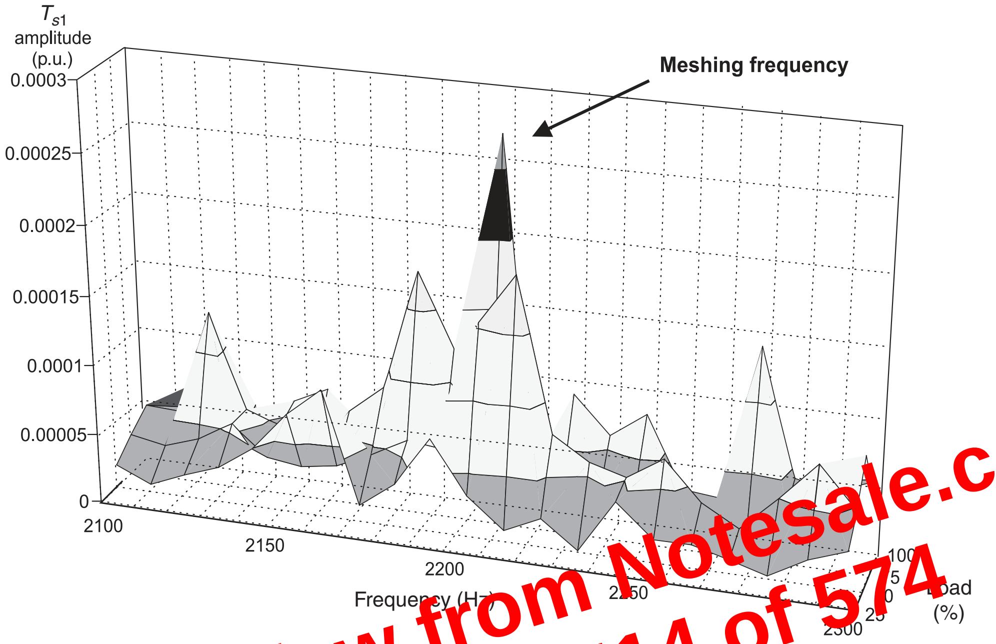

Figure 22.18 Identification of the gear meshing frequency for motor speed related to ca. 150 km/h train velocity. (For a color version of this figure, please see color plates.)

speeds—related to next train speeds: 50 km/h and 150 km/h. For each speed, the load was changed to the levels 25%, 50%, 75%, 100%. Fast Fourier transform (FFT) harmonic analysis was then realized for the load torque and next the amplitudes levels related to meshing frequencies were plotted. According to the transmission theory, an increase of amplitudes with load increment is noticed (Muller 1979).

Higher precision of computation was observed for lower speed 50km/h which is, similarly to the case of speed observer, caused by distorting current waveform with decreasing inverter transistors switching frequency at higher speeds.

Above 150 km/h torque observer was not able to identify meshing frequency, which makes it possible to assume that its practical use could be limited for speed range up to 150 km/h. Nevertheless, torque observer is applicable for diagnosis purposes, because it is not required that it works all the time but, for example, at lower speeds only. This is supposed to ensure a detection of transmission system faults. Assembly defects of transmission system are characterized by violent failures, which could be detected during initial test for train travels at lower speeds.

22.7 Diagnosis System Principles

Diagnosis system is currently intended to evaluate diagnostic criterion. It is assumed that a diagnostic system will not utilize any additional sensor except the sensors that are currently used in existing HST. The main parts of our diagnostic system are speed and load torque observers. For condition detection of speed sensor and drive transmission system, specific values computation is going to be realized and analyzed according to the defined criterions. This aims for proper fault detection appearing and to the prediction of future faults before their occurring.

22.7.1 Diagnosis of Speed Sensor

The base speed sensor diagnosis depends on real-time inspection of the next diagnostic criterion:

$$|\hat{\omega}_m - \omega_m| > E_{mlimit} \tag{22.29}$$

where E_{mlimit} is the error limit between the measured and the computed speed.

On the base of the simulation and experimental tests, it was assumed that this error level E_{mlimit} is limited to 3%. This value was selected to be higher than the maximum observed speed observer computational error, a 2% value.

If the diagnostic system identifies crossing of this limit level, then the system should give an appropriate fault alarm and then HST control system could be switched to sensorless mode of operation (Figure 22.19). In Figure 22.19 the speed sensor fault appeared at instant 5 s. At this instant, the measured speed was equated to zero. The control system detected fault and a diagnostic indicator $d_{\omega m}$ has been changed from 0 to 1. This was done immediately—in one step of the control calculation algorithm. Simultaneously, the whole system was switched to the speed sensorless operation mode without any noticeable disturbances. After fault detection, the commanded motor torque was changed and the system has reacted correctly.

The other fault of the speed sensor is also possible—in the speed scanning buffer the last proper value of the measured speed could be memorized. If this happens during a steady state, the diagnostic system does not react immediately. In such case, the whole system still works

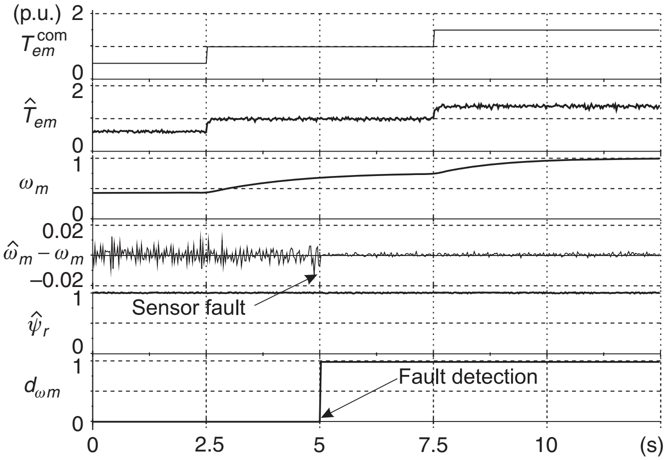

Figure 22.19 Speed sensor fault identification and switch to speed sensorless control

23

AC Motor Control Applications in High-Power Industrial Drives

Ajit K. Chattopadhyay
Electrical Engineering Department, Bengal Engineering & Science University, India

23.1 Introduction

The power ratings of large medium voltage (2.2–13.8 kV) industrial drives range between few hundred kilowatts to a few tens of megawatts and even 100 MW. The upper limit is decided by the requirements of the applications rather than by the technology of the converters and machines (Stemmler 1994). The available speed range lies from 10 rpm for low-speed machines (e.g. Cement mills), 1500/3000 rpm for normal-speed drives to even 18 000 rpm for very high power high speed drives (e.g., compressors). The limits for the dc motors such as cost, size, commutator problems and inability to operate satisfactorily in a dirty and explosive environment have called for ac motor drives for high power applications. Major technical breakthroughs have occurred both in the power conversion and in control areas of variable voltage variable frequency (VVVF) ac drives to meet the exacting requirements of ac drives using direct ac/ac cycloconverters or ac/dc/ac link inverters that feed either induction motors (IM) or synchronous motors (SM). The machine may be excited by a voltage source inverter (VSI) or a current source inverter (CSI). Synchronous motor drives have the advantages over the induction motor drives in that, with separate field excitation, these can be operated at any power factor-leading, lagging and unity. The operation near unity power factor reduces armature copper loss and permits inverter size reduction with simplicity of commutation (load commutation) with thyristors as switches. Further, a synchronous motor runs at a precisely set speed independent of load and voltage fluctuations unlike an induction motor.

The recent trends in high-power ac drives are to use pulse width modulated (PWM) VSI or CSI with self-commutated devices like insulated gate bipolar transistors (IGBTs), gate turn

AC Electric Motors Control: Advanced Design Techniques and Applications, First Edition. Edited by Fouad Giri.

off thyristors (GTOs), integrated gate commutated thyristors (IGCTs) and injection enhanced gate transistors (IEGTs) for efficient VVVF control with harmonic reduction. The development of new high-power semiconductors such as 3.3/4.5 kV, 1.7/1.2 kA IGBTs, 6 kV, 6 kA IGCTs and 4.5 kV, 5.5 kA IEGTs capable of snubberless operation and the introduction of three level topologies in contrast to earlier two level ones have led to an increased application of PWM controlled Voltage Source Converters (VSC) ranging from 0.5 MVA to about 30 MVA (Chattopadhyay 2010). CSI-fed drives with simplified regeneration control and microcomputer-controlled drives implementing evolutionary concepts like *field orientation* or *vector control (VC)*, with either inverter or cycloconverter-fed induction or SM by which dc machine-like performance can be obtained and *direct torque control* (DTC) are now finding increasing acceptance in *high-performance* industrial ac drives for applications such as steel mills, ore-grinding mills, cement kilns, ship drives, mine winders, and electric traction (Chattopadhyay 1997a). The converters for such drives meeting the *high performance* requirements must:

- generate smoothly variable frequency and voltage;
- produce nearly sinusoidal current waveforms throughout the operating range to avoid undesirable torque oscillations;
- permit highly dynamic control both in forward and reverse motoring and braking applications;
- provide as nearly as possible or even better performance than that of the dual converter-fed dc drives as regards cost, service reliability and harmonic effects on the system.

Besides the application of field-oriented control (FOC) in PWM inverter-fed motor drives with various PWM schemes like carrier-based, hysteresis-band control and space vector modulation (SVM), the recent application of DTC to ac drives (Chattopadhyay 2010) has been claimed to achieve the highest torque and speed performance ever achieved with variable speed drives, making it possible to control the full torque within a few milliseconds, reducing the impacts of load shocks.

Thus, rapid and remarkable progress has been made over the years in the ac drive technology used in the high-power drives and their control. Figure 23.1 shows a block diagram of a typical high power ac drive system for a mill with its various components. The technology is vast and the objective of this chapter is to present a brief but comprehensive state-of-the-art overview of the development of each of the components such as high-power semiconductor devices, converter topologies, motors used and the control strategies employed together with their various application examples in the industry. The brief features of the industrial ac drives developed by the leading manufacturers worldwide are also provided as well as new developments and possible future trends.

23.2 High-Power Semiconductor Devices

Rapid advances in industrial ac drives and power conversion systems have been possible due to continuous and astonishing development of the rating and performance of the power semiconductor devices over the last 50 years. Two major types of high-power semiconductor devices are used in high power converters in the industry: the thyristor-based (*current switched*)

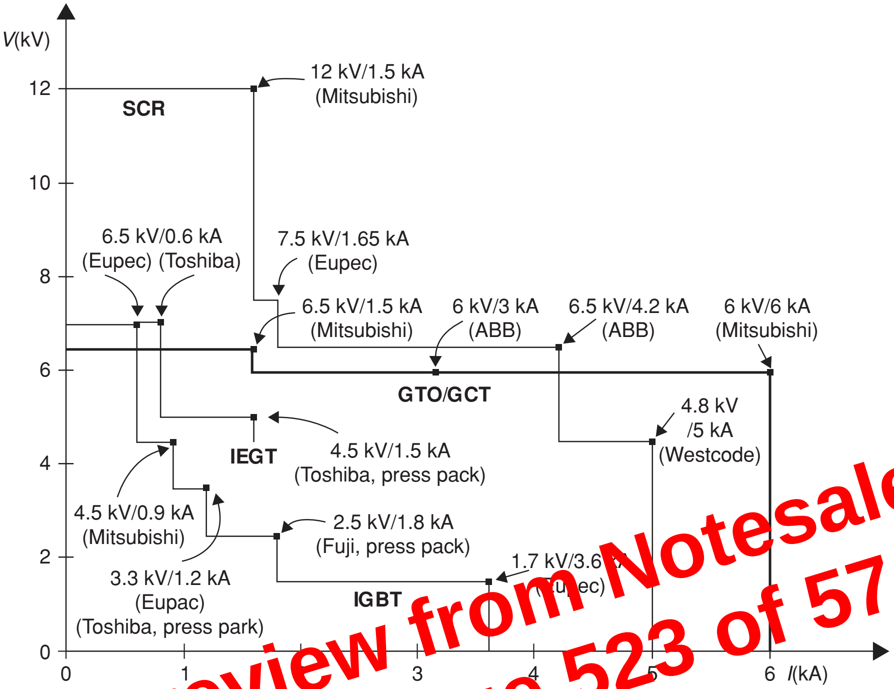

Figure 23.2 Voltage and current ratings of high-power semiconductor devices. Reprinted with permission from IEEE (Chattopadhyay 2010)

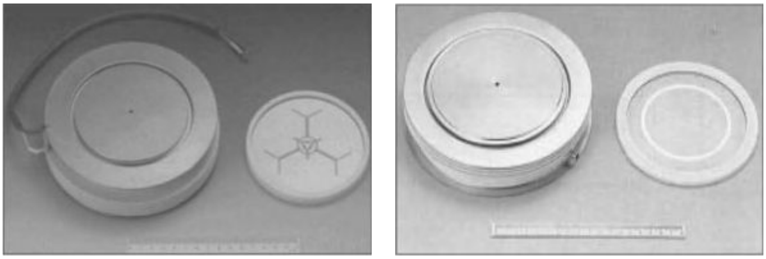
(a) 12-kV, 1.5-kA SCR (b) 6-kV, 6-kA GTO

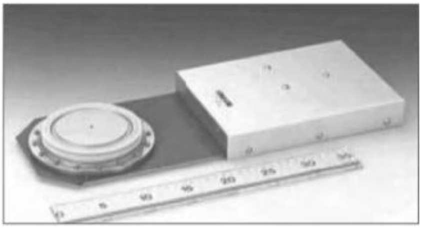
(c) 6-kV, 6-kA IGCT/GCT

Figure 23.3 Thyristor-based (current switched) high-power semiconductor devices. Reprinted with permission from IEEE (Chattopadhyay 2010)

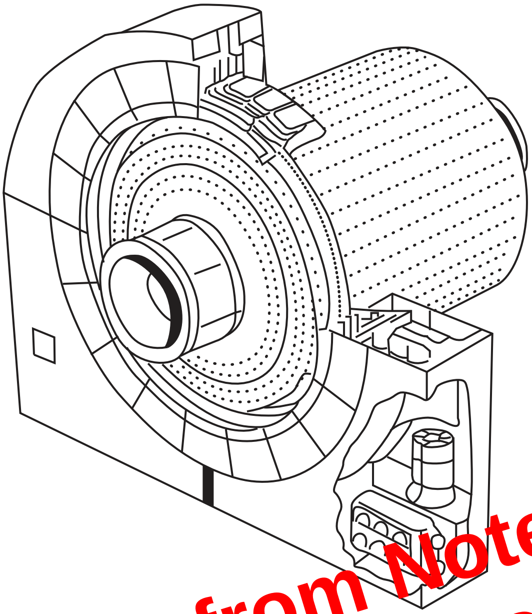

Figure 23.36 View of a wrap-around or ring motor for cement or ore grinding mill

motors to facilitate variable motor speed and thrust from fixed or controllable pitch propellers. The power electronic converters mostly used in modern marine electrical propulsion are ac cycloconverter, LCI and the PWM VSI. The feasibility of a practical marine MC for electrical propulsion system has been studied recently (Bucknall and Ciaramella 2010).

Cycloconverter drive technology is ideally suited to the extreme requirements (large powers at low speeds and high dynamic performance) of the icebreaker. For example, US Coast Guard Icebreaker Healy is equipped with 2 × 11.2 MW, 0–130/160 rpm dual wound motors driving twin shafts, each motor being powered by two 5.6 MW 12-pulse ALSTOM Alspa CL9000 Cycloconverters capable of providing 175% full load trorque for 30 s at zero speed (English 2001; Radan 2004). A shuttle tanker equipped with ABB made cycloconverter propeller drives is also mentioned in Radan (2004). A vector-controlled cycloconverter-fed drive designed for icebreaker to deliver 16 000 hp to the twin propeller shafts of a Canadian Coast Guard icebreaker is reported in (Hill *et al.* 1987).

LCI-fed synchronous motor drives (also known as Synchroconverter-CSI drives) are ideally suited to normal high-power ship propulsion applications such as the cruise liners, for example, RCI Cruise Liner INFINITY with two 19 MW Mermaid podded propulsers which use 2 × 7 MW, 0–118/135 rpm motors with 2 × 12-pulse synchroconverters (English 2001; Radan 2004). Another interesting application of LCIs is in a container ship (Clegg *et al.* 1999), where a 24-pulse SCR-rectifier-inverter system serves as a frequency converter to convert a voltage of 14–25.7 Hz generated by the shaft generator to a bus voltage of 6.6 kV, 60 Hz for the ship's main distribution system.

Medium voltage source two-level inverters with water-cooled series IGBTs with ratings typically up to 20 MW, 2000 rpm, 6.6 kV have been used in drill ships. The ship *Pride*

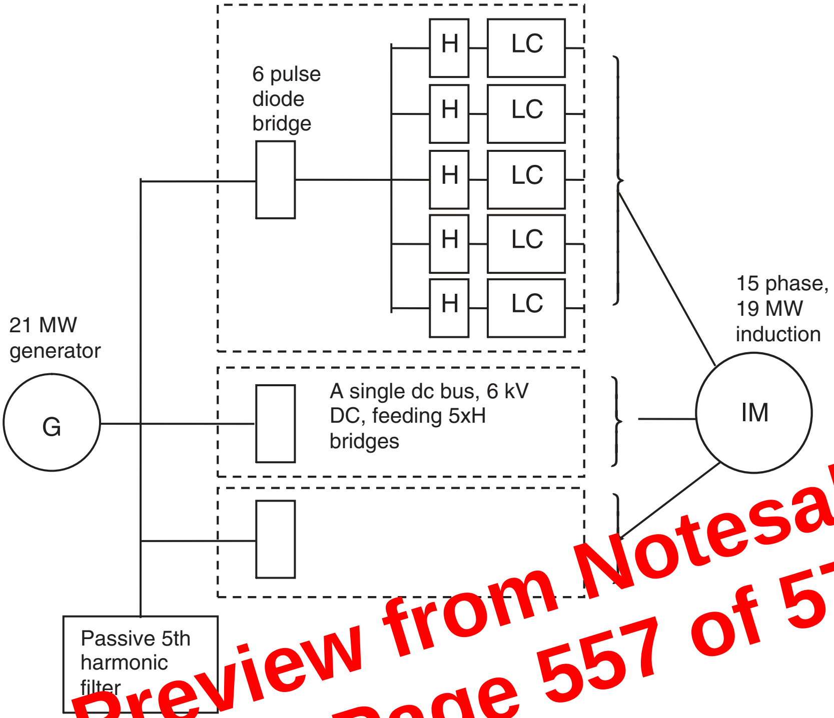

Figure 23.37 Schematic diagram of IPS drive system of a ship (Crane and McCoy 1999)

Africa is fitted with 7 medium voltage ALSTOM VDM5000 IGBT variable speed thrustor drives up to 4.5 MW (English 2001). World's first electric warship-UK's "daring class" *Type-45 Destroyer*, in service from 2007 is fitted with two 15-phase 20 MW, 4.16 kV ALSTOM VDM25000 PWM drives with advanced induction motors for main propulsion. An integrated power system for all electric ship in a full-scale main propulsion drive for US navy (Crane and McCoy 1999) consists of a main propulsion 19 MW induction motor drive system. The PWM converter (Figure 23.37) consists of three 6-pulse rectifier bridges, three 6 kV dc links and 15 IGBT-based H bridges feeding a 15-phase induction motor.

23.6.4 Mine Hoists, Winders, and Draglines

The trends in the electronic control of mine hoists and winders in the 1970s and 1980s were reviewed in Madiseti and Ramlu, (1986), where it was mentioned that SM supplied by cycloconverter control are ideally suited for hoisting applications that are directly coupled. Torques of about six times the rated torque at low speed are possible and with digital monitoring the winding cycle can be optimised, smooth and accurate. Advanced hoist technologies in coal mines in China and zinc and copper mines in Finland with high-power SM (e.g 2.5 MW, 3 × 3050 V, 8.7 Hz, 65.8 rpm by ABB in *Pyhasalmi* mine in Finland with shaft depths of 1450 m) are enumerated in Chadwick (2010). The *Pyhasalmi* mine hoist is the first in the world to

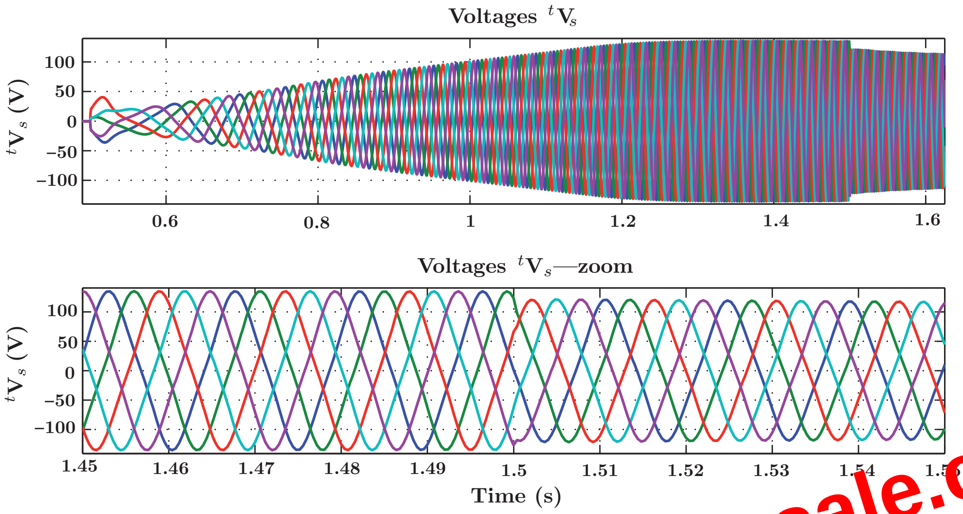

Figure 12.12 Stator voltages in the original reference frame Σ_t during the velocity rising ramp. (See page 250).

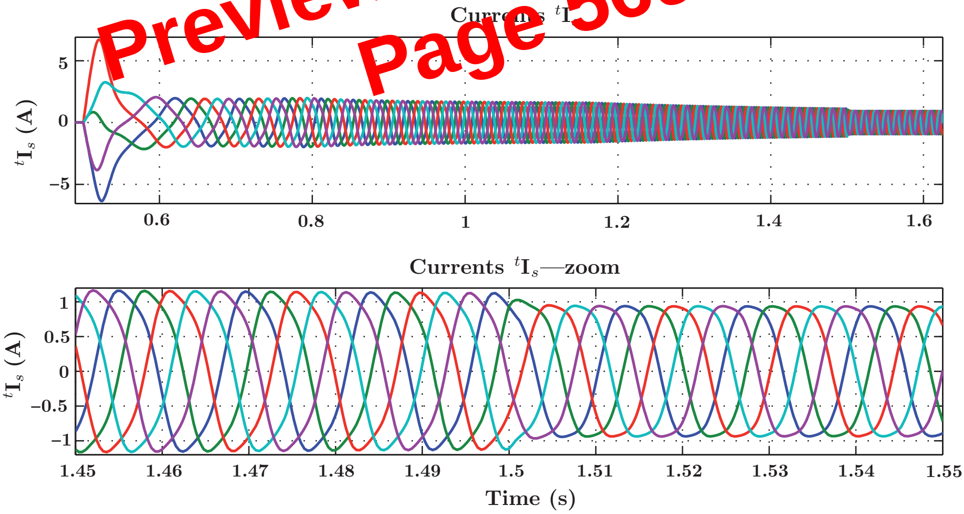

Figure 12.13 Stator currents in the original reference frame Σ_t during the velocity rising ramp. (See page 250).